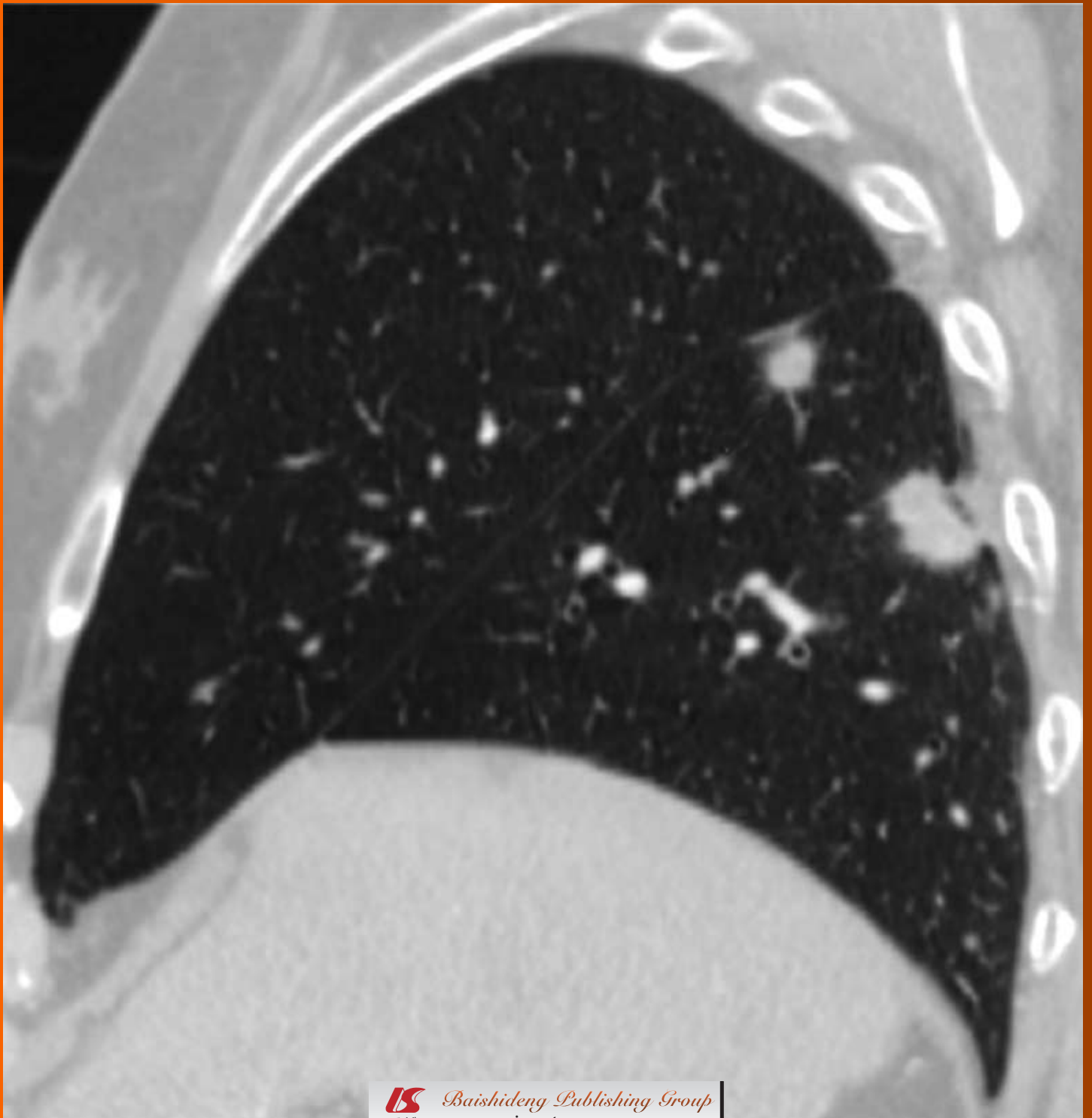


World Journal of *Radiology*

World J Radiol 2012 April 28; 4(4): 126-185





Editorial Board

2009-2013

The *World Journal of Radiology* Editorial Board consists of 319 members, representing a team of worldwide experts in radiology. They are from 40 countries, including Australia (3), Austria (4), Belgium (5), Brazil (3), Canada (9), Chile (1), China (25), Czech (1), Denmark (1), Egypt (4), Estonia (1), Finland (1), France (6), Germany (17), Greece (8), Hungary (1), India (9), Iran (5), Ireland (1), Israel (4), Italy (28), Japan (14), Lebanon (1), Libya (1), Malaysia (2), Mexico (1), Netherlands (4), New Zealand (1), Norway (1), Saudi Arabia (3), Serbia (1), Singapore (2), Slovakia (1), South Korea (16), Spain (8), Switzerland (5), Thailand (1), Turkey (20), United Kingdom (16), and United States (82).

EDITOR-IN-CHIEF

Filippo Cademartiri, *Monastier di Treviso*

STRATEGY ASSOCIATE

EDITORS-IN-CHIEF

Ritesh Agarwal, *Chandigarh*
Kenneth Coenegrachts, *Bruges*
Mannudeep K Kalra, *Boston*
Meng Law, *Los Angeles*
Ewald Moser, *Vienna*
Aytekin Oto, *Chicago*
AAK Abdel Razek, *Mansoura*
Àlex Rovira, *Barcelona*
Yi-Xiang Wang, *Hong Kong*
Hui-Xiong Xu, *Guangzhou*

GUEST EDITORIAL BOARD MEMBERS

Wing P Chan, *Taipei*
Wen-Chen Huang, *Taipei*
Shi-Long Lian, *Kaohsiung*
Chao-Bao Luo, *Taipei*
Shu-Hang Ng, *Taoyuan*
Pao-Sheng Yen, *Hualien*

MEMBERS OF THE EDITORIAL BOARD



Australia

Karol Miller, *Perth*
Tomas Kron, *Melbourne*
Zhonghua Sun, *Perth*



Austria

Herwig R Cerwenka, *Graz*
Daniela Prayer, *Vienna*

Siegfried Trattnig, *Vienna*



Belgium

Piet R Dirix, *Leuven*
Yicheng Ni, *Leuven*
Piet Vanhoenacker, *Aalst*
Jean-Louis Vincent, *Brussels*



Brazil

Emerson L Gasparetto, *Rio de Janeiro*
Edson Marchiori, *Petrópolis*
Wellington P Martins, *São Paulo*



Canada

Sriharsha Athreya, *Hamilton*
Mark Otto Baerlocher, *Toronto*
Martin Charron, *Toronto*
James Chow, *Toronto*
John Martin Kirby, *Hamilton*
Piyush Kumar, *Edmonton*
Catherine Limperopoulos, *Quebec*
Ernest K Osei, *Kitchener*
Weiguang Yao, *Sudbury*



Chile

Masami Yamamoto, *Santiago*



China

Feng Chen, *Nanjing*
Ying-Sheng Cheng, *Shanghai*
Woei-Chyn Chu, *Taipei*
Guo-Guang Fan, *Shenyang*

Shen Fu, *Shanghai*

Gang Jin, *Beijing*
Tak Yeung Leung, *Hong Kong*
Wen-Bin Li, *Shanghai*
Rico Liu, *Hong Kong*
Yi-Yao Liu, *Chengdu*
Wei Lu, *Guangdong*
Fu-Hua Peng, *Guangzhou*
Liang Wang, *Wuhan*
Li-Jun Wu, *Hefei*
Zhi-Gang Yang, *Chengdu*
Xiao-Ming Zhang, *Nanchong*
Chun-Jiu Zhong, *Shanghai*



Czech

Vlastimil Válek, *Brno*



Denmark

Poul Erik Andersen, *Odense*



Egypt

Mohamed Abou El-Ghar, *Mansoura*
Mohamed Ragab Nouh, *Alexandria*
Ahmed A Shokeir, *Mansoura*



Estonia

Tiina Talvik, *Tartu*



Finland

Tove J Grönroos, *Turku*

**France**

Alain Chapel, *Fontenay-Aux-Roses*
 Nathalie Lassau, *Villejuif*
 Youlia M Kirova, *Paris*
 Géraldine Le Duc, *Grenoble Cedex*
 Laurent Pierot, *Reims*
 Frank Pilleul, *Lyon*
 Pascal Pommier, *Lyon*

**Germany**

Ambros J Beer, *München*
 Thomas Deserno, *Aachen*
 Frederik L Giesel, *Heidelberg*
 Ulf Jensen, *Kiel*
 Markus Sebastian Juchems, *Ulm*
 Kai U Juergens, *Bremen*
 Melanie Kettering, *Jena*
 Jennifer Linn, *Munich*
 Christian Lohrmann, *Freiburg*
 David Maintz, *Münster*
 Henrik J Michaely, *Mannheim*
 Oliver Micke, *Bielefeld*
 Thoralf Niendorf, *Berlin-Buch*
 Silvia Obenauer, *Duesseldorf*
 Steffen Rickes, *Halberstadt*
 Lars V Baron von Engelhardt, *Bochum*
 Goetz H Welsch, *Erlangen*

**Greece**

Panagiotis Antoniou, *Alexandroupolis*
 George C Kagadis, *Rion*
 Dimitris Karacostas, *Thessaloniki*
 George Panayiotakis, *Patras*
 Alexander D Rapidis, *Athens*
 C Triantopoulou, *Athens*
 Ioannis Tsalafoutas, *Athens*
 Virginia Tsapaki, *Anixi*
 Ioannis Valais, *Athens*

**Hungary**

Peter Laszlo Lakatos, *Budapest*

**India**

Anil Kumar Anand, *New Delhi*
 Surendra Babu, *Tamilnadu*
 Sandip Basu, *Bombay*
 Kundan Singh Chufal, *New Delhi*
 Shivanand Gamanagatti, *New Delhi*
 Vimoj J Nair, *Haryana*
 R Prabhakar, *New Delhi*
 Sanjeeb Kumar Sahoo, *Orissa*

**Iran**

Vahid Reza Dabbagh Kakhki, *Mashhad*
 Mehran Karimi, *Shiraz*
 Farideh Nejat, *Tehran*
 Alireza Shirazi, *Tehran*
 Hadi Rokni Yazdi, *Tehran*

**Ireland**

Joseph Simon Butler, *Dublin*

**Israel**

Amit Gefen, *Tel Aviv*
 Eyal Sheiner, *Be'er-Sheva*
 Jacob Sosna, *Jerusalem*
 Simcha Yagel, *Jerusalem*

**Italy**

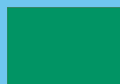
Mohssen Ansarin, *Milan*
 Stefano Arcangeli, *Rome*
 Tommaso Bartalena, *Imola*
 Sergio Casciaro, *Lecce*
 Laura Crocetti, *Pisa*
 Alberto Cuocolo, *Napoli*
 Mirko D'Onofrio, *Verona*
 Massimo Filippi, *Milan*
 Claudio Fiorino, *Milano*
 Alessandro Franchello, *Turin*
 Roberto Grassi, *Naples*
 Stefano Guerriero, *Cagliari*
 Francesco Lassandro, *Napoli*
 Nicola Limbucci, *L'Aquila*
 Raffaele Lodi, *Bologna*
 Francesca Maccioni, *Rome*
 Laura Martincich, *Candiolo*
 Mario Mascacchi, *Florence*
 Roberto Miraglia, *Palermo*
 Eugenio Picano, *Pisa*
 Antonio Pinto, *Naples*
 Stefania Romano, *Naples*
 Luca Saba, *Cagliari*
 Sergio Sartori, *Ferrara*
 Mariano Scaglione, *Castel Volturno*
 Lidia Strigari, *Rome*
 Vincenzo Valentini, *Rome*

**Japan**

Shigeru Ehara, *Morioka*
 Nobuyuki Hamada, *Chiba*
 Takao Hiraki, *Okayama*
 Akio Hiwatashi, *Fukuoka*
 Masahiro Jinzaki, *Tokyo*
 Hiroshi Matsuda, *Saitama*
 Yasunori Minami, *Osaka*
 Jun-Ichi Nishizawa, *Tokyo*
 Tetsu Niwa, *Yokohama*
 Kazushi Numata, *Kanagawa*
 Kazuhiko Ogawa, *Okinawa*
 Hitoshi Shibuya, *Tokyo*
 Akira Uchino, *Saitama*
 Haiquan Yang, *Kanagawa*

**Lebanon**

Aghiad Al-Kutoubi, *Beirut*

**Libya**

Anuj Mishra, *Tripoli*

**Malaysia**

R Logeswaran, *Cyberjaya*
 Kwan-Hoong Ng, *Kuala Lumpur*

**Mexico**

Heriberto Medina-Franco, *Mexico City*

**Netherlands**

Jurgen J Fütterer, *Nijmegen*
 Raffaella Rossin, *Eindhoven*
 Paul E Sijens, *Groningen*

**New Zealand**

W Howell Round, *Hamilton*

**Norway**

Arne Sigmund Borthne, *Lørenskog*

**Saudi Arabia**

Mohammed Al-Omran, *Riyadh*
 Ragab Hani Donkol, *Abha*
 Volker Rudat, *Al Khobar*

**Serbia**

Djordjije Saranovic, *Belgrade*

**Singapore**

Uei Pua, *Singapore*
 Lim CC Tchoyoson, *Singapore*

**Slovakia**

František Dubecký, *Bratislava*

**South Korea**

Bo-Young Choe, *Seoul*
 Joon Koo Han, *Seoul*
 Seung Jae Huh, *Seoul*
 Chan Kyo Kim, *Seoul*
 Myeong-Jin Kim, *Seoul*
 Seung Hyup Kim, *Seoul*
 Kyoung Ho Lee, *Gyeonggi-do*
 Won-Jin Moon, *Seoul*
 Wazir Muhammad, *Daegu*
 Jai Soung Park, *Bucheon*
 Noh Hyuck Park, *Kyunggi*
 Sang-Hyun Park, *Daejeon*
 Joon Beom Seo, *Seoul*
 Ji-Hoon Shin, *Seoul*
 Jin-Suck Suh, *Seoul*
 Hong-Gyun Wu, *Seoul*



Spain

Eduardo J Aguilar, *Valencia*
 Miguel Alcaraz, *Murcia*
 Juan Luis Alcazar, *Pamplona*
 Gorka Bastarrika, *Pamplona*
 Rafael Martínez-Monge, *Pamplona*
 Alberto Muñoz, *Madrid*
 Joan C Vilanova, *Girona*



Switzerland

Nicolau Beckmann, *Basel*
 Silke Grabherr, *Lausanne*
 Karl-Olof Lövblad, *Geneva*
 Tilo Niemann, *Basel*
 Martin A Walter, *Basel*



Thailand

Sudsriluk Sampatchalit, *Bangkok*



Turkey

Olus Api, *Istanbul*
 Kubilay Aydin, *Istanbul*
 Işıl Bilgen, *Izmir*
 Zulkif Bozgeyik, *Elazig*
 Barbaros E Çil, *Ankara*
 Gulgun Engin, *Istanbul*
 M Fatih Evcimik, *Malatya*
 Ahmet Kaan Gündüz, *Ankara*
 Tayfun Hakan, *Istanbul*
 Adnan Kabaalioglu, *Antalya*
 Fehmi Kaçmaz, *Ankara*
 Musturay Karcaaltincaba, *Ankara*
 Osman Kizilkilic, *Istanbul*
 Zafer Koc, *Adana*
 Cem Onal, *Adana*
 Yahya Paksoy, *Konya*
 Bunyamin Sahin, *Samsun*
 Ercument Unlu, *Edirne*
 Ahmet Tuncay Turgut, *Ankara*
 Ender Uysal, *Istanbul*



United Kingdom

K Faulkner, *Wallsend*
 Peter Gaines, *Sheffield*
 Balaji Ganeshan, *Brighton*
 Nagy Habib, *London*
 Alan Jackson, *Manchester*
 Pradesh Kumar, *Portsmouth*
 Tarik F Massoud, *Cambridge*
 Igor Meglinski, *Bedfordshire*
 Robert Morgan, *London*
 Ian Negus, *Bristol*
 Georgios A Plataniotis, *Aberdeen*
 N J Raine-Fenning, *Nottingham*
 Manuchehr Soleimani, *Bath*
 MY Tseng, *Nottingham*
 Edwin JR van Beek, *Edinburgh*
 Feng Wu, *Oxford*



United States

Athanassios Argiris, *Pittsburgh*
 Stephen R Baker, *Newark*
 Lia Bartella, *New York*
 Charles Bellows, *New Orleans*
 Walter L Biffl, *Denver*
 Homer S Black, *Houston*
 Wessam Bou-Assaly, *Ann Arbor*
 Owen Carmichael, *Davis*
 Shelton D Caruthers, *St Louis*
 Yuhchayau Chen, *Rochester*
 Melvin E Clouse, *Boston*
 Ezra Eddy Wyssam Cohen, *Chicago*
 Aaron Cohen-Gadol, *Indianapolis*
 Patrick M Colletti, *Los Angeles*
 Kassa Darge, *Philadelphia*
 Abhijit P Datir, *Miami*
 Delia C DeBuc, *Miami*
 Russell L Deter, *Houston*
 Adam P Dicker, *Phil*
 Khaled M Elsayes, *Ann Arbor*
 Steven Feigenberg, *Baltimore*
 Christopher G Filippi, *Burlington*
 Victor Frenkel, *Bethesda*
 Thomas J George Jr, *Gainesville*
 Patrick K Ha, *Baltimore*
 Robert I Haddad, *Boston*
 Walter A Hall, *Syracuse*
 Mary S Hammes, *Chicago*

John Hart Jr, *Dallas*
 Randall T Higashida, *San Francisco*
 Juebin Huang, *Jackson*
 Andrei Iagaru, *Stanford*
 Craig Johnson, *Milwaukee*
 Ella F Jones, *San Francisco*
 Csaba Juhasz, *Detroit*
 Riyadh Karmy-Jones, *Vancouver*
 Daniel J Kelley, *Madison*
 Amir Khan, *Longview*
 Euishin Edmund Kim, *Houston*
 Vikas Kundra, *Houston*
 Kenneth F Layton, *Dallas*
 Rui Liao, *Princeton*
 CM Charlie Ma, *Philadelphia*
 Nina A Mayr, *Columbus*
 Thomas J Meade, *Evanston*
 Steven R Messé, *Philadelphia*
 Nathan Olivier Mewton, *Baltimore*
 Feroze B Mohamed, *Philadelphia*
 Koenraad J Morteale, *Boston*
 Mohan Natarajan, *San Antonio*
 John L Nosher, *New Brunswick*
 Chong-Xian Pan, *Sacramento*
 Dipanjan Pan, *St Louis*
 Martin R Prince, *New York*
 Reza Rahbar, *Boston*
 Carlos S Restrepo, *San Antonio*
 Veronica Rooks, *Honolulu*
 Maythem Saeed, *San Francisco*
 Edgar A Samaniego, *Palo Alto*
 Kohkan Shamsi, *Doylestown*
 Jason P Sheehan, *Charlottesville*
 William P Sheehan, *Willmar*
 Charles Jeffrey Smith, *Columbia*
 Monvadi B Srichai-Parsia, *New York*
 Dan Stoianovici, *Baltimore*
 Janio Szklaruk, *Houston*
 Dian Wang, *Milwaukee*
 Jian Z Wang, *Columbus*
 Shougang Wang, *Santa Clara*
 Wenbao Wang, *New York*
 Aaron H Wolfson, *Miami*
 Gayle E Woloschak, *Chicago*
 Ying Xiao, *Philadelphia*
 Juan Xu, *Pittsburgh*
 Benjamin M Yeh, *San Francisco*
 Terry T Yoshizumi, *Durham*
 Jinxing Yu, *Richmond*
 Jianhui Zhong, *Rochester*



EDITORIAL

- 126 TNM staging update for lung cancer: Why is this important?
Murchison JT

TOPIC HIGHLIGHT

- 128 The 7th lung cancer TNM classification and staging system: Review of the changes and implications
Mirsadraee S, Oswal D, Alizadeh Y, Caulo A, van Beek EJR

ORIGINAL ARTICLES

- 135 Reliable clinical and sonographic findings in the diagnosis of abdominal wall endometriosis near cesarean section scar
Francica G
- 141 Chest radiographic and computed tomographic manifestations in allergic bronchopulmonary aspergillosis
Agarwal R, Khan A, Garg M, Aggarwal AN, Gupta D
- 151 Primary malignant fibrous histiocytoma of the abdominal cavity: CT findings and pathological correlation
Karki B, Xu YK, Wu YK, Zhang WW

BRIEF ARTICLES

- 159 Multimodal morphometry and functional magnetic resonance imaging in schizophrenia and auditory hallucinations
García-Martí G, Aguilar EJ, Martí-Bonmati L, Escartí MJ, Sanjuán J
- 167 Virtual nonenhanced abdominal dual-energy MDCT: Analysis of image characteristics
Sosna J, Mahgerefteh S, Goshen L, Kafri G, Aviram G, Blachar A
- 174 ARFI elastography for the evaluation of diffuse thyroid gland pathology: Preliminary results
Sporea I, Sirli R, Bota S, Vlad M, Popescu A, Zosin I
- 179 Quantitative measurement of contrast enhancement of esophageal squamous cell carcinoma on clinical MDCT
Li R, Chen TW, Wang LY, Zhou L, Li H, Chen XL, Li CP, Zhang XM, Xiao RH

Contents

World Journal of Radiology
Volume 4 Number 4 April 28, 2012

ACKNOWLEDGMENTS I Acknowledgments to reviewers of *World Journal of Radiology*

APPENDIX I Meetings

I-V Instructions to authors

ABOUT COVER Mirsadraee S, Oswal D, Alizadeh Y, Caulo A, van Beek EJR. The 7th lung cancer TNM classification and staging system: Review of the changes and implications. *World J Radiol* 2012; 4(4): 128-134
<http://www.wjgnet.com/1949-8470/full/v4/i4/128.htm>

AIM AND SCOPE

World Journal of Radiology (*World J Radiol*, *WJR*, online ISSN 1949-8470, DOI: 10.4329) is a monthly peer-reviewed, online, open-access, journal supported by an editorial board consisting of 319 experts in radiology from 40 countries.

The major task of *WJR* is to rapidly report the most recent improvement in the research of medical imaging and radiation therapy by the radiologists. *WJR* accepts papers on the following aspects related to radiology: Abdominal radiology, women health radiology, cardiovascular radiology, chest radiology, genitourinary radiology, neuroradiology, head and neck radiology, interventional radiology, musculoskeletal radiology, molecular imaging, pediatric radiology, experimental radiology, radiological technology, nuclear medicine, PACS and radiology informatics, and ultrasound. We also encourage papers that cover all other areas of radiology as well as basic research.

FLYLEAF I-III Editorial Board

EDITORS FOR THIS ISSUE

Responsible Assistant Editor: *Jian-Xia Cheng*
Responsible Electronic Editor: *LJ Xiong*
Proofing Editor-in-Chief: *Lian-Sheng Ma*

Responsible Science Editor: *Jian-Xia Cheng*

NAME OF JOURNAL
World Journal of Radiology

ISSN
ISSN 1949-8470 (online)

LAUNCH DATE
December 31, 2009

FREQUENCY
Monthly

EDITING
Editorial Board of *World Journal of Radiology*,
Room 903, Building D, Ocean International Center,
No. 62 Dongsihuan Zhonglu, Chaoyang District,
Beijing 100025, China
Telephone: +86-10-59080039
Fax: +86-10-85381893
E-mail: wjr@wjgnet.com
<http://www.wjgnet.com>

EDITOR-IN-CHIEF
Filippo Cademartiri, MD, PhD, FESC, FSCCT,
Professor, Cardio-Vascular Imaging Unit-Giovanni
XXIII Hospital, Via Giovanni XXIII, 7-31050-Mo-
nastier di Treviso (TV), Italy

EDITORIAL OFFICE
Jian-Xia Cheng, Director
World Journal of Radiology
Room 903, Building D, Ocean International Center,
No. 62 Dongsihuan Zhonglu, Chaoyang District,
Beijing 100025, China
Telephone: +86-10-59080039
Fax: +86-10-85381893
E-mail: wjr@wjgnet.com
<http://www.wjgnet.com>

PUBLISHING
Baishideng Publishing Group Co., Limited,
Room 1701, 17/F, Henan Building,
No.90 Jaffe Road, Wanchai, Hong Kong, China
Fax: +852-31158812
Telephone: +852-58042046

PUBLICATION DATE
April 28, 2012

COPYRIGHT
© 2012 Baishideng. Articles published by this Open-Access journal are distributed under the terms of the Creative Commons Attribution Non-commercial License, which permits use, distribution, and reproduction in any medium, provided the original work is properly cited, the use is non commercial and is otherwise in compliance with the license.

SPECIAL STATEMENT
All articles published in this journal represent the viewpoints of the authors except where indicated otherwise.

INSTRUCTIONS TO AUTHORS
Full instructions are available online at http://www.wjgnet.com/1949-8470/g_info_20100316162358.htm.

ONLINE SUBMISSION
<http://www.wjgnet.com/1949-8470office>



TNM staging update for lung cancer: Why is this important?

John T Murchison

John T Murchison, Royal Infirmary of Edinburgh, Edinburgh EH13 0RA, Scotland, United Kingdom

Author contributions: Murchison JT solely contributed to this paper.

Correspondence to: Dr. John T Murchison, Consultant Radiologist, Royal Infirmary of Edinburgh, Edinburgh EH13 0RA, Scotland, United Kingdom. john.murchison@luht.scot.nhs.uk
Telephone: +44-131-242-3775 Fax: 44-131-2427773

Received: April 1, 2011 Revised: April 20, 2012

Accepted: April 27, 2012

Published online: April 28, 2012

Abstract

Cancer staging characterises the extent of disease facilitating selection of the most appropriate management and therapy and providing prediction of prognosis. As understanding of lung cancer evolves the opportunities arises to adjust disease staging. The adoption of the 7th edition tumour, node, metastasis staging system should result in improved treatment selection and more accurate prognostic information for the individual patient.

© 2012 Baishideng. All rights reserved.

Key words: Lung cancer; Tumour; Node; Metastasis; Staging

Murchison JT. TNM staging update for lung cancer: Why is this important? *World J Radiol* 2012; 4(4): 126-127 Available from: URL: <http://www.wjgnet.com/1949-8470/full/v4/i4/126.htm>
DOI: <http://dx.doi.org/10.4329/wjr.v4.i4.126>

Lung cancer is responsible for around 1.3 million deaths world-wide with its incidence still rising, particularly in women. Outlook for lung cancer patients remains poor with an over-all five year survival of around 15%. Correct staging is essential to tailor optimal management and choose the appropriate therapy with lowest mortality and morbidity for the individual patient. Staging also allows more accurate prediction of prognosis. Because the use

of staging systems allows continuity in data collection and temporal comparison such systems should not be altered without good cause. However novel technologies and the availability of computer aided data-sets on large surgical and non-surgical cohorts have enabled greater accuracy of outcome prediction, revealing potential areas for improvement in the lung cancer staging system, and as this new data on tumour biology and tumour response to therapy has become available honing of the system has become possible and the time has now been reached where an update of the staging system incorporating this knowledge is advisable. This update is more extensively discussed in the article by Mirsadraee *et al*^[1] in this issue of the *World Journal of Radiology*.

The lung cancer reflect the appropriate therapy and particularly whether a malignancy may be amenable to potentially curative surgery. Many details of the 7th edition^[2] are unchanged providing continuity with the 6th edition. The main changes are: a more precise characterisation of tumour size in T staging, differentiation of staging of satellite pulmonary nodules depending on their location and the differentiation of intrapulmonary from extrapulmonary metastatic disease. There has also been upstaging of some disease such as pleural and pericardial effusions where outcome data has shown involvement to result in poorer prognosis. Another development with version 7 is the recommendation for its use for staging of not just non-small cell lung cancer as with version 6 but also small cell lung cancer and carcinoid tumours. The revision of the lung cancer staging system is being overseen by the International Association for the Study of Lung Cancer.

This is an on-going project and version 7 does not include information from newer developments such as positron emission tomography-computed tomography (PET-CT) scanning. Data collection is already underway as part of the 7 year cycle in preparation for the 8th edition of the lung cancer tumour, node, metastasis (TNM) staging, which will very likely incorporate the PET-CT data that are now part of routine management in many countries.

The 7th edition TNM staging system is now in wide-

spread use and it is hoped that its introduction will result in better management of the individual patient and contribute to improved outcomes for patients who develop this common malignancy.

REFERENCES

1 **Mirsadraee S**, Oswal D, Alizadeh Y, Caulo A, van Beek EJ. R.

Murchison JT. Why has lung cancer staging changed?

The 7th lung cancer TNM classification and staging system: review of the changes and implications. *World J Radiol* 2012; **4**: 128-134

2 **Goldstraw P**, Crowley J, Chansky K, Giroux DJ, Groome PA, Rami-Porta R, Postmus PE, Rusch V, Sobin L. The IASLC Lung Cancer Staging Project: proposals for the revision of the TNM stage groupings in the forthcoming (seventh) edition of the TNM Classification of malignant tumours. *J Thorac Oncol* 2007; **2**: 706-714

S- Editor Cheng JX **L- Editor** A **E- Editor** Xiong L



The 7th lung cancer TNM classification and staging system: Review of the changes and implications

Saeed Mirsadraee, Dilip Oswal, Yalda Alizadeh, Andrea Caulo, Edwin JR van Beek

Saeed Mirsadraee, Andrea Caulo, Edwin JR van Beek, Clinical Research Imaging Centre, University of Edinburgh, Edinburgh EH16 4TJ, United Kingdom

Dilip Oswal, Department of Radiology, Mid Yorkshire NHS Trust, Wakefield WF1 4DG, United Kingdom

Yalda Alizadeh, Department of Pathology, Leeds Teaching Hospitals, Leeds LS9 7TF, United Kingdom

Author contributions: All authors have edited and reviewed the manuscript prior to submission.

Correspondence to: Dr. Saeed Mirsadraee, MD, PhD, FRCR, Senior Clinical Lecturer in Radiology, Honorary Consultant Radiologist, Clinical Research Imaging Centre, University of Edinburgh, 47 Little France Crescent, Edinburgh EH16 4TJ, United Kingdom. saeed.mirsadraee@ed.ac.uk

Telephone: +44-131-2427768 Fax: +44-131-2427773

Received: April 1, 2011 Revised: April 20, 2012

Accepted: April 27, 2012

Published online: April 28, 2012

© 2012 Baishideng. All rights reserved.

Key words: Lung neoplasms; Neoplasm staging; Lung cancer staging

Peer reviewers: James Chow, PhD, Radiation Physicist, Radiation Medicine Program, Princess Margaret Hospital, 610 University Avenue, Toronto, ON M5G 2M9, Canada; Francesco Lassandro, MD, Department of Radiology, Monaldi Hospital, Via Leonardo Bianchi, 80129 Napoli, Italy

Mirsadraee S, Oswal D, Alizadeh Y, Caulo A, van Beek EJR. The 7th lung cancer TNM classification and staging system: Review of the changes and implications. *World J Radiol* 2012; 4(4): 128-134 Available from: URL: <http://www.wjgnet.com/1949-8470/full/v4/i4/128.htm> DOI: <http://dx.doi.org/10.4329/wjr.v4.i4.128>

Abstract

Lung cancer is the most common cause of death from cancer in males, accounting for more than 1.4 million deaths in 2008. It is a growing concern in China, Asia and Africa as well. Accurate staging of the disease is an important part of the management as it provides estimation of patient's prognosis and identifies treatment strategies. It also helps to build a database for future staging projects. A major revision of lung cancer staging has been announced with effect from January 2010. The new classification is based on a larger surgical and non-surgical cohort of patients, and thus more accurate in terms of outcome prediction compared to the previous classification. There are several original papers regarding this new classification which give comprehensive description of the methodology, the changes in the staging and the statistical analysis. This overview is a simplified description of the changes in the new classification and their potential impact on patients' treatment and prognosis.

INTRODUCTION

Lung cancer is the most common cause of cancer deaths in males, accounting for 13% (1.6 million) of the total cancer cases and 18% (1.4 million) of the cancer deaths in 2008. Male lung cancer death rates are decreasing in the western world and increasing in China and several other countries in Asia and Africa. Female lung cancer death rates are increasing worldwide, with the exception of United States, Canada and Australia^[1-3].

Complete resection of lung cancer is associated with significantly longer survival remission but only about 25% of patients are candidates for surgical treatment at the time of diagnosis^[4]. Staging of cancer at the time of diagnosis is the most important predictor of survival, and treatments options should be based on the stage. Since the introduction of tumour, node, metastasis (TNM) staging by Pierre Denoix between the years 1943 and 1952, there have been significant changes including the TNM staging for lung cancer. The International Union Against Cancer (UICC) TNM Prognostic Factors Project

continued to develop the TNM classification as more data became available. The pocket book, “Livre de Poche”, was the first edition of the TNM classification and was published in 1968 and following several updates, the sixth edition was released in 2002. Like other tumours, lung cancer classification and staging assess the anatomical extension of the tumor which is critical to choosing a therapy and provides information on prognosis^[5-9].

The International Association for the Study of Lung Cancer (IASLC) announced a major revision of the TNM staging system for lung cancer^[10]. This has been included in the seventh edition of the “TNM classification of malignant tumours” published by the UICC in January 2010 (Table 1). The previous latest update of the classification was based on a predominantly surgical database of 5319 patients from a single centre in the United States from 1972 to 1988^[11]. The database was small and old and there was little internal and no external validation of stage groupings relating to these data and given the fact that this is the commonest cause for cancer related death, a major revision of the staging was long overdue and became possible with the availability of multicentre and larger cohorts of patients being treated for lung cancer.

Traditionally the TNM classification has been used for non-small-cell lung cancer (NSCLC). Even though the TNM classification was applicable to the small-cell lung cancer (SCLC), this was not practiced. SCLC was classified as “local” and “extensive” disease. The new classification is also applicable to both types of lung cancers^[12].

Imaging has a fundamental role in staging of the lung cancer. As imaging techniques have improved especially in terms of resolution and speed for CT scans and as newer techniques like positron emission tomography (PET) have become established in the routine clinical practice, consideration needed to be given to revising the classification and staging of lung cancer. The new classification has led to alteration in treatment options and in predicting the prognosis.

The staging of lung cancer can be clinical or pathological (also known as surgical). Clinical staging involves radiological studies (plain radiographs and CT scan).

Currently, PET (Figure 1) is routinely used in many centres as an additional diagnostic tool which may change the clinical stage of the disease in a given patient. PET often upstages the disease (in comparison to conventional CT scan) by identifying newer, metabolically active sites of disease (Figure 2). In a minority of cases, it downstages the disease (Figure 3). However, it must be noted that the database analysed for the 7th TNM classification did not include any data from PET studies. Surgical staging refers to pathological staging following surgery or tissue biopsy (e.g., *via* endoscopical techniques). In addition to T, N and M descriptors, the pathological staging also involves description of resection margins which is indicated as R0 or R1 (R0 is resection margins clear of the malignancy and R1 is involved margins). Following pathological staging, the T, N and M become pT, pN and pM. Obviously, this may result in either upward or

downward alteration of clinical staging. The overall level of agreement between clinical and pathological systems is reported to be only 35%-55%^[13].

The aim of this overview is to discuss the basis for the changes in the 7th classification of lung cancer and its impact on predicting patients’ prognosis. Potential limitations of the classification and future directions are discussed.

APPROACH TO DEVELOPMENT OF THE 7TH TNM CLASSIFICATION

A retrospective international lung cancer database was developed from 46 sources in more than 19 countries with staging and outcome data on 100 869 lung cancer cases managed between 1990 and 2000. After applying exclusion criteria, 81 015 cases remained for analysis. Of these, 67 725 were NSCLC and 13 290 were SCLC. Only the NSCLC cases were included in the analyses of the T, N and M descriptors and the subsequent analysis of TNM subsets and stage groupings^[10]. From 67 725 NSCLC cases, 38265 were clinically without metastases, and 28 371 had pathological staging (defined at thoracotomy). Survival was estimated by the Kaplan-Meier method. Prognostic groups were assessed by Cox regression analysis after adjustment for cell type, sex, age and region, using the SAS System for Windows Version 9.0 PHREG procedure^[10,14].

New tumour staging

The T staging is determined by the size of primary tumour in long axis, or direct extent of the tumour into adjacent structures such as mediastinum or chest wall.

Main changes in staging classification are reflected in the T staging. These changes are largely related to the re-classification of the size and location of the primary tumour and satellite nodules (Table 2).

The former staging system divided tumours into two size groups with 3 cm as the cut off point. The new system has 5 size-based categories with cut-off points at 2, 3, 5 and 7 cm. Tumours measuring < 2 cm are classified as T1a, whereas those measuring 2-3 cm are classified as T1b. T2 disease is also subdivided into T2a (> 3 - 5 cm) and T2b (> 5 cm - 7cm). The tumours larger than 7 cm are now classified as T3. The additional cut-off points changes may alter treatment recommendations.

The new classification does not take into account a single tumour which involves two lobes across a fissure. It only considers the tumour size and satellite (non-contagious) nodules in the same and different lobes. Patients previously considered T4 if additional tumour nodules were found in the same lobe are now classified as T3. Additional tumour nodules outside the primary lobe but in the same lung, are now down staged from M1 to T4 and they may be suitable for a pneumonectomy. Classification for a satellite nodule in the contralateral lung has changed from M1 to M1a to indicate intrathoracic spread, which has a slightly favourable prognosis compared to patients

Table 1 Seventh tumour, node, metastasis classification of lung cancer: January 2010^[10]

T: Tumour	
TX	Primary tumour cannot be assessed, or tumour proven by the presence of malignant cells in sputum or bronchial washings but not visualized by imaging or bronchoscopy
T0	No evidence of primary tumour
Tis	Carcinoma <i>in situ</i>
T1	Tumour < 3 cm in greatest dimension, surrounded by lung or visceral pleura, without bronchoscopic evidence of invasion more proximal than the lobar bronchus (i.e., not in the main bronchus)
T1a	Tumour < 2 cm in greatest dimension
T1b	Tumour > 2 cm but < 3 cm in greatest dimension
T2	Tumour > 3 cm but < 7 cm or tumour with any of the following features (T2 tumours with these features are classified T2a if < 5 cm): Involves main bronchus, > 2 cm distal to the carina Invades visceral pleura Associated with atelectasis or obstructive pneumonitis that extends to the hilar region but does not involve the entire lung
T2a	Tumour > 3 cm but < 5 cm in greatest dimension
T2b	Tumour > 5 cm but < 7 cm in greatest dimension
T3	Tumour > 7 cm or one that directly invades any of the following: Chest wall (including superior sulcus tumours), diaphragm, phrenic nerve, mediastinal pleura, parietal pericardium Tumour in the main bronchus < 2 cm distal to the carina but without involvement of the carina Associated atelectasis or obstructive pneumonitis of the entire lung Separate tumour nodule(s) in the same lobe
T4	Tumour of any size that invades any of the following: Mediastinum, heart, great vessels, trachea, recurrent laryngeal nerve, esophagus, vertebral body, carina Separate tumour nodule(s) in a different ipsilateral lobe
N: Nodes	
NX	Regional lymph nodes cannot be assessed
N0	No regional lymph node metastasis
N1	Metastasis in ipsilateral peribronchial and/or ipsilateral hilar lymph nodes and intrapulmonary nodes, including involvement by direct extension
N2	Metastasis in ipsilateral mediastinal and/or subcarinal lymph node(s)
N3	Metastasis in contralateral mediastinal, contralateral hilar, ipsilateral or contralateral scalene, or supraclavicular lymph node(s)
M: Metastases	
MX	Distant metastasis cannot be assessed
M0	No distant metastasis
M1	Distant metastasis
M1a	Separate tumour nodule(s) in a contralateral lobe tumour with pleural nodules or malignant pleural/ pericardial effusion
M1b	Distant metastasis

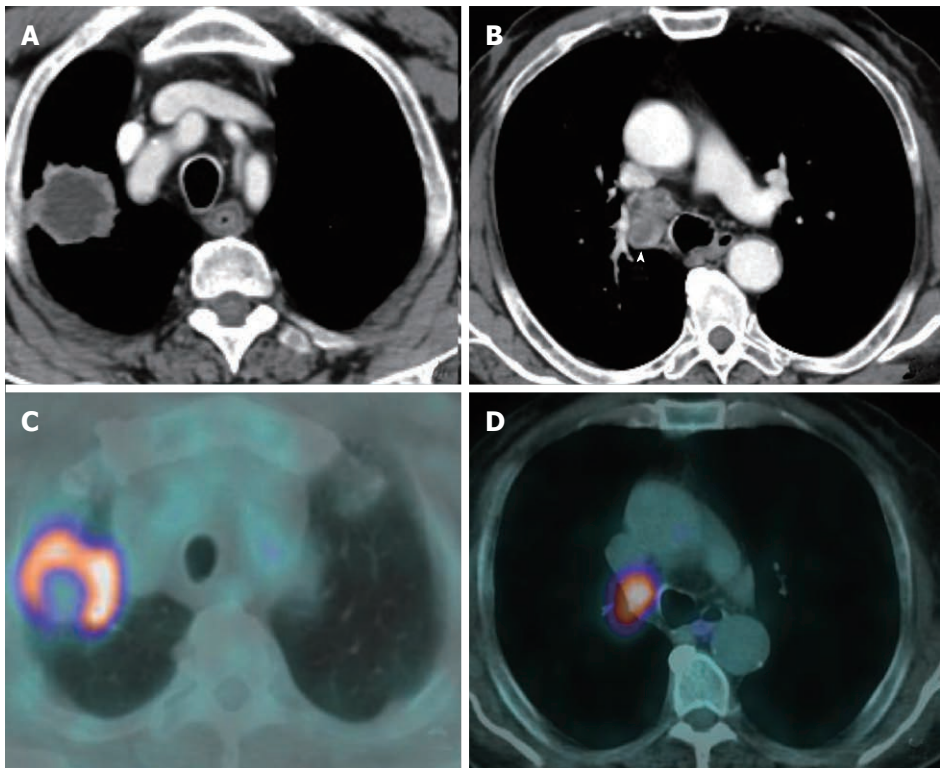


Figure 1 Contrast enhanced computed tomography of the chest viewed with mediastinal window settings demonstrated a large necrotic mass in the right upper lobe (A) with enlarged necrotic paratracheal lymph nodes in station 4R (arrowhead) (B). C, D: Positron emission tomography-computed tomography demonstrated high [18F]-2-fluoro-2-deoxy-d-glucose uptake in the mass and lymph nodes confirming a T2aN2 lung cancer.

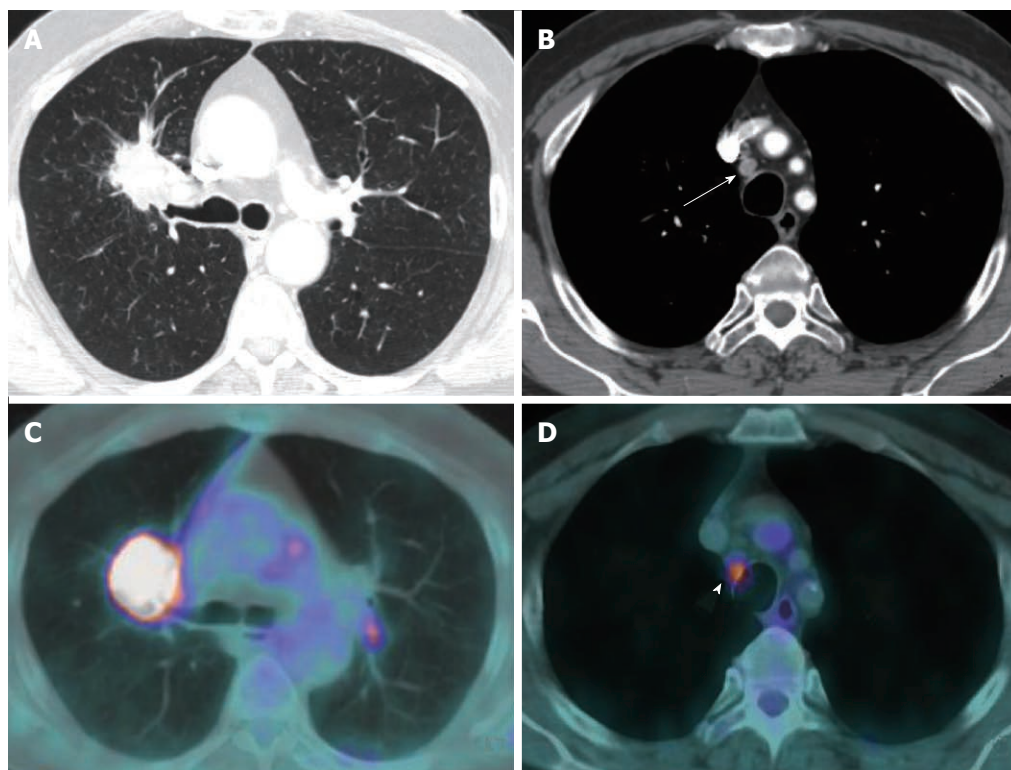


Figure 2 Contrast enhanced thoracic computed tomography viewed with lung window settings shows a 5.2 cm ill-defined mass suspected of lung cancer abutting the right lung hilum, causing narrowing of the upper lobe bronchus (A). B: Review of images on mediastinal window settings showed a paratracheal lymph node with short axis smaller than 1 cm (arrow) in station 2R; C and D: Positron emission tomography-computed tomography demonstrated a high [18F]-2-fluoro-2-deoxy-d-glucose-uptake of both mass and 2R node (arrowhead), resulting in an up-staging of the disease from T2bN1 (CT classification) to T2bN2. This finding was further confirmed by mediastinoscopy sampling.

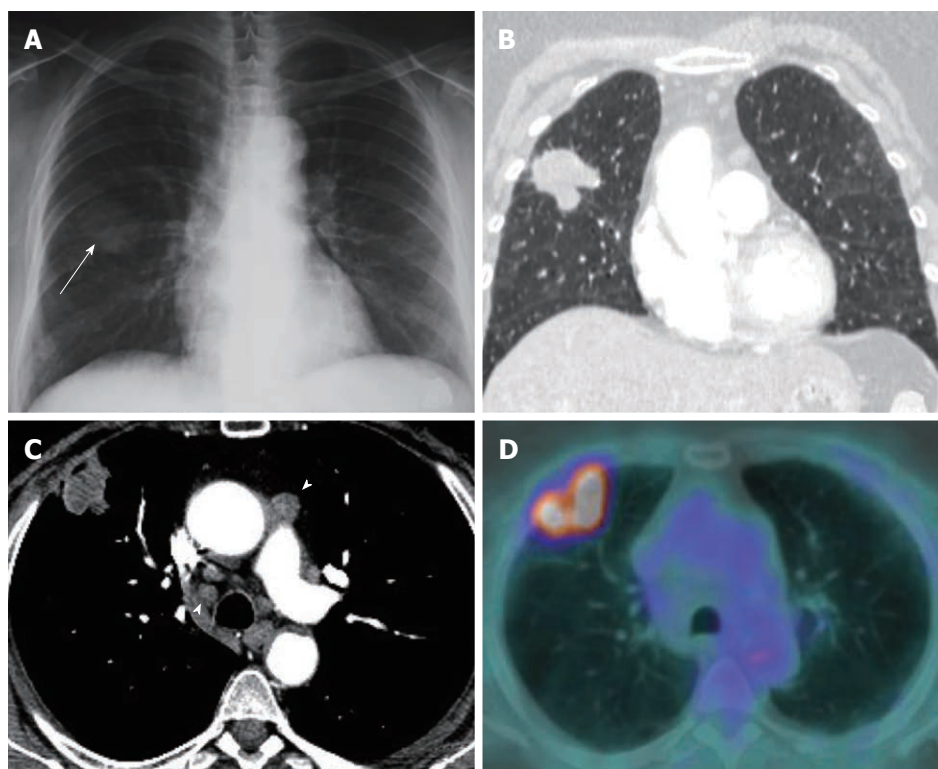


Figure 3 Example of cross sectional imaging nodal staging pitfalls. A: A mass of the right lung (arrow) was identified on chest radiograph. B: A 4 cm spiculated mass suspected of lung cancer in the right upper lobe was confirmed by computed tomography (CT); C, D: Contrast enhanced CT demonstrated enlarged lymph nodes (> 1 cm in short axis; arrowheads) in ipsi- and contra-lateral mediastinal nodal stations (C) (T2aN3), positron emission tomography-computed tomography (PET-CT) (D) showed high metabolic activity of the parenchymal lesion but no nodal [18F]-2-fluoro-2-deoxy-d-glucose uptake (PET-CT staging: T2aN0M0). No metastatic nodes were demonstrated by endoscopic ultrasound-needle aspiration and mediastinoscopy, and surgical staging was in full agreement with PET-CT (pT2N0 adenocarcinoma).

Table 2 Summary of what has changed

Feature	Old - sixth classification 2002-2009	Current, new - seventh classification - Jan 2010
Tumour < 2 cm	T1	T1a
Tumour > 2 but < 3 cm	T1	T1b
Tumour > 3 cm but < 5 cm	T2	T2a
Tumour > 5 but < 7 cm	T2	T2b
Tumour > 7 cm	T2	T3
Tumour - same lobe nodules	T4	T3
Ipsilateral lung nodule - non primary lobe	M1	T4
Malignant pleural effusion	T4	M1a
Contralateral lung nodule	M1	M1a
Distant metastases	M1	M1b

with distant metastases (M1b). Figures 4 to 6 show examples of cases in whom the new T classification has changed the staging.

New node staging

The N classification describes the degree of spread to regional lymph nodes. This remained unchanged in the 7th edition as the new data showed no change in node staging related survival.

The regional nodal classification for lung cancer was described by Mountain and Dresler (1997)^[15]. Various techniques are used to identify nodal spread. Previous studies showed that the sensitivity and specificity of CT and PET for predicting malignant involvement of mediastinal lymph nodes were 60% and 81%, and 84% and 89%, respectively^[16]. Lymph node sampling is regarded as the most accurate predictor of nodal status. Mediastinoscopy has been regarded as the “gold standard” for staging of the mediastinum, but it is invasive and has limitations in accessing to the posterior and inferior mediastinal nodes. Furthermore, the sensitivity for mediastinoscopy is still only 80%-90%, and, in 10%-15% of cases, the technique returns a false-negative diagnosis^[17,18].

Endobronchial ultrasound-guided transbronchial needle biopsy (EBUS-TBNA) is reported to have a sensitivity of 85% and a negative predictive value of 90%^[19]. Similarly, Rintoul *et al*^[20] reported a sensitivity, specificity and accuracy of 85%, 100% and 89%, respectively for EBUS-TBNA. They also suggested that a combined EBUS and oesophageal endoscopic ultrasound (EUS) allows better access to the mediastinal and hilar lymph nodes than is usually accessible by mediastinoscopy^[20]. A further study of 150 consecutive lung cancer patients reported that combination of EUS fine needle aspiration (EUS-FNA) and EBUS-TBNA had higher sensitivity (93%) and higher negative predictive value (97%), when compared to that of each technique^[21]. This however needs to be highlighted that not all lymphnode stations are not accessible by EUS techniques.

New metastasis staging

The M staging defines the presence of metastases beyond regional lymph nodes. In the 7th edition of the lung can-

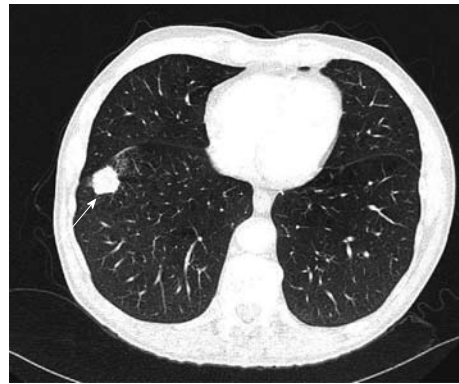


Figure 4 A 2.5 cm mass (arrow) in the right lower lobe was classified as T1 in 6th edition and is described as T1b in the 7th classification. This did not change the staging (see Table 3).



Figure 5 A 7.5 cm necrotic mass in the right lower lobe (arrow). As far as size is concerned, the T classification is upstaged from T2 to T3 and therefore a worse prognosis is expected.

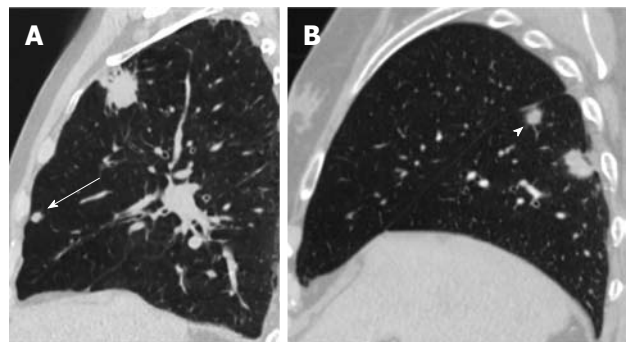


Figure 6 Example of change in classification status. A: A mass in the right upper lobe and a satellite nodule (arrow) in the right middle lobe. This tumour is reclassified from M1 to T4. Patient may be considered for treatment (e.g., pneumonectomy) and a better prognosis is to be expected; B: A tumour with a satellite nodule (arrowhead) both in right lower lobe; this was therefore downstaged from T4 to T3 in the new classification and surgical treatment was considered.

cer classification, the pleural or pericardial dissemination (effusions or nodules) are no longer classified T4, but are now upstaged into a new category (M1a). This category also includes additional nodules that are found in the contralateral lung. Distant metastasis is sub-classified as M1b disease.

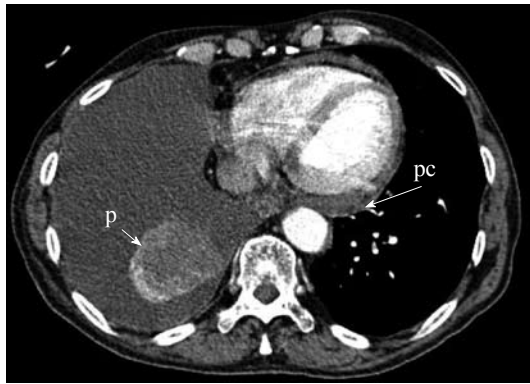


Figure 7 A patient with a necrotic mass in the right lower lobe (short arrow). As seen in this axial contrast enhanced computed tomography, there is pleural (p) and pericardial (pc) effusions which were confirmed to be malignant. This will be re-classified from T4 to M1a indicating worse estimated prognosis.

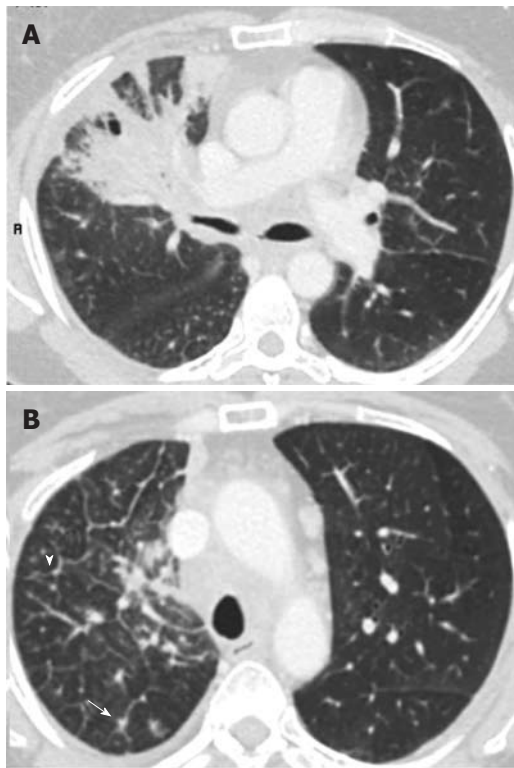


Figure 8 Lymphangitis caused by a large right upper lobe mass, note thickening of interlobular septa (arrowhead) and peribronchovascular nodules (arrow). There is no provision for lymphangitis in the tumour, node, metastasis classification.

M1a includes malignant pleural effusion (with median overall survival of 8 mo in 488 patients) and contralateral lung nodules, which had overall survival of 10 mo in 362 patients. M1b refers to extra-thoracic metastases and median overall survival was 6 mo ($n = 4343$). This contrasts with 13 mo overall median survival in T4M0 any N group ($n = 399$)^[22]. Figure 7 shows an example in which the new TNM classification has changed the T and M staging.

Impact of new staging system on patient management

The revised lung cancer staging based on the new TNM

Table 3 Changes in the staging of lung cancer based on the new tumour, node, metastasis classification: Cells in the bold indicate a change from the sixth edition for a tumour, node, metastasis category^[10]

Old- sixth edition-descriptor	New seventh edition-descriptor	N0	N1	N2	N3
T1 (≤ 2 cm)	T1a	I A	II A	III A	III B
T1 ($> 2-3$ cm)	T1b	I A	II A	III A	III B
T2 (≤ 5 cm)	T2a	I B	II A	III A	III B
T2 ($> 5-7$ cm)	T2b	II A	II B	III A	III B
T2 (> 7 cm)	T3	II B	III A	III A	III B
T3 (invasion)	T3	II B	III A	III A	III B
T4 (same lobe nodule)	T3	II B	III A	III A	III B
T4 (extension)	T4	III A	III A	III B	III B
M1 (ipsilateral non primary lobe nodule)	T4	III A	III A	III B	III B
T4 (pleural effusion)	M1a	IV	IV	IV	IV
M1 (contralateral lung nodule)	M1a	IV	IV	IV	IV
M1 (distant metastases)	M1b	IV	IV	IV	IV

classification is shown in Table 3^[10].

New staging is based on analyzing survival in large databases based on tumour size and disease proliferation and therefore is expected to assess an individual patient's prognosis more accurately. Many patients will receive a different staging category based on the 7th edition of the TNM staging system. Those who are down-staged because additional tumours are found in the same lobe as the primary tumour may now be considered candidates for adjunctive chemotherapy along with surgery. Similarly, there may be a greater role for surgery in patients with metastatic nodules in the ipsilateral, non-primary lobe who previously would have been assigned a stage IV diagnosis, but are now stage III A.

Those patients who undergo biopsy or surgical resection of the tumour and/or lymph nodes may have their TNM classification revised based on histological findings. The clinical staging of the patient thus changes into pathological staging and is described by adding prefix "p" e.g., T1b N1 M0 may become pT2a pN2 M0 based on pathological measurements and findings, and these would influence treatment strategies and estimated prognosis.

Limitations of new classification

There are glaring deficiencies in the global distribution of the data with no data at all being included from Africa, South America or the Indian subcontinent. Other vast countries such as Russia, China, and Indonesia are not represented or only poorly represented^[10]. Moreover, the database used for the 7th edition of lung staging classification (1990-2000) predates the widespread and routine use of PET which has had an enormous impact on clinical staging algorithms^[10].

Lymphangitis carcinomatosa (Figure 8) is believed to be associated with worse prognosis in lung cancer patients. However, there is no evidence to support this. The new TNM classification does not specifically take account of lymphangitis.

WHAT NEXT FOR LUNG CANCER STAGING?

The process by which TNM classification in lung cancer evolves has been changed irrevocably, and the IASLC has secured a central role in future revisions for the whole of the thoracic oncology community. The IASLC proposes to improve on the above described limitations, especially those relating to PET-CT scanning, in time for the 8th edition of TNM classification. A prospective data set has been agreed, funding has been secured for the 7-year cycle leading up to the 8th edition. A web-based data collection system is being developed and tested to make data submission easier for those who collaborate in this next phase. Data collection has been expanded to incorporate neuro-endocrine tumours and mesothelioma^[23].

REFERENCES

- 1 Mortality Statistics: Deaths registered in England and Wales (Series DR), 2009. Available from: URL: <http://www.ons.gov.uk/ons/rel/vsob1/mortality-statistics--deaths-registered-in-england-and-wales--series-dr-/2009/index.html>
- 2 Jemal A, Bray F, Center MM, Ferlay J, Ward E, Forman D. Global cancer statistics. *CA Cancer J Clin* 2011; **61**: 69-90
- 3 Ferlay J, Shin HR, Bray F, Forman D, Mathers C, Parkin DM. GLOBOCAN 2008 Cancer Incidence and Mortality Worldwide: IARC CancerBase No. 10. Lyon, France: International Agency for Research on Cancer, 2011. Available from: URL: <http://globocan.iarc.fr>. Last accessed 17/02/2011
- 4 Rami-Porta R, Crowley JJ, Goldstraw P. The revised TNM staging system for lung cancer. *Ann Thorac Cardiovasc Surg* 2009; **15**: 4-9
- 5 Sobin LH, Wittekind CH. TNM classification of malignant tumours. 6th ed. Hoboken, NJ: John Wiley&Sons, 2002
- 6 Denoix PF. Tumor, Node and Metastasis (TNM). *Bull Inst. Nat Hyg (Paris)* 1944; **1**: 69
- 7 Denoix PF. Tumor, Node and Metastasis (TNM). *Bull Inst. Nat Hyg (Paris)* 1944; **2**: 82
- 8 Denoix PF. Tumor, Node and Metastasis (TNM). *Bull Inst. Nat Hyg (Paris)* 1950; **5**: 81
- 9 Denoix PF. Tumor, Node and Metastasis (TNM). *Bull Inst. Nat Hyg (Paris)* 1952; **7**: 743
- 10 Goldstraw P, Crowley J, Chansky K, Giroux DJ, Groome PA, Rami-Porta R, Postmus PE, Rusch V, Sobin L, International Association for the Study of Lung Cancer International Staging Committee, Participating Institutions. The IASLC Lung Cancer Staging Project: proposals for the revision of the TNM stage groupings in the forthcoming (seventh) edition of the TNM Classification of malignant tumours. *J Thorac Oncol* 2007; **2**: 706-714
- 11 Mountain CF. Revisions in the International System for Staging Lung Cancer. *Chest* 1997; **111**: 1710-1717
- 12 Shepherd FA, Crowley J, Van Houtte P, Postmus PE, Carney D, Chansky K, Shaikh Z, Goldstraw P, International Association for the Study of Lung Cancer International Staging Committee and Participating Institutions. The International Association for the Study of Lung Cancer lung cancer staging project: proposals regarding the clinical staging of small cell lung cancer in the forthcoming (seventh) edition of the tumor, node, metastasis classification for lung cancer. *J Thorac Oncol* 2007; **2**: 1067-1077
- 13 López-Encuentra A, García-Luján R, Rivas JJ, Rodríguez-Rodríguez J, Torres-Lanza J, Varela-Simo G. Comparison between clinical and pathologic staging in 2,994 cases of lung cancer. *Ann Thorac Surg* 2005; **79**: 974-979; discussion 979
- 14 Groome PA, Bolejack V, Crowley JJ, Kennedy C, Krasnik M, Sobin LH, Goldstraw P, IASLC International Staging Committee, Cancer Research and Biostatistics; Observers to the Committee, Participating Institutions. The IASLC Lung Cancer Staging Project: validation of the proposals for revision of the T, N, and M descriptors and consequent stage groupings in the forthcoming (seventh) edition of the TNM classification of malignant tumours. *J Thorac Oncol* 2007; **2**: 694-705
- 15 Mountain CF, Dresler CM. Regional lymph node classification for lung cancer staging. *Chest* 1997; **111**: 1718-1723
- 16 Toloza EM, Harpole L, Detterbeck F, McCrory DC. Invasive staging of non-small cell lung cancer: a review of the current evidence. *Chest* 2003; **123**: 157S-166S
- 17 Luke WP, Pearson FG, Todd TR, Patterson GA, Cooper JD. Prospective evaluation of mediastinoscopy for assessment of carcinoma of the lung. *J Thorac Cardiovasc Surg* 1986; **91**: 53-56
- 18 Coughlin M, Deslauriers J, Beaulieu M, Fournier B, Piroux M, Rouleau J, Tardif A. Role of mediastinoscopy in pretreatment staging of patients with primary lung cancer. *Ann Thorac Surg* 1985; **40**: 556-560
- 19 Ømark Petersen H, Eckardt J, Hakami A, Olsen KE, Jørgensen OD. The value of mediastinal staging with endobronchial ultrasound-guided transbronchial needle aspiration in patients with lung cancer. *Eur J Cardiothorac Surg* 2009; **36**: 465-468
- 20 Rintoul RC, Skwarski KM, Murchison JT, Wallace WA, Walker WS, Penman ID. Endobronchial and endoscopic ultrasound-guided real-time fine-needle aspiration for mediastinal staging. *Eur Respir J* 2005; **25**: 416-421
- 21 Wallace MB, Pascual JM, Raimondo M, Woodward TA, McComb BL, Crook JE, Johnson MM, Al-Haddad MA, Gross SA, Pungpapong S, Hardee JN, Odell JA. Minimally invasive endoscopic staging of suspected lung cancer. *JAMA* 2008; **299**: 540-546
- 22 Postmus PE, Brambilla E, Chansky K, Crowley J, Goldstraw P, Patz EF, Yokomise H. The IASLC Lung Cancer Staging Project: proposals for revision of the M descriptors in the forthcoming (seventh) edition of the TNM classification of lung cancer. *J Thorac Oncol* 2007; **2**: 686-693
- 23 Goldstraw P. The 7th Edition of TNM in Lung Cancer: what now? *J Thorac Oncol* 2009; **4**: 671-673

S- Editor Cheng JX L- Editor A E- Editor Xiong L



Reliable clinical and sonographic findings in the diagnosis of abdominal wall endometriosis near cesarean section scar

Giampiero Francica

Giampiero Francica, Unit of Diagnostic and Interventional ultrasound, Camilliani Hospital, "S. Maria della Pietà", S. Rocco St. 9, 80026 Casoria, Italy

Author contributions: Francica G designed the study, performed the research, analyzed the data, and drafted the manuscript.

Correspondence to: Dr. Giampiero Francica, Unit of Diagnostic and Interventional Ultrasound, Presidio Ospedaliero Camilliani, "S. Maria della Pietà", via S. Rocco 9, 80026 Casoria, Italy. giampierofrancica@gmail.com

Telephone: +39-81-5408262 Fax: +39-81-7586638

Received: October 28, 2011 Revised: March 23, 2012

Accepted: March 30, 2012

Published online: April 28, 2012

Abstract

AIM: To highlight sonographic and clinical characteristics of scar endometrioma with special emphasis on size-related features.

METHODS: Thirty women (mean age 30.6 years, range 20-42 years) with 33 scar endometriomas (mean diameter 27.1 mm, range 7-60 mm) were consecutively studied by Sonography and Color Doppler examination prior to surgery. Pathological examination was available in all cases.

RESULTS: The most frequent (24 of 33 nodules, 74%) sonographic B-mode aspect of endometrioma was that of an inhomogeneously hypoechoic roundish nodule with fibrotic changes (in the form of hyperechoic spots or strands), a peripheral inflammatory hyperechoic ring, spiculated margins and a single vascular pedicle entering the mass at the periphery. On average, 1.6 cesarean sections were recorded per patient (range 1-3). The median interval between the last cesarean section and admission to hospital was 36 mo (range 12-120 mo) and the median duration of symptoms before admission was 25.7 mo (range 0.5-80 mo). 13 patients had 13

large endometriomas (≥ 30 mm) with a mean lesion diameter of 41.3 ± 9.02 mm (range 30-60 mm). Seventeen women had 20 small endometriomas with a mean lesion size of 18.2 ± 5.17 mm (range 7-26 mm). The mean interval between the last cesarean section and admission to hospital (66.0 mo vs 39.6 mo, $P < 0.01$) and the mean duration of symptoms before admission (43.0 mo vs 17.4 mo, $P < 0.01$) were significantly longer in patients with large endometriomas; in addition, a statistically significant higher percentage of patients with large implants had undergone previous inconclusive diagnostic examinations, including either computed tomography/magnetic resonance imaging/fine needle biopsy/laparoscopy (38.4% vs 0%, $P < 0.05$). On sonography, large endometriomas showed frequent cystic portions and fistulous tracts ($P < 0.02$), loss of round/oval shape ($P < 0.04$) along with increased vascularity ($P < 0.04$).

CONCLUSION: Endometrioma near cesarean section scar is an often neglected disease, but knowledge of its clinical and sonographic findings may prevent a delay in diagnosis that typically occurs in patients with larger (≥ 3 cm) endometriomas.

© 2012 Baishideng. All rights reserved.

Key words: Cesarean section scar; Endometrioma; Ultrasound

Peer reviewers: Ragab Hani Donkol, Professor, Radiology Department, Aseer Central Hospital, 34 Abha, Saudi Arabia; Jacob Sosna, MD, Section Chief, CT, Director of Research and Imaging Laboratories Department of Radiology, Hadassah Hebrew University Medical Center, Jerusalem 91120, Israel

Francica G. Reliable clinical and sonographic findings in the diagnosis of abdominal wall endometriosis near cesarean section scar. *World J Radiol* 2012; 4(4): 135-140 Available from: URL: <http://www.wjgnet.com/1949-8470/full/v4/i4/135.htm> DOI: <http://dx.doi.org/10.4329/wjr.v4.i4.135>

INTRODUCTION

Subcutaneous endometriosis near cesarean delivery scar (so-called “scar endometrioma”) is a rare form of extra-pelvic endometriosis, occurring in 0.03% to 1.5% of all women who have had cesarean deliveries^[1-6]. Although for extrapelvic endometriosis it has been suggested that multipotential mesenchymal cells may undergo metaplasia into endometriosis, in the case of endometrioma near a Pfannenstiel incision, the most likely explanation is inadvertent transportation of endometrial cells during cesarean section^[7-9]. An iatrogenic origin has also been proposed in the case of endometriotic implants occurring after hysterectomy^[9], appendectomy^[3], laparoscopic trocar tract^[10], needle tract amniocentesis^[11] and perineal episiotomy incision^[12].

On a clinical basis, the most typical finding is a palpable small mass near the cesarean section scar becoming painful with menses^[3,13,14].

However, the comparative rarity of scar endometrioma may represent a major factor explaining why the correct diagnosis is frequently overlooked by both clinicians^[15] and radiologists^[13,16]. Moreover, endometriosis of the abdominal wall may be a diagnostic challenge since a variety of pathologic conditions (a suture granuloma, an incisional hernia, a primary or metastatic cancer) should be taken into account in the differential diagnosis^[13,16].

The aim of this study was to report on a large series of scar endometriomas by highlighting the clinical and sonographic characteristics of this neglected disease.

MATERIALS AND METHODS

Thirty women (mean age 30.6 years, range 20-42 years) with 33 scar endometriomas were consecutively seen at the Ultrasound Unit between June 1999 and April 2010. All of the patients underwent wide surgical excision and pathologic analysis of all surgical specimens was available.

In each patient the following parameters were determined: (1) historical data: number of cesarean sections, time from both last cesarean section and onset of symptoms before admission, known pelvic endometriosis, inconclusive previous diagnostic exams other than sonography [computed tomography (CT), magnetic resonance imaging (MRI), fine needle biopsy (FNB), laparoscopy], previous pelvic/abdominal surgery related to painful symptoms, characteristics of pain (cyclic with menses *vs* continuous); (2) clinical data: physical examination at entry (palpability of nodule/s); and (3) sonographic and color doppler findings: lesion size, site, echotexture, margins, presence of vascular pedicle/s, presence of central vascularity and values of resistive index (RI) of arterial flow.

In all patients, sonographic examination was carried out by a single operator (Francica G) with high frequency probes (7.5 MHz up to 12 MHz) with the sonographic machines available over the study time period (Logic 500, Logic 700 Expert Series, Logic 7, Logic 9, GE Healthcare, Milwaukee, WI, USA). After 2004, only high-frequency wide band electronic transducers along with

spatial compound and tissue harmonic imaging modalities were used.

Color Doppler parameters were set to detect low blood flow velocities (PRF 500-1000 Hz, Wall filter 50 Hz, High filters for color-*vs*-echo priority and color persistence); RI of arterial flow (if detectable) was expressed as the mean of 2 measurements.

For the purpose of comparison, a large scar endometrioma was considered if the widest nodule diameter was equal to or greater than 30 mm.

Fisher's exact test and χ^2 test for categorical data and the unpaired *t*-test for continuous variables were used for statistical analysis. *P* values < 0.05 were considered statistically significant.

The institutional ethics committee of the author's hospital approved the study design, and written consent to participate in the study was obtained from all patients.

RESULTS

The 33 endometriomas had a mean diameter of 27.1 mm (range 7-60 mm); twenty-six nodules (78.7%) were located between subcutaneous fat and the muscular sheath; in three cases (9.1%) both the subcutaneous and muscular plane were infiltrated; two endometriomas (6.1%) were purely subcutaneous and two more nodules (6.1%) were entrapped in the muscular layer of the abdominal wall. Endometriomas did not show a preferential distribution along the incision scar: 16 nodules were located on the right, 14 on the left and 3 on the midline.

Thirteen patients (43%) had 13 large endometriomas (≥ 30 mm) with a mean lesion diameter of 41.3 ± 9.02 mm (range 30-60 mm). Seventeen women (56.7%) had 20 small endometriomas with a mean lesion size of 18.2 ± 5.17 mm (range 7-26 mm). One subject had a 10-mm satellite nodule near the largest endometrioma of this series (60 mm).

Clinical findings

On average, 1.6 cesarean sections were recorded per patient (range 1-3). The median interval between the last cesarean section and admission to hospital was 36 mo (range 12-120 mo) and the median duration of symptoms before admission was 25.7 mo (range 0.5-80 mo). A history of previous pelvic endometriosis was rarely reported (two cases, 6.6%). At entry, abdominal wall lesions were palpable in all cases but one, an obese patient with a 7-mm nodule. Cyclic pain with menses associated with a palpable mass was recorded in 24 cases (80%); in the remaining 6 patients, pain was described as continuous.

In Table 1, the clinical and demographic findings are shown according to endometrioma size.

Patients with endometriomas larger than 3 cm had a longer mean interval between the last cesarean section and admission to hospital (66.0 mo *vs* 36 mo, *P* < 0.01) and mean duration of symptoms before admission (43.0 mo *vs* 17.4 mo, *P* < 0.01) when compared with patients bearing smaller endometriomas. In addition, a statistically signifi-

Table 1 Clinical data of patients with large and small scar endometriomas

Clinical data	L-SE (13 cases with 13 nodules)	S-SE (17 cases with 20 nodules)	P
Mean age (yr) (range)	31.3 (22-39)	30.8 (20-42)	NS
No. of cesarean sections (range)	1.8 (1-3)	1.5 (1-3)	NS
Time since last cesarean section (mo)	66.0 ± 29.5	39.6 ± 18.0	< 0.01
Onset of symptoms (mo before admission)	43.0 ± 29.0	17.4 ± 20.0	< 0.01
Known pelvic endometriosis	2	1	NS
Previous pelvic/abdominal surgery	2	0	NS
Inconclusive previous diagnostic exams ¹	5	0	< 0.05
Continuous pain	4	2	NS
Cyclic pain	8	14	NS

¹Either computed tomography/magnetic resonance imaging/fine needle biopsy/laparoscopy. L-SE: Large scar endometrioma; S-SE: Small scar endometrioma; NS: Not significant.

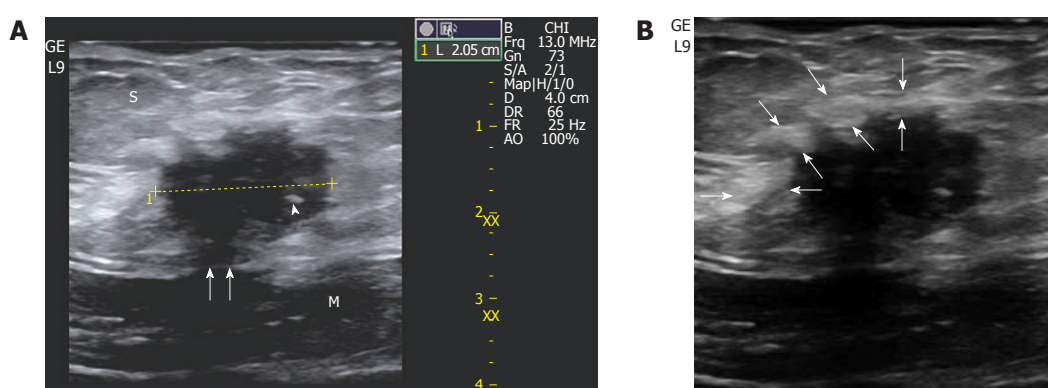


Figure 1 A 32-year-old woman with 6-mo of cyclic pain two years after a cesarean delivery. A: A small (2 cm) scar endometrioma is displayed at sonography located in the subcutaneous fat (S) with typical features: a roundish nodule, hypoechoic with fibrotic spots (the thick one is indicated by a white arrowhead), spiculated margins infiltrating the sheath (white arrows) of the rectus abdominis (M); B: An inflammatory hyperechoic ring (between white arrows) circumscribes almost the entire endometrioma.

cant higher percentage of patients with large endometriomas (38.4% *vs* 0%, $P < 0.05$) had undergone inconclusive diagnostic examinations elsewhere [CT (1 case), MRI (2 cases)/FNB (1 case)/laparoscopy (twice in 1 case)] that were aimed at clarifying the origin of lower abdominal pain.

Although not statistically significant, patients with larger endometriomas more often complained of continuous pain associated with a palpable mass (33.3%) than cases with small lesions (12.5%). In addition, surgical interventions for “bowel adhesions” that had not ameliorated patients’ symptoms were recorded in 2 cases (16.6%) with large implants. At the time of writing, no relapse of endometriosis was recorded in either group.

Sonography and color Doppler findings

The most frequent B-mode aspect of endometrioma was that of an inhomogeneously hypoechoic roundish nodule with fibrotic changes (in the form of hyperechoic spots or strands), a peripheral hyperechoic ring (complete or incomplete), spiculated margins, and a single vascular pedicle entering the mass at the periphery (Figures 1 and 2) with a mean RI of 0.78. This sonographic pattern was identified in 24 of 33 scar endometriomas (74%).

In the remaining 9 nodules (26%), all greater than 3 cm,

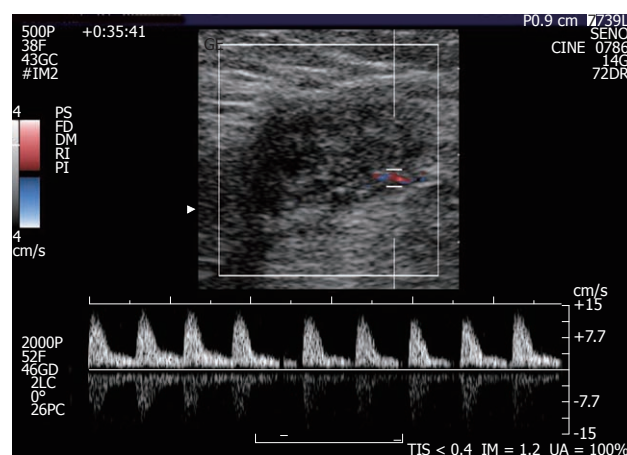


Figure 2 A small endometrioma with the typical single vascular pedicle entering the mass at the periphery. No central vascularisation is observed. Doppler demonstrates high resistance arterial flow (resistive index > 0.7).

a more elongated and irregular shape along with a more heterogenous echostructure and the presence of internal small cystic areas and/or fistulous tracts towards either the skin or the muscle (Figures 3 and 4) were observed. Multiple vascular pedicles associated with increased central vascularisation were also observed (Figure 5). In two

Table 2 Sonographic color Doppler findings in patients with large and small scar endometriomas

	L-SE (13 nodules)	S-SE (20 nodules)	P
US findings			
Size (mean \pm SD)	41.3 \pm 9.02	18.2 \pm 5.17	
Echotexture			
Hypoechoic with hyperechoic spots/strands	11	19	NS
Cystic portions and/or fistulous tract	7	1	< 0.02
Peripheral hyperechoic ring (absent/present)	1/12	7/13	NS
Margins (spiculated-infiltrating)	9	14	NS
Loss of oval or round shape	4	0	< 0.04
Color doppler findings			
Resistive index (mean \pm SD)	0.75 \pm 0.08	0.66 \pm 0.16	NS
Multiple vascular pedicles	8	2	< 0.04
Central vascularisation	8	2	<0.04

L-SE: Large scar endometrioma; S-SE: Small scar endometrioma; NS: Not significant.



Figure 3 A 30-year-old woman with a long history (84 mo) of continuous pain in the lower abdomen and two previous non-diagnostic laparoscopic examinations. In the abdominal wall (between the subcutaneous fat and the muscle), US exam discloses a 4-cm, ovoid hypoechoic endometrioma with a linear fistulous tract (arrow) emerging from the posterior aspect of the lesion and transgressing the muscular plane.

small endometriomas (7 and 14 mm) Doppler signals were not demonstrated.

To sum up, large endometriomas showed frequent cystic portions and fistulous tracts ($P < 0.02$), loss of round/oval shape ($P < 0.04$) along with increased vascularity ($P < 0.04$) (Table 2).

During the same time period, seven surgically-proved lesions near cesarean section scars were correctly identified as non-endometrioma nodules (1 metastasis, 2 incisional hernias, 1 abscess, 2 chronic inflammation, and 1 desmoid tumor).

DISCUSSION

Endometriosis of the abdominal wall arising on a Pfannenstiel incision represents an often neglected disease^[17] which is more prevalent than previously reported, especially if one considers the increasing cesarean section rate in Western countries^[18,19].

Sonographic and Doppler characteristics of scar endometrioma described in the literature^[14,20,21] are very different from the usual sonographic appearance of pelvic en-

dometriosis: classic-appearing adnexal endometriomas are cystic-like masses with round shape, regular margins, thick walls, and homogeneous low-level internal echoes^[13,22,23]. In contrast, scar endometriomas present as solid masses, inhomogeneously hypoechoic with a fibrotic component appearing as either tiny hyperechoic spots or thick hyperechoic strands and irregularly, often frankly spiculated margins; vascularity may be appreciated by Color Doppler in most of the masses, whereas cystic changes have been rarely reported^[14,20,21]. Moreover, in most cases perilesional hyperechoic rings (due to inflammatory reaction triggered by monthly haemorrhage in adjacent tissues) complete or incomplete may be appreciated^[14,21].

The present study confirmed the peculiar clinical and sonographic presentation of these lesions, but also demonstrated that large lesions (≥ 30 mm) displayed some clinical and sonographic characteristics which are different from the above-mentioned classic pattern.

Indeed, when compared to patients with smaller lesions, women with a large endometrioma showed a medical history characterized by a longer interval between both the last cesarean delivery and the onset of painful symptoms before hospital admission. Of note, they tended to complain of continuous pain instead of cyclic pain with menses and to more often undergo more expensive imaging examinations (CT/MRI) and invasive diagnostic (FNB/laparoscopy) and therapeutic (e.g., surgery for bowel adhesions) procedures without obtaining either a correct diagnosis or resolution of their illness.

In addition, implant size ≥ 30 mm was associated with peculiar sonographic features of endometriomas that showed more frequent small cystic areas, fistulous digitations and loss of the usual round/oval shape. Color Doppler examination showed multiple vascular pedicles entering the mass from different points and an abundant central vascularisation in contrast with the single vascular pedicle and scarce or absent intralesional vessels seen in smaller scar endometriomas. A likely explanation for these phenomena may rely on the longstanding cyclic bouts of haemorrhage facilitating both accumulation of larger fluid collections and loss of the initial nodular shape of the lesions due to inflammatory and fibrotic

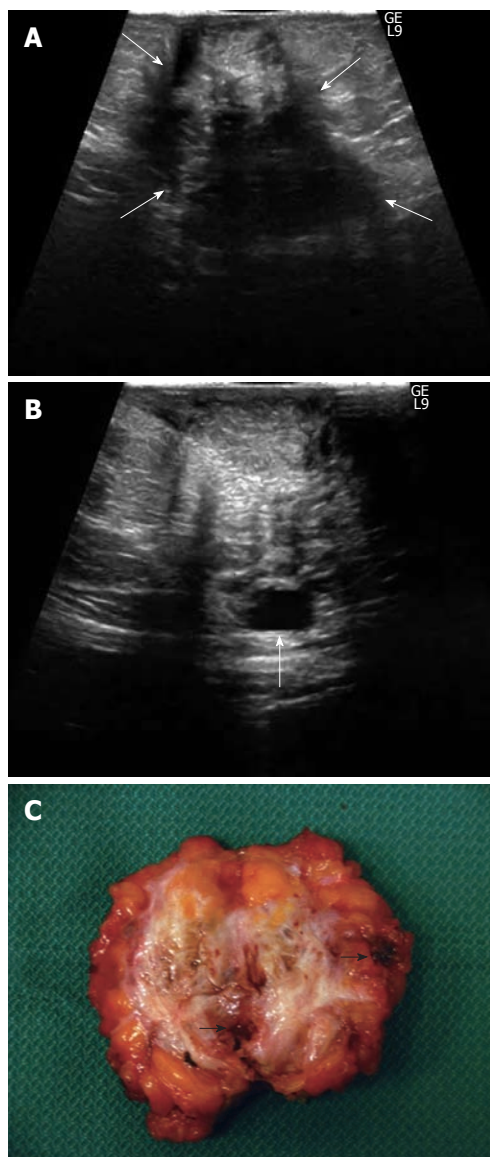


Figure 4 A 35-year-old woman with 52-mo of cyclic pain (after a cesarean delivery 2 years previously) that was not relieved by a surgical intervention for “intestinal adhesions” performed 44 mo before admission. A: US displays a huge (widest diameter: 60 mm), heterogeneous, irregularly-shaped mass occupying (between white arrows) the entire abdominal subcutaneous fat thickness and infiltrating the underlying muscle; B: A cystic area is seen along the posterior aspect of the mass (arrow); C: Cut surface of the surgical specimen: note the irregular shape of the highly vascularised mass with margins infiltrating adjacent tissues, the huge amount of white fibrotic strands and the multiple, well-defined haemorrhagic cystic collections (black arrows point out the greatest collections).

changes in the surrounding tissues triggered by haemorrhage itself.

The development of a fistulous tract may be regarded as a consequence of the infiltrative course of this chronic inflammatory process, a feature that further contributes to the irregular shape of endometriomas. An increase in vasculature density, which can be detected more easily on Color Doppler, is another obvious result of increasing nodule size over time.

If one considers that 43% of cases included in the present series had large endometriomas (≥ 3 cm) at the

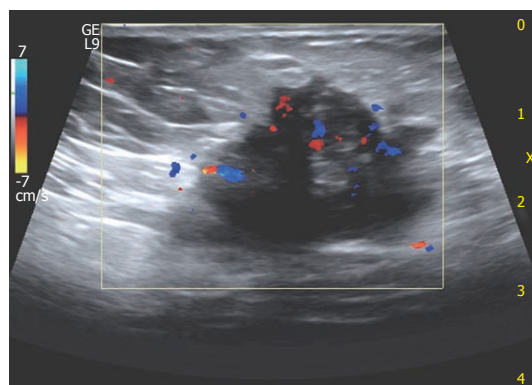


Figure 5 A 32-year-old woman with large scar endometrioma. Color Doppler exam displays multiple vascular poles entering the mass from different points and intralesional vascularisation.

time of diagnosis, this pathologic entity is a truly overlooked diagnosis with several consequences. Firstly, the masses in the abdominal wall are allowed to grow, a condition that brings about a change in the characteristics of both pain (from cyclic to continuous) and sonographic findings (more irregularly-shaped, heterogeneous lesions with cystic areas, fistulous tracts, and more abundant vascularisation). In turn, this entails widening of the differential diagnosis gamut between benign and malignant conditions, thus baffling physicians and radiologists further. Secondly, patients are bound to undergo more frequent inconclusive diagnostic work-ups with costly (i.e., CT/MRI) and sometimes invasive exams (i.e., FNB/laparoscopy). Thirdly, unnecessary abdominal surgery may be performed to relieve painful abdominal symptoms.

In addition, although the malignant transformation of abdominal wall endometrioma has not been clearly elucidated, owing to its rarity, such an eventuality should always be considered^[24,25]; therefore early detection and prompt treatment are mandatory.

Although scar endometrioma is a challenging diagnosis, only the first three cases in the present series were misdiagnosed (suture granulomas and sarcoma) at the beginning of this study. Since then every occupying-space lesion in the abdominal wall near a cesarean section incision in a patient with chronic abdominal pain (either cyclic or continuous) was considered a likely endometrioma, and all 27 subsequent patients were correctly diagnosed prior to operation. Moreover, seven non-endometrioma nodules near cesarean section scars were correctly identified during the same time period. Detailed clinical history and accurate physical and sonographic examination were the clues to the high diagnostic accuracy achieved; furthermore, none of the cases underwent CT, MRI and FNB in the diagnostic work-up and surgery, which is the sole form of effective therapy in abdominal wall endometriosis^[6,9,26], was not delayed. Although CT and MRI features of scar endometrioma have been described, they often provide only aspecific findings^[22,27,28]; furthermore, in the Author's opinion, evaluation of disease extent in musculo-cutaneous planes of the abdominal wall (one of the main alleged reasons to perform CT and/or MRI)

may be assessed nowadays by electronic wide-band high frequency sonographic probes as accurately as by CT and/or MRI. Some authors have proposed FNB to be a valuable diagnostic tool for scar endometrioma^[20,29,30], however, inconclusive data have also been obtained^[31]. This was true for one of the studied patients who underwent FNB with an inconclusive diagnosis several months before admission.

In conclusion, the clinical scenario (palpable mass near cesarean section scar and pain, especially if cyclic with menses) along with a careful sonographic examination of the entire abdominal wall of the lower quadrants, taking into account all the suggestive sonographic features, even if they might differ according to endometriotic implant size, are sufficient for a confident preoperative diagnosis of abdominal wall endometrioma.

COMMENTS

Background

Endometriotic implants in the abdominal wall near a cesarean section scar represent a rare but often misdiagnosed form of extrapelvic endometriosis.

Innovations and breakthroughs

The classic sonographic presentation of endometrioma (i.e., an inhomogeneously hypoechoic roundish nodule with fibrotic changes, a peripheral hyperechoic ring, spiculated margins and scarce internal vascularisation) may vary according to nodule size. In fact, large endometriomas show frequent cystic portions and fistulous tracts, loss of round/oval shape along with increased vascularity.

Peer review

The author reported the experience in 33 scar endometriomas by highlighting the clinical and sonographic characteristics of this neglected disease. The research is well written and clearly presented. It is a rare entity and of interest to radiologists.

REFERENCES

- Bergqvist A. Different types of extragenital endometriosis: a review. *Gynecol Endocrinol* 1993; **7**: 207-221
- Firilas A, Soi A, Max M. Abdominal incision endometriomas. *Am Surg* 1994; **60**: 259-261
- Singh KK, Lessells AM, Adam DJ, Jordan C, Miles WF, Macintyre IM, Greig JD. Presentation of endometriosis to general surgeons: a 10-year experience. *Br J Surg* 1995; **82**: 1349-1351
- Wicherek L, Klimek M, Skret-Magierlo J, Czekierdowski A, Banas T, Popiela TJ, Kraczkowski J, Sikora J, Oplawski M, Nowak A, Skret A, Basta A. The obstetrical history in patients with Pfannenstiel scar endometriomas--an analysis of 81 patients. *Gynecol Obstet Invest* 2007; **63**: 107-113
- Minaglia S, Mishell DR, Ballard CA. Incisional endometriomas after Cesarean section: a case series. *J Reprod Med* 2007; **52**: 630-634
- Ozel L, Sagiroglu J, Unal A, Unal E, Gunes P, Baskent E, Aka N, Titiz MI, Tufekci EC. Abdominal wall endometriosis in the cesarean section surgical scar: a potential diagnostic pitfall. *J Obstet Gynaecol Res* 2012; **38**: 526-530
- Olive DL, Schwartz LB. Endometriosis. *N Engl J Med* 1993; **328**: 1759-1769
- Steck WD, Helwig EB. Cutaneous endometriosis. *Clin Obstet Gynecol* 1966; **9**: 373-383
- Patterson GK, Winburn GB. Abdominal wall endometriomas: report of eight cases. *Am Surg* 1999; **65**: 36-39
- Kodandapani S, Pai MV, Mathew M. Umbilical laparoscopic scar endometriosis. *J Hum Reprod Sci* 2011; **4**: 150-152
- Kaunitz A, Di Sant'Agnese PA. Needle tract endometriosis: an unusual complication of amniocentesis. *Obstet Gynecol* 1979; **54**: 753-755
- Yackovich FH, Bender GN, Tsuchida AM. Case report: perianal episiotomy scar endometrioma imaged by CT and sector endoluminal ultrasound. *Clin Radiol* 1994; **49**: 578-579
- Woodward PJ, Sohaey R, Mezzetti TP. Endometriosis: radiologic-pathologic correlation. *Radiographics* 2001; **21**: 193-216; questionnaire 288-294
- Francica G, Giardiello C, Angelone G, Cristiano S, Finelli R, Tramontano G. Abdominal wall endometriomas near cesarean delivery scars: sonographic and color doppler findings in a series of 12 patients. *J Ultrasound Med* 2003; **22**: 1041-1047
- Blanco RG, Parithivel VS, Shah AK, Gumbs MA, Schein M, Gerst PH. Abdominal wall endometriomas. *Am J Surg* 2003; **185**: 596-598
- Park SB, Kim JK, Cho KS. Sonography of endometriosis in infrequent sites. *J Clin Ultrasound* 2008; **36**: 91-97
- Nirula R, Greaney GC. Incisional endometriosis: an underappreciated diagnosis in general surgery. *J Am Coll Surg* 2000; **190**: 404-407
- Black C, Kaye JA, Jick H. Cesarean delivery in the United Kingdom: time trends in the general practice research database. *Obstet Gynecol* 2005; **106**: 151-155
- Hamilton BE, Martin JA, Ventura SJ. Births: preliminary data for 2005. *Natl Vital Stat Rep* 2006; **55**: 1-18
- Hensen JH, Van Breda Vriesman AC, Puylaert JB. Abdominal wall endometriosis: clinical presentation and imaging features with emphasis on sonography. *AJR Am J Roentgenol* 2006; **186**: 616-620
- Savelli L, Manuzzi L, Donato ND, Salvi N, Trivella G, Cecaroni M, Seracchioli R. Endometriosis of the abdominal wall: ultrasonographic and doppler characteristics. *Ultrasound Obstet Gynecol* 2012; **39**: 336-340
- Kinkel K, Frei KA, Balleyguier C, Chapron C. Diagnosis of endometriosis with imaging: a review. *Eur Radiol* 2006; **16**: 285-298
- Asch E, Levine D. Variations in appearance of endometriomas. *J Ultrasound Med* 2007; **26**: 993-1002
- Bats AS, Zafrani Y, Pautier P, Duvillard P, Morice P. Malignant transformation of abdominal wall endometriosis to clear cell carcinoma: case report and review of the literature. *Fertil Steril* 2008; **90**: 1197.e13-1197.e16
- Yan Y, Li L, Guo J, Zheng Y, Liu Q. Malignant transformation of an endometriotic lesion derived from an abdominal wall scar. *Int J Gynaecol Obstet* 2011; **115**: 202-203
- Koger KE, Shatney CH, Hodge K, McClenathan JH. Surgical scar endometrioma. *Surg Gynecol Obstet* 1993; **177**: 243-246
- Amato M, Levitt R. Abdominal wall endometrioma: CT findings. *J Comput Assist Tomogr* 1984; **8**: 1213-1214
- Coley BD, Casola G. Incisional endometrioma involving the rectus abdominis muscle and subcutaneous tissues: CT appearance. *AJR Am J Roentgenol* 1993; **160**: 549-550
- Douglas C, Rotimi O. Extragenital endometriosis--a clinicopathological review of a Glasgow hospital experience with case illustrations. *J Obstet Gynaecol* 2004; **24**: 804-808
- Pathan ZA, Dinesh U, Rao R. Scar endometriosis. *J Cytol* 2010; **27**: 106-108
- Dwivedi AJ, Agrawal SN, Silva YJ. Abdominal wall endometriomas. *Dig Dis Sci* 2002; **47**: 456-461

S- Editor Cheng JX L- Editor Webster JR E- Editor Zheng XM



Chest radiographic and computed tomographic manifestations in allergic bronchopulmonary aspergillosis

Ritesh Agarwal, Ajmal Khan, Mandeep Garg, Ashutosh N Aggarwal, Dheeraj Gupta

Ritesh Agarwal, Ajmal Khan, Mandeep Garg, Ashutosh N Aggarwal, Dheeraj Gupta, Department of Pulmonary Medicine, Postgraduate Institute of Medical Education and Research, Chandigarh 160012, India

Mandeep Garg, Department of Radiodiagnosis, Postgraduate Institute of Medical Education and Research, Chandigarh 160012, India

Author contributions: Agarwal R conceived the article, performed the systematic review, drafted and revised the manuscript; Khan A, Garg M, Aggarwal AN and Gupta D drafted and revised the manuscript.

Correspondence to: Dr. Ritesh Agarwal, Associate Professor, Department of Pulmonary Medicine, Postgraduate Institute of Medical Education and Research, Sector-12, Chandigarh 160012, India. riteshpgi@gmail.com

Telephone: +91-172-2748215 Fax: +91-172-2756825

Received: November 18, 2011 Revised: February 21, 2012

Accepted: February 28, 2012

Published online: April 28, 2012

Abstract

AIM: To investigate the chest radiographic and high resolution computed tomography (HRCT) chest manifestations in glucocorticoid-naïve allergic bronchopulmonary aspergillosis (ABPA) patients.

METHODS: This is a prospective observational study and includes 60 consecutive glucocorticoid-naïve patients with ABPA who underwent chest radiography and HRCT of the chest (1.25 mm every 10 mm) in the routine diagnostic workup for ABPA.

RESULTS: Chest radiographs were normal in 50% of cases. Of the remainder, most patients demonstrated permanent findings in the form of parallel line and ring shadows suggesting bronchiectasis. Consolidation was detected in 17 cases but in the majority, the corresponding HRCT chest scan showed mucus-filled bronchiectatic cavities. Chest HRCT was normal in 22

patients, while central bronchiectasis (CB) was demonstrated in the remaining 38 patients. Bronchiectasis extended to the periphery in 33%-43% depending on the criteria used for defining CB. The other findings observed on HRCT were mucoid impaction, centrilobular nodules and high-attenuation mucus in decreasing order of frequency.

CONCLUSION: Patients with ABPA can present with normal HRCT chest scans. Central bronchiectasis cannot be considered a characteristic feature of ABPA as peripheral bronchiectasis is commonly observed. Consolidation is an uncommon finding in ABPA.

© 2012 Baishideng. All rights reserved.

Key words: Allergic bronchopulmonary aspergillosis; Chest radiograph; High resolution computed tomography; Computed tomography; *Aspergillus*

Peer reviewer: Francesco Lassandro, MD, Department of Radiology, Monaldi Hospital, via Leonardo Bianchi, 80129 Napoli, Italy

Agarwal R, Khan A, Garg M, Aggarwal AN, Gupta D. Chest radiographic and computed tomographic manifestations in allergic bronchopulmonary aspergillosis. *World J Radiol* 2012; 4(4): 141-150 Available from: URL: <http://www.wjgnet.com/1949-8470/full/v4/i4/141.htm> DOI: <http://dx.doi.org/10.4329/wjr.v4.i4.141>

INTRODUCTION

Allergic bronchopulmonary aspergillosis (ABPA) is a complex pulmonary disorder caused by immune reactions to antigens that are released by *Aspergillus fumigatus* (*A. fumigatus*), a ubiquitous fungus that colonizes the tracheo-bronchial tree of patients with asthma and cystic fibro-

sis^[1]. The disease can complicate the course in 2%-32% of asthmatics^[2], and 2%-15% of patients with cystic fibrosis^[3]. Patients most commonly present with poorly controlled asthma although hemoptysis, expectoration of mucus plugs, malaise and fever are also encountered^[4]. The diagnosis is made on a combination of clinical, immunological and radiological findings using the Rosenberg-Patterson criteria or a modification thereof^[5,6]. The natural history of ABPA is variable, and is characterized by recurrent remissions and relapses. In many patients it causes progression from mild asthma to glucocorticoid-dependent asthma, while in others, chronic lung damage in the form of central bronchiectasis (CB) or pulmonary fibrosis may ensue.

High resolution computed tomography (HRCT) of the chest is the radiological investigation of choice in patients with ABPA^[7]. Chest radiography is not sufficiently sensitive to detect the presence or the extent of bronchiectasis^[8]. Bronchography, traditionally considered the investigation of choice for the diagnosis of bronchiectasis, is not only invasive but may also be associated with adverse effects^[9]. HRCT of the chest safely allows detection of abnormalities not apparent on chest radiography with a sensitivity and specificity of 96%-98% and 93%-99% respectively, compared to bronchography in diagnosis of bronchiectasis^[10,11]. The chest radiographic findings depend on the clinical stage of the disease. Transient and fleeting opacities are characteristically found during acute exacerbations of the disease, whereas fixed abnormalities are encountered in later stages of the disease. The findings on HRCT chest scan include CB, mucus plugging with bronchocele formation, centrilobular nodules and others^[12].

Few studies have reported HRCT chest findings in patients with ABPA^[13-22]. Most of these studies have focused their attention on detection of CB rather than describing the CT findings. In fact, only two studies have described the occurrence of centrilobular nodules in ABPA^[20,22]. Moreover, with time, change in disease epidemiology and better understanding of the disease, the radiological manifestations may be different from those originally described. For example, high-attenuation mucus has been a recently described radiological finding in ABPA. In this study, we describe the chest radiographic and HRCT chest manifestations in glucocorticoid-naïve patients with ABPA diagnosed in the Chest Clinic of a tertiary care hospital in North India. Further, we have also performed a systematic review of all the studies describing the HRCT chest manifestations of ABPA.

MATERIALS AND METHODS

This is a prospective observational study, and includes consecutive glucocorticoid-naïve patients with ABPA diagnosed in the Chest Clinic of this institute over a period of 9 mo (January 2009 to September 2009). An informed consent was taken from all patients, and the study was

approved by the Local Ethics Committee. In our Chest Clinic, all patients with asthma are screened for *Aspergillus* sensitization using an intradermal skin test. Patients who demonstrate immediate cutaneous hyperreactivity to *Aspergillus* skin test are further evaluated with: IgE levels (total and *A. fumigatus*-specific), total eosinophil count, *Aspergillus* precipitins and HRCT of the chest. Patients are classified as having ABPA if they meet the following two criteria: (1) total IgE levels > 1000 IU/mL; and (2) *A. fumigatus*-specific IgE levels > 0.35 kUA/L; and two of the following criteria: (1) presence of serum precipitins against *A. fumigatus*; (2) radiographic pulmonary opacities (fixed/transient); (3) eosinophil count > 1000 cells/ μ L in peripheral blood; and (4) CB on HRCT chest^[6,22-24]. All the investigations, including CT scan, are done prior to starting glucocorticoid therapy.

Aspergillus skin test is performed by injecting the test forearm intradermally with 0.2 mL of the *Aspergillus* antigen (100 PNU/mL)^[25]. The reactions are classified as type I, if wheal and erythema occurs within a minute and resolves within 1 to 2 h. Any amount of subcutaneous edema after 6 h is classified as type III reaction.

Serum total IgE and *A. fumigatus*-specific IgE levels were assayed with commercially available kits using the quantitative enzyme-linked immunosorbent assay (Demeditec diagnostics GmbH, Kiel, Germany) and the fluorescent enzyme immunoassay (UniCap Systems; Pharmacia Upjohn; Stockholm, Sweden).

A. fumigatus precipitins were detected by the Ouchterlony's gel diffusion techniques as described by Longbottom and Pepys^[26].

The total leucocyte count was initially determined using an auto-analyzer (LH-750 or SF-3000). The percentage of differential leucocyte count was ascertained by counting and classifying 100 white blood cells on a peripheral blood smear. The total eosinophil count was obtained by multiplying the percentage with the total leucocyte count.

Spirometry was performed on a dry rolling seal spirometer (Spiroflow; PK Morgan Ltd.; Kent, UK) to determine the lung function measurements and bronchodilator reversibility. Age, gender, height and spirometry data were recorded for all patients using computer software previously developed by us^[27].

Chest radiography was performed in all patients. The radiographic findings were characterized as transient or fixed as described by McCarthy *et al.*^[28] with minor modifications. Transient opacities include consolidation, band-like shadows (toothpaste opacities, appearance of a "V", inverted "V" or a "Y" shaped shadow), finger-in-glove opacities (ovoid perihilar shadows with an expanded rounded distal end), circular shadows, and atelectasis. Fixed changes include parallel line or tram line shadows (width of the zone between the lines is more than that of a normal bronchus) and ring shadows.

HRCT of the chest was performed on a 16-row, multiple detector CT scanner (LightSpeed Plus; GE Medical

Table 1 Baseline characteristics of 60 patients with allergic bronchopulmonary aspergillosis *n* (%)

Demographic details	
Age (yr), median (IQR)	30 (21.3–43.5)
Sex (M:F)	34:26
History	
Duration of asthma (yr), median (IQR)	6.5 (3–10.75)
Hemoptysis	20 (33.3)
Expectoration of brownish-black mucus plugs	23 (38.3)
Prescription of anti-tuberculous therapy	17 (28.3)
Tobacco smoking	3 (5)
Spirometry	
Normal	14 (23.3)
Mild obstruction	15 (25)
Moderate obstruction	19 (31.7)
Severe obstruction	12 (20)
Bronchodilator reversibility	29 (48.3)
Immunological findings	
Aspergillus skin test	
Type 1	60 (100)
Type 3	47 (78.3)
Absolute eosinophil count (/μL), median (IQR)	800 (485–1535)
Aspergillus precipitins	50 (83.3)
IgE levels (total) (IU/mL), median (IQR)	6068.5 (3041–10284)
IgE levels (A _f) (kU/L), median (IQR)	6.5 (1.31–23.23)

Systems; Slough, UK) with a 512 matrix size. The scans [120 kilovolts; 10 mA; window width, 1500 Hounsfield units (HU); and window level, -600 HU] were obtained with a scan time of three seconds in the supine position at full end-inspiration from lung apex to base. The image acquisition was spaced and the images (1.25 mm at 10-mm intervals) were reconstructed using the high-spatial-frequency algorithm. The scans were analyzed at the lobar as well as segmental level. Individual bronchopulmonary segments were identified by their relationship to the major and minor fissures, and the appropriate lobar bronchi^[29]. The lobes were classified as three on the right and two on the left with lingular lobe considered as part of the left upper lobe. We divided the right lung into 10 segments, and left into 8 segments according to the classification of Jackson and Huber^[30]. All scans were assessed for radiological abnormalities and were categorized as follows: (1) normal bronchi were those having the lumen diameter similar to the adjacent artery. A bronchus was considered to be dilated if the broncho-arterial ratio (internal diameter of the bronchi divided by the external diameter of its accompanying artery) was more than one^[31]. Bronchiectasis was further classified as cylindrical, varicose or cystic. Cylindrical bronchiectasis, the mildest form of this disease, appears as tram track or signet ring depending on the orientation of bronchi relative to the scan plane. Varicose bronchiectasis was considered to be moderate dilatation of the bronchus with irregular bronchial walls showing a beaded appearance. Cystic bronchiectasis was defined as marked saccular dilatation, which appears as a cluster of air-filled cysts^[32]; (2) CB was defined using two different criteria, depend-

**Figure 1** Chest radiograph showing ring opacities (arrows) and parallel line shadows (arrowhead).

ing on whether the bronchiectasis was confined to the medial half (point midway between hilum and chest wall) or the medial two-thirds of the lung^[33]; (3) the presence of high attenuation mucus (HAM) was considered if the mucus was visually denser than the paraspinal skeletal muscle^[23,34,35]; (4) centrilobular nodules were considered to be present if the nodules were distributed primarily within the center of the secondary pulmonary lobule with or without a tree-in-bud pattern^[36]; (5) presence of parenchymal abnormalities including consolidation, parenchymal scarring, bullae, atelectasis and pneumothorax were also noted. The criteria used to define these appearances were as described by Webb *et al.*^[31]; and (6) patients were classified radiologically as ABPA-S, ABPA-CB and ABPA-CB-HAM based on the presence or absence of CB and HAM^[35].

RESULTS

During the study period, 60 patients [34 men, 26 women; median (IQR) age, 30 years (21.3–43.5)] were diagnosed with ABPA. The median duration of asthma prior to diagnosis of ABPA was 6.5 mo. The baseline demographic, clinical, spirometric, and immunological findings are shown in Table 1. Almost 29% of the patients had received anti-tuberculous therapy inappropriately prior to diagnosis of ABPA. Spirometry was normal in 23.3% and bronchodilator reversibility could be demonstrated in almost half of the patients.

Radiographic findings on the initial chest radiograph

The chest radiograph was normal in 50% of cases (Table 2). Of the remaining patients, the majority had permanent findings on the chest radiograph in the form of parallel line and ring shadows (Figure 1). Consolidation was detected in 17 (28.3%) cases. However, in 13 of them, the corresponding CT showed mucus-filled bronchiectatic cavities (Figure 2A and B), while classic consolidation was observed in both chest radiograph and chest CT in four patients (Figure 2C and D). Other findings observed were toothpaste opacities (Figure 4A), fleeting pulmonary

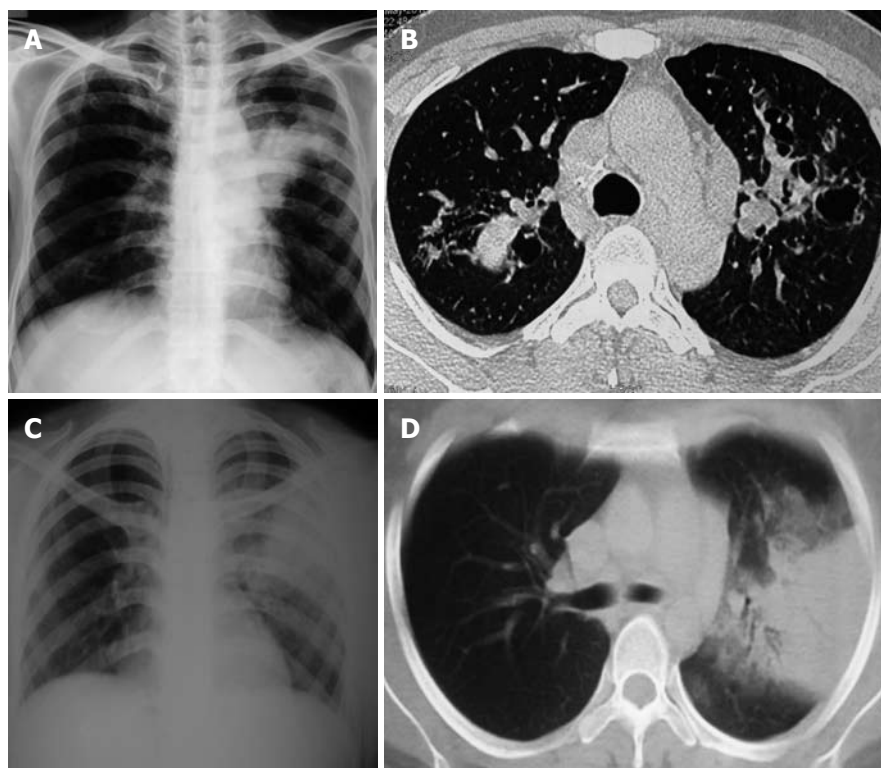


Figure 2 Chest radiograph. A, B: Chest radiograph (right panel) demonstrating consolidation in the left upper zone. Corresponding high resolution computed tomography of the chest (left panel) shows mucus-filled dilated bronchi; C, D: Chest radiograph (right panel) demonstrating consolidation in left upper zone. Computed tomography chest (left panel) shows typical consolidation with air bronchograms.

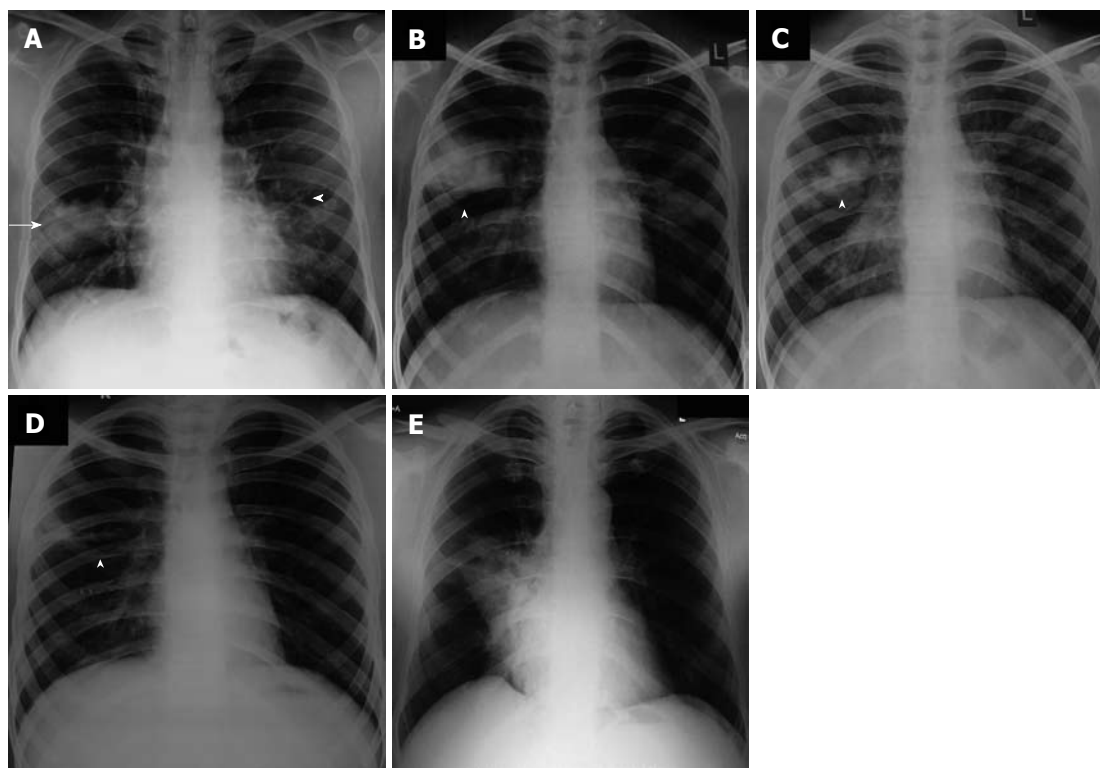


Figure 3 Chest radiograph. A: Chest radiograph showing consolidation (arrow) and tram track opacities (arrowhead); B-D: Chest radiographs performed over time in a patient with allergic bronchopulmonary aspergillosis showing fleeting pulmonary opacities, and clearance after treatment. Arrowheads depict the fleeting opacities; E: Chest radiograph showing subsegmental collapse.

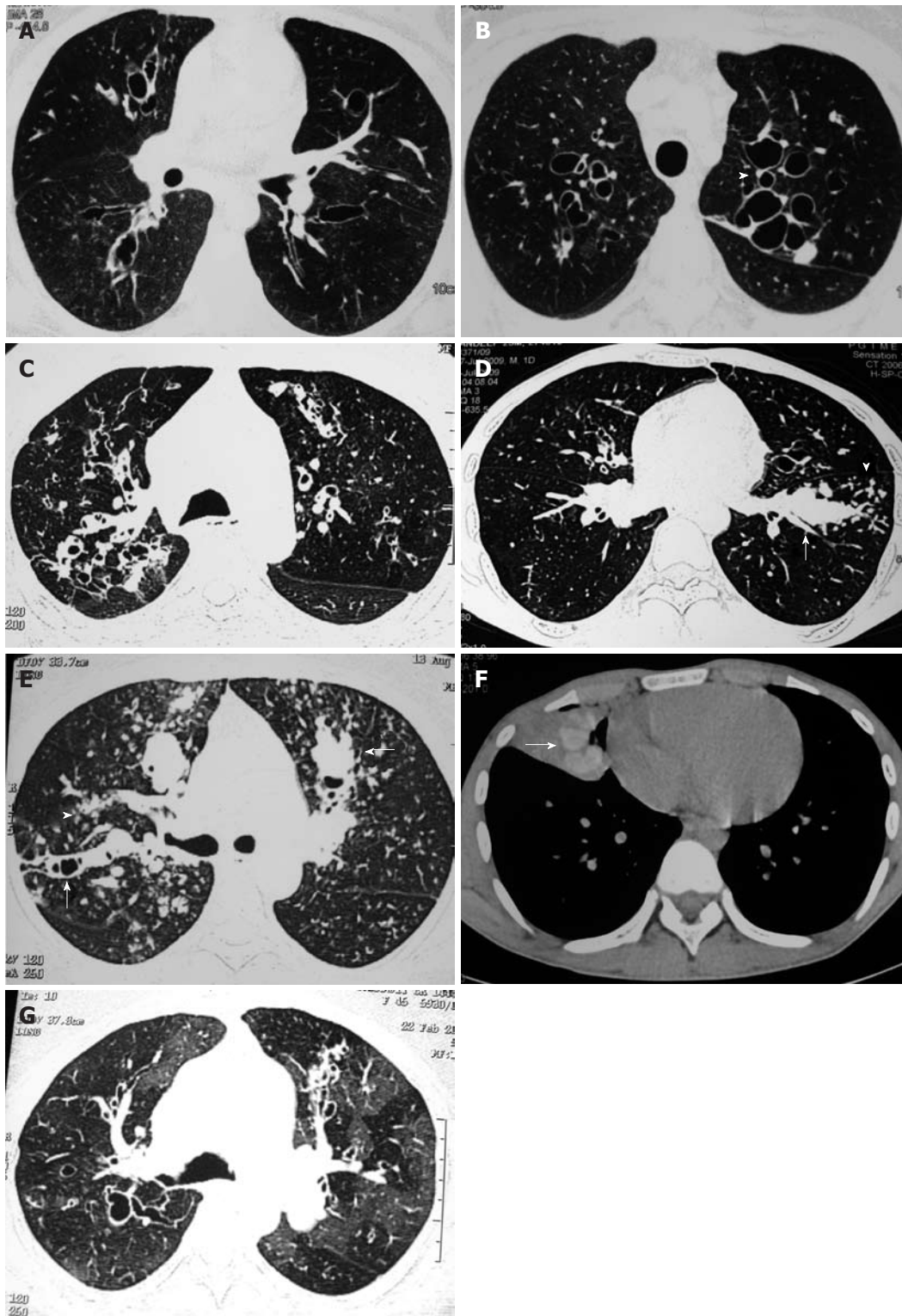


Figure 4 High resolution computed tomography chest scan. A, B: High resolution computed tomography chest scan showing typical central bronchiectasis. The upper panel shows cylindrical bronchiectasis while the lower panel shows cystic bronchiectasis; C: High resolution computed tomography chest scan showing bronchiectasis extending to the periphery. Also seen are mosaic attenuation and centrilobular nodules; D, E: High resolution computed tomography chest scan demonstrating mucus plugging of dilated bronchi (arrows) with evidence of centrilobular nodules in a tree-in-bud fashion (arrowheads); G: High resolution computed tomography chest scan showing central bronchiectasis with extensive areas of mosaic attenuation.

opacities (Figure 3B-D) and atelectasis (Figure 3E).

HRCT chest findings

HRCT of the chest was normal in 22 patients, while CB

was demonstrated in the remaining 38 patients (Figure 4A and B). Eight patients with normal chest radiographs were found to have CB on HRCT chest scan while all patients with abnormal chest radiographs had CB on chest CT.

Table 2 Radiographic findings in the first chest radiograph in 60 cases of allergic bronchopulmonary aspergillosis

Normal	30
Transient	
Fleeting opacities	24
Toothpaste/finger-in-glove opacities	23
Consolidation	17
Nodular	13
Atelectasis	8
Fixed	
Parallel line and ring shadows	25 ¹
Cystic bronchiectasis	10

¹Includes tramline shadows.

Bronchiectasis was generally extensive with the median number of lobes and segments involved being 4 and 7, respectively. The details of lobes and segments involved with regard to CB are shown in Table 3. Of the 300 lobes and 1080 segments, 22 patients (110 lobes, 396 segments) had normal HRCT, whereas 8 lobes and 20 segments could not be evaluated due to the presence of collapse or fibrosis. Of the remaining 182 lobes and 664 segments, 139 lobes and 282 segments were involved by CB. Cylindrical, varicose and cystic bronchiectasis was observed in 37, 73 and 29 lobes, respectively. While there was no predilection for any particular lobe or segment, the posterior segment of the right upper lobe had CB involvement in the bulk of cases. Three patients had isolated lower lobe bronchiectasis without involvement of the upper lobes. Bronchiectasis extended to the periphery (Figure 4C) in 33%-43% depending on the criteria used for defining CB (Table 3). Other findings noted in decreasing order of frequency were mucoid impaction, centrilobular nodules (Figure 4D and E), high-attenuation mucus (Figure 4F) and mosaic attenuation (Figure 4G).

DISCUSSION

ABPA was first described by Hinson *et al*^[37] in 1952 from the United Kingdom in a description of pyrexial illness occurring in asthmatics characterized by recurrent episodes of consolidation with peripheral blood eosinophilia. This was followed by reports of ABPA from other continents^[38-40]. The disease was initially considered to be rare until large series were published from different countries^[41,42]. In a genetically susceptible individual, inhaled conidia of *A. fumigatus* are able to germinate into hyphae, releasing antigens that not only compromise mucociliary clearance and breach the airway epithelial barrier, but also activate the immune system of the lung^[3]. This leads to influx of inflammatory cells with resultant tissue injury and the characteristic finding of CB. The finding of proximal bronchiectasis, i.e., involvement of segmental and subsegmental bronchi with sparing of the distal branches, is believed to be typical of ABPA^[43].

The current study represents one of the largest reporting radiological manifestations of ABPA. The importance

Table 3 High resolution computed tomography findings in 60 consecutive patients with allergic bronchopulmonary aspergillosis *n* (%)

	Results
Staging of ABPA	
ABPA-S	22 (36.7)
ABPA-CB	25 (41.7)
ABPA-CB-HAM	13 (21.7)
Lobar and segmental involvement by bronchiectasis (<i>n</i> = 38), median (IQR)	
Number of lobes	4 (3-5)
Number of segments	7 (4-9)
No. of lobes/segments not evaluable	8/20
No. of lobes/segments affected by central bronchiectasis	139/182
No. of lobes affected by peripheral bronchiectasis	
By 1/2 criteria	60/139 (43.2%)
By 2/3 criteria	46/139 (33.1%)
Right upper lobe	33/38
Apical segment	14
Anterior segment	19
Posterior segment	25
Right middle lobe	23/38
Medial segment	21
Lateral segment	13
Right lower lobe	27/38
Apical	20
Medial	10
Anterior	12
Lateral	15
Posterior	14
Left upper lobe	27/38
Apicoposterior	17
Anterior	17
Superior lingular	15
Inferior lingular	9
Left lower lobe	29/38
Apical	19
Anterior	12
Lateral	12
Posterior	18
Other findings	
Centrilobular nodules and tree-in-bud opacities	28 (46.7)
Atelectasis	8 (13.3)
Mucoid impaction	30 (50)
Mosaic attenuation	12 (20)
High-attenuation mucus	13 (21.7)
Lower lobe involvement without upper lobe involvement	3 (5)

ABPA: Allergic bronchopulmonary aspergillosis; CB: Central bronchiectasis; HAM: High attenuation mucus.

of chest radiographic findings is currently questionable with the advent of HRCT of the chest, and the radiographic manifestations seem to have lost their diagnostic importance. The most common chest radiographic finding noted in our study was a normal radiograph. Although transient findings were commonly observed in those with chest radiographic abnormality, most of the patients also had fixed abnormality indicating the presence of permanent lung damage. Consolidation, considered to be the most frequent chest radiographic abnormality of ABPA^[28], was evident on chest radiograph in our study. The HRCT chest scan, however, revealed

Table 4 Studies describing high resolution computed tomography findings in patients with allergic bronchopulmonary aspergillosis

Author (yr)	No. of patients	HRCT thickness	Scan time (s)	Window width/level	Lobes or segments evaluated	Central bronchiectasis criteria	Patients with CB	Patients with PB	Lobes with CB/PB	Lobes with PB
Currie <i>et al</i> ^[13] (1987)	9	3mm every 10 mm	5.5	Wide setting	NA	Subjective; based on proximity to hilum	9	7	31	19
Neeld <i>et al</i> ^[14] (1990)	8	1.5 mm every 10 or 20 mm		2000/-550	46 lobes	Medial 2/3rd of the lung	6	2	19	2
Shah <i>et al</i> ^[15] (1992)	2	NA	4.0	1000/-700	37 segments	Medial 2/3rd of the lung	24 segments	None		None
Angus <i>et al</i> ^[16] (1994)	14	3 mm every 9 mm	9.5	NA	102 lobes	Medial 2/3rd of the lung	14	1	43	5
Panchal <i>et al</i> ^[17] (1994)	21	8 mm contiguous sections	3-5	NA	336 segments	Medial 2/3rd of the lung	NA	NA	212 segments	NA
Sandhu <i>et al</i> ^[18] (1994)	15	8 mm contiguous scans (2-4 mm where required)	NA	1000/-700	90 lobes	Medial 2/3rd of the lung	44	NA	57	18
Panchal <i>et al</i> ^[19] (1997)	23	8 mm contiguous (4 mm if not clearly visualized)	3-5	NA	134 lobes/406 segments	Medial 2/3rd of the lung	23	NA	114 lobes/210 segments	34 lobes/45 segments
Ward <i>et al</i> ^[20] (1999)	44	1-3 mm every 10 mm at 5 selected levels	NA	NA	264	Medial 2/3rd of the lung	28	NA	184	NA
Mitchell <i>et al</i> ^[21] (2000)	19	1-1.5 mm every 10-20 mm; 5 and 10 mm contiguous cuts also taken	1-2	NA	114	Medial 2/3rd of the lung	18	15	101	NA
Agarwal <i>et al</i> ^[22] (2006)	126	1.25 mm every 10 mm	3.0	1500/-600	431 lobes/1621 segments	Medial half of the lung midway between the hilum and chest wall	NA	NA	255 lobes/664 segments	99 lobes

HRCT: High resolution computed tomography; CB: Central bronchiectasis.

the area of consolidation identified on the radiograph as mucus-filled bronchi in the majority of the patients, indicating that eosinophilic “pneumonia” is an uncommon finding of ABPA contrary to what has been previously believed. The likely reason is that previous studies describing chest radiographic findings in ABPA are of the pre-CT era and researchers could not corroborate their findings with HRCT of the chest.

Although CB is the most characteristic finding in ABPA, there is lack of uniformity in the definition of CB. Hansell *et al*^[33] were the first to describe CB arbitrarily as dilated bronchi within a point midway radially from the hilum to the chest wall. Subsequently, authors have used different definitions including subjective criteria based on proximity to the hilum^[13], and dilated bronchi within the medial two-thirds of the point radially from the hilum to the chest wall^[14,16,17]. Although believed to be a characteristic finding in ABPA, the significance of CB as a specific diagnostic marker for ABPA is debatable as it has been shown that almost 40% of the involved lobes have bronchiectasis extending to the periphery^[19,21,22]. In our study, the prevalence of CB was 43% and 33%, respectively, if CB was defined as the presence of bronchiectasis within the medial half or the medial two-thirds of the lung. Moreover, patients with asthma without ABPA can also

develop CB^[14,44]. Although bronchiectasis affecting three or more lobes, centrilobular nodules, and mucoid impaction on HRCT suggests ABPA rather than asthma^[20], one study recognized all these findings in asthmatics with *Aspergillus* sensitization without ABPA^[45]. Apart from CB, mucoid impaction was the commonest finding observed on HRCT in our study. The mucus plugs in ABPA are generally hypodense but can also be hyperdense; defined as a mucus plug visually denser than the paraspinal skeletal muscle^[22]. The hyperattenuating character of mucus is ascribed to the presence of calcium salts and metals or desiccated mucus^[46,47]. Recently, numerous reports have described the occurrence of HAM in ABPA^[23,34,48-51], and currently the presence of HAM is considered a pathognomonic finding in ABPA^[52].

To compare the HRCT chest findings of our study with those described in the literature, we have also performed a systematic review of PubMed and EmBase using free text search terms: allergic bronchopulmonary aspergillosis, ABPA. Our search yielded 3133 references of which 10 studies have reported HRCT chest findings of ABPA (Table 4)^[13-22]. The studies have used different protocols for performance of CT, and most studies have used the definition of CB as dilated bronchi present within the medial two-thirds of the lung fields. The presence

of bronchiectasis extending to the periphery has also been variably described^[13,14,16,18,19,22]. Most studies were retrospective and included patients who had already received glucocorticoids for treatment of ABPA^[13,14,16,19-21]. Only one study described the presence of HAM in ABPA^[22]. The presence of HAM in ABPA was first described by Goyal *et al.*^[53] although this radiological diagnosis was probably missed for long periods before^[54] and even after description of this finding^[18,55].

Although we have previously reported HRCT chest findings in ABPA^[22], the limitation of the previous study was that we had not compared the chest radiograph findings with chest CT. Moreover, in this study we have used different definitions for defining CB to determine the change in prevalence of peripheral bronchiectasis in ABPA with different definitions. The prevalence of peripheral bronchiectasis has been variably reported as between 11% and 61%. Our study is different from the previous studies in that we included consecutive glucocorticoid-naïve patients diagnosed in the Chest Clinic. This is also reflected by the fact that almost 37% of the patients had a normal HRCT of the chest. It is the usual belief of clinicians and radiologists that all patients with ABPA should manifest with CB on chest HRCT. However, the earliest stage of ABPA is serologic ABPA (ABPA-S) in which the patients fulfill all diagnostic criteria of ABPA but do not manifest with any abnormalities on HRCT chest scan^[56]. In fact, in asthma clinics where there is an active screening program for ABPA, almost 25% of ABPA patients will be diagnosed in the serological stage^[35].

In conclusion, HRCT findings are useful in the diagnosis of ABPA; however, patients with ABPA can present with normal HRCT of the chest. CB cannot be considered a characteristic feature as peripheral bronchiectasis is commonly observed. Consolidation is an uncommon finding of ABPA while high-attenuation mucus, if present, is a characteristic finding of ABPA.

COMMENTS

Background

Allergic bronchopulmonary aspergillosis (ABPA) is a complex pulmonary disorder caused by immune reactions to antigens that are released by *Aspergillus fumigatus*, a ubiquitous fungus that colonizes the tracheobronchial tree of patients with asthma and cystic fibrosis. High resolution computed tomography (HRCT) of the chest is the radiological investigation of choice in patients with ABPA. Few studies have reported HRCT chest findings in patients with ABPA.

Research frontiers

Most of the studies describing HRCT findings have focused their attention on detection of central bronchiectasis (CB) rather than describing the CT findings. In fact, only two studies have described the occurrence of centrilobular nodules in ABPA. Moreover, with time, change in disease epidemiology and better understanding of the disease, the radiological manifestations may be different from those originally described. For example, high-attenuation mucus has been a recently described radiological finding in ABPA. In this study, the author describes the chest radiographic and HRCT chest manifestations in glucocorticoid-naïve patients with ABPA diagnosed in the Chest Clinic of a tertiary care hospital in North India. Further, the authors also perform a systematic review of all the studies describing the HRCT chest manifestations of ABPA.

Innovations and breakthroughs

Chest radiographs were normal in 50% of cases while in the remaining, most patients demonstrated permanent findings in the form of parallel line and ring shadows suggesting bronchiectasis. Consolidation was detected in 17 cases but in the majority, the corresponding HRCT chest scan showed mucus-filled bronchiectatic cavities. Chest HRCT was normal in 22 patients, while CB was demonstrated in the remaining 38 patients. Bronchiectasis extended to the periphery in 33%-43% depending on the criteria used for defining CB. The other findings observed on HRCT were mucoid impaction, centrilobular nodules and high-attenuation mucus in decreasing order of frequency.

Applications

Patients with ABPA can present with normal HRCT of the chest. CB cannot be considered a characteristic feature of ABPA as peripheral bronchiectasis is commonly observed. Consolidation is an uncommon finding of ABPA

Terminology

CB: CB can be defined using two different criteria; if bronchiectasis is confined to the medial half (point midway between hilum and chest wall) or the medial two-thirds of the lung; High-attenuation mucus: considered if the mucus is visually denser than the paraspinal skeletal muscle.

Peer review

This is very interesting and well conducted study. It is worth of publication after some clarifications.

REFERENCES

- 1 Agarwal R. Allergic bronchopulmonary aspergillosis. In: Jindal SK, Shankar PS, Raoof S, Gupta D, Aggarwal AN, Agarwal R, editors. Textbook of pulmonary and critical care medicine. 1st ed. New Delhi: Jaypee Publications, 2010: 947-970
- 2 Agarwal R, Aggarwal AN, Gupta D, Jindal SK. Aspergillus hypersensitivity and allergic bronchopulmonary aspergillosis in patients with bronchial asthma: systematic review and meta-analysis. *Int J Tuberc Lung Dis* 2009; **13**: 936-944
- 3 Agarwal R. Allergic bronchopulmonary aspergillosis. *Chest* 2009; **135**: 805-826
- 4 Agarwal R, Chakrabarti A. Clinical manifestations and natural history of allergic bronchopulmonary aspergillosis. In: Pasqualotto AC, editor. Aspergillosis: From diagnosis to prevention. New York: Springer, 2010: 707-724
- 5 Rosenberg M, Patterson R, Mintzer R, Cooper BJ, Roberts M, Harris KE. Clinical and immunologic criteria for the diagnosis of allergic bronchopulmonary aspergillosis. *Ann Intern Med* 1977; **86**: 405-414
- 6 Agarwal R, Hazarika B, Gupta D, Aggarwal AN, Chakrabarti A, Jindal SK. Aspergillus hypersensitivity in patients with chronic obstructive pulmonary disease: COPD as a risk factor for ABPA? *Med Mycol* 2010; **48**: 988-994
- 7 Agarwal R, Khan A, Garg M, Aggarwal AN, Gupta D. Pictorial essay: Allergic bronchopulmonary aspergillosis. *Indian J Radiol Imaging* 2011; **21**: 242-252
- 8 Currie DC, Cooke JC, Morgan AD, Kerr IH, Delany D, Strickland B, Cole PJ. Interpretation of bronchograms and chest radiographs in patients with chronic sputum production. *Thorax* 1987; **42**: 278-284
- 9 Mendelson EB, Fisher MR, Mintzer RA, Halwig JM, Greenberger PA. Roentgenographic and clinical staging of allergic bronchopulmonary aspergillosis. *Chest* 1985; **87**: 334-339
- 10 Young K, Aspestrand F, Kolbenstvedt A. High resolution CT and bronchography in the assessment of bronchiectasis. *Acta Radiol* 1991; **32**: 439-441
- 11 Grenier P, Maurice F, Musset D, Menu Y, Nahum H. Bronchiectasis: assessment by thin-section CT. *Radiology* 1986; **161**: 95-99
- 12 Agarwal R. Allergic bronchopulmonary aspergillosis: Lessons for the busy radiologist. *World J Radiol* 2011; **3**: 178-181
- 13 Currie DC, Goldman JM, Cole PJ, Strickland B. Comparison

- of narrow section computed tomography and plain chest radiography in chronic allergic bronchopulmonary aspergillosis. *Clin Radiol* 1987; **38**: 593-596
- 14 **Neeld DA**, Goodman LR, Gurney JW, Greenberger PA, Fink JN. Computerized tomography in the evaluation of allergic bronchopulmonary aspergillosis. *Am Rev Respir Dis* 1990; **142**: 1200-1205
- 15 **Shah A**, Pant CS, Bhagat R, Panchal N. CT in childhood allergic bronchopulmonary aspergillosis. *Pediatr Radiol* 1992; **22**: 227-228
- 16 **Angus RM**, Davies ML, Cowan MD, McSharry C, Thomson NC. Computed tomographic scanning of the lung in patients with allergic bronchopulmonary aspergillosis and in asthmatic patients with a positive skin test to *Aspergillus fumigatus*. *Thorax* 1994; **49**: 586-589
- 17 **Panchal N**, Pant C, Bhagat R, Shah A. Central bronchiectasis in allergic bronchopulmonary aspergillosis: comparative evaluation of computed tomography of the thorax with bronchography. *Eur Respir J* 1994; **7**: 1290-1293
- 18 **Sandhu M**, Mukhopadhyay S, Sharma SK. Allergic bronchopulmonary aspergillosis: a comparative evaluation of computed tomography with plain chest radiography. *Australas Radiol* 1994; **38**: 288-293
- 19 **Panchal N**, Bhagat R, Pant C, Shah A. Allergic bronchopulmonary aspergillosis: the spectrum of computed tomography appearances. *Respir Med* 1997; **91**: 213-219
- 20 **Ward S**, Heyneman L, Lee MJ, Leung AN, Hansell DM, Müller NL. Accuracy of CT in the diagnosis of allergic bronchopulmonary aspergillosis in asthmatic patients. *AJR Am J Roentgenol* 1999; **173**: 937-942
- 21 **Mitchell TA**, Hamilos DL, Lynch DA, Newell JD. Distribution and severity of bronchiectasis in allergic bronchopulmonary aspergillosis (ABPA). *J Asthma* 2000; **37**: 65-72
- 22 **Agarwal R**, Gupta D, Aggarwal AN, Behera D, Jindal SK. Allergic bronchopulmonary aspergillosis: lessons from 126 patients attending a chest clinic in north India. *Chest* 2006; **130**: 442-448
- 23 **Agarwal R**, Gupta D, Aggarwal AN, Saxena AK, Chakrabarti A, Jindal SK. Clinical significance of hyperattenuating mucoid impaction in allergic bronchopulmonary aspergillosis: an analysis of 155 patients. *Chest* 2007; **132**: 1183-1190
- 24 **Agarwal R**, Gupta D, Aggarwal AN, Saxena AK, Saikia B, Chakrabarti A, Jindal SK. Clinical significance of decline in serum IgE levels in allergic bronchopulmonary aspergillosis. *Respir Med* 2010; **104**: 204-210
- 25 **Agarwal R**, Noel V, Aggarwal AN, Gupta D, Chakrabarti A. Clinical significance of *Aspergillus* sensitisation in bronchial asthma. *Mycoses* 2011; **54**: e531-e538
- 26 **Longbottom JL**, Pepys J. Pulmonary aspergillosis: diagnostic and immunological significance of antigens and C-substance in *aspergillus fumigatus*. *J Pathol Bacteriol* 1964; **88**: 141-151
- 27 **Aggarwal AN**, Gupta D, Jindal SK. Development of a simple computer program for spirometry interpretation. *J Assoc Physicians India* 2002; **50**: 567-570
- 28 **McCarthy DS**, Simon G, Hargreave FE. The radiological appearances in allergic broncho-pulmonary aspergillosis. *Clin Radiol* 1970; **21**: 366-375
- 29 **Osborne D**, Vock P, Godwin JD, Silverman PM. CT identification of bronchopulmonary segments: 50 normal subjects. *AJR Am J Roentgenol* 1984; **142**: 47-52
- 30 **Jackson CL**, Huber JF. Correlated applied anatomy of the bronchial tree and lungs with a system of nomenclature. *Chest* 1943; **9**: 319-326
- 31 High-resolution computed tomography findings of lung disease. In: Webb WR, Muller NL, Naidich DP, editors. High-resolution CT of the lung. 4th ed. Philadelphia: Lippincott Williams and Wilkins, 2009: 65-176
- 32 **Naidich DP**, McCauley DI, Khouri NF, Stitik FP, Siegelman SS. Computed tomography of bronchiectasis. *J Comput Assist Tomogr* 1982; **6**: 437-444
- 33 **Hansell DM**, Strickland B. High-resolution computed tomography in pulmonary cystic fibrosis. *Br J Radiol* 1989; **62**: 1-5
- 34 **Agarwal R**, Aggarwal AN, Gupta D. High-attenuation mucus in allergic bronchopulmonary aspergillosis: another cause of diffuse high-attenuation pulmonary abnormality. *AJR Am J Roentgenol* 2006; **186**: 904
- 35 **Agarwal R**, Khan A, Gupta D, Aggarwal AN, Saxena AK, Chakrabarti A. An alternate method of classifying allergic bronchopulmonary aspergillosis based on high-attenuation mucus. *PLoS One* 2010; **5**: e15346
- 36 **Gotway MB**, Reddy GP, Webb WR, Elicker BM, Leung JW. High-resolution CT of the lung: patterns of disease and differential diagnoses. *Radiol Clin North Am* 2005; **43**: 513-42, viii
- 37 **HINSON KF**, MOON AJ, PLUMMER NS. Broncho-pulmonary aspergillosis; a review and a report of eight new cases. *Thorax* 1952; **7**: 317-333
- 38 **Elder JL**, Smyth JT. Allergic broncho-pulmonary aspergillosis. *Med J Aust* 1967; **1**: 231-233
- 39 **Patterson R**, Golbert TM. Hypersensitivity disease of the lung. *Univ Mich Med Cent J* 1968; **34**: 8-11
- 40 **Shah JR**. Allergic pulmonary aspergillosis. *J Assoc Physicians India* 1971; **19**: 835-841
- 41 **Hoehne J**, Reed C, Dickie H. Allergic bronchopulmonary aspergillosis is not rare. *J Lab Clin Med* 1971; **78**: 1007-1008
- 42 **Chetty A**, Bhargava S, Jain RK. Allergic bronchopulmonary aspergillosis in Indian children with bronchial asthma. *Ann Allergy* 1985; **54**: 46-49
- 43 **Chan-Yeung M**, Chase WH, Trapp W, Grzybowski S. Allergic bronchopulmonary aspergillosis. Clinical and pathologic study of three cases. *Chest* 1971; **59**: 33-39
- 44 **Paganin F**, Trussard V, Seneterre E, Chanez P, Giron J, Godard P, Sénac JP, Michel FB, Bousquet J. Chest radiography and high resolution computed tomography of the lungs in asthma. *Am Rev Respir Dis* 1992; **146**: 1084-1087
- 45 **Menzies D**, Holmes L, McCumesky G, Prys-Picard C, Niven R. *Aspergillus* sensitization is associated with airflow limitation and bronchiectasis in severe asthma. *Allergy* 2011; **66**: 679-685
- 46 **Kopp W**, Fotter R, Steiner H, Beaufort F, Stammberger H. Aspergillosis of the paranasal sinuses. *Radiology* 1985; **156**: 715-716
- 47 **Dillon WP**, Som PM, Fullerton GD. Hypointense MR signal in chronically inspissated sinonasal secretions. *Radiology* 1990; **174**: 73-78
- 48 **Logan PM**, Müller NL. High-attenuation mucous plugging in allergic bronchopulmonary aspergillosis. *Can Assoc Radiol J* 1996; **47**: 374-377
- 49 **Karunaratne N**, Baraket M, Lim S, Ridley L. Case quiz. Thoracic CT illustrating hyperdense bronchial mucous plugging: allergic bronchopulmonary aspergillosis. *Australas Radiol* 2003; **47**: 336-338
- 50 **Molinari M**, Ruii A, Biondi M, Zompatori M. Hyperdense mucoid impaction in allergic bronchopulmonary aspergillosis: CT appearance. *Monaldi Arch Chest Dis* 2004; **61**: 62-64
- 51 **Morozov A**, Applegate KE, Brown S, Howenstone M. High-attenuation mucus plugs on MDCT in a child with cystic fibrosis: potential cause and differential diagnosis. *Pediatr Radiol* 2007; **37**: 592-595
- 52 Airway diseases. In: Webb WR, Muller NL, Naidich DP, editors. High-resolution CT of the lung. 4th ed. Philadelphia: Lippincott Williams and Wilkins, 2009: 492-554
- 53 **Goyal R**, White CS, Templeton PA, Britt EJ, Rubin LJ. High attenuation mucous plugs in allergic bronchopulmonary aspergillosis: CT appearance. *J Comput Assist Tomogr* 1992; **16**: 649-650
- 54 Mycotic and Actinomycotic pleuropulmonary infections. In: Fraser RG, Pare JAP, Pare PD, Fraser RS, Genereux GP, editors. Diagnosis of diseases of the chest. 3rd ed. Philadelphia:

- WB Saunders, 1989: 940-1022
- 55 **Aquino SL**, Kee ST, Warnock ML, Gamsu G. Pulmonary aspergillosis: imaging findings with pathologic correlation. *AJR Am J Roentgenol* 1994; **163**: 811-815
- 56 **Agarwal R**, Khan A, Aggarwal AN, Saikia B, Gupta D, Chakrabarti A. Role of inhaled corticosteroids in the management of serological allergic bronchopulmonary aspergillosis (ABPA). *Intern Med* 2011; **50**: 855-860

S- Editor Cheng JX **L- Editor** Logan S **E- Editor** Zheng XM

Primary malignant fibrous histiocytoma of the abdominal cavity: CT findings and pathological correlation

Bivek Karki, Yi-Kai Xu, Yuan-Kui Wu, Wei-Wei Zhang

Bivek Karki, Yi-Kai Xu, Yuan-Kui Wu, Wei-Wei Zhang, Department of Medical Imaging, Nan fang Hospital, Southern Medical University, Guangzhou 510515, Guangdong Province, China
 Author contributions: Karki B was involved in the study concept, writing, literature review and drafting; Xu YK was responsible for the concept, literature review and writing guidance; Wu YK and Zhang WW contributed to the collection of articles, CT images and final editing.

Correspondence to: Yi-Kai Xu, MD, PhD, Professor and Head, Department of Medical Imaging, Nan fang Hospital, Southern Medical University, Guangzhou 510515, Guangdong Province, China. daoshi08@gmail.com

Telephone: +86-20-61687333 Fax: +86-20-61687333

Received: September 25, 2011 Revised: February 27, 2012

Accepted: March 5, 2012

Published online: April 28, 2012

Abstract

AIM: To study computed tomography (CT) features of abdominal malignant fibrous histiocytoma (MFH) in various rare locations.

METHODS: We retrospectively identified cases of MFH involving the abdominal cavity. Particular attention was paid to details regarding imaging features and histological types.

RESULTS: The study population consisted of seven men and one woman, with a mean age of 52.5 years. Seven patients had some physical symptoms, while one was incidentally detected. The sites of origin were liver ($n = 3$), greater omentum ($n = 1$), superior mesentery ($n = 1$), ileum ($n = 1$), right psoas muscle ($n = 1$) and right kidney ($n = 1$). With the exception of the ileum lesion, all were of huge size. The contour of the lesions was more or less clear. Foci of necrosis were present in six lesions ($n = 6$). On plain CT scan, all lesions were hypo to iso dense. The lesion in the greater omentum was cystic. One lesion ($n = 1$) showed significant enhancement and the cystic lesion showed mild peripheral

enhancement. An abundance of blood vessels surrounding the mass was seen in two lesions ($n = 2$) and both were of the inflammatory variety. Pathological examination revealed storiform-pleomorphic variety ($n = 4$), inflammatory variety ($n = 3$) and myxoid variety ($n = 1$). Two of the patients with inflammatory MFH had a clinical presentation of fever and one was afebrile, however, blood investigations in all three showed leukocytosis.

CONCLUSION: Primary MFHs of the abdominal viscera and gastrointestinal tract are generally huge soft tissue masses containing areas of low attenuation and mild to moderate contrast enhancement.

© 2012 Baishideng. All rights reserved.

Key words: Abdomen; Computed tomography; Malignant fibrous histiocytoma; Soft tissue sarcoma

Peer reviewers: Vlastimil Valek, Professor, MD, CSc, MBA, Department of Radiology, University Hospital Brno and Med. Faculty Masaryk University Brno, Brno 62800, Czech Republic; Hiroshi Yoshida, Department of Surgery, Nippon Medical School Tama Nagayama Hospital, Tokyo 205-8512, Japan

Karki B, Xu YK, Wu YK, Zhang WW. Primary malignant fibrous histiocytoma of the abdominal cavity: CT findings and pathological correlation. *World J Radiol* 2012; 4(4): 151-158 Available from: URL: <http://www.wjgnet.com/1949-8470/full/v4/i4/151.htm> DOI: <http://dx.doi.org/10.4329/wjr.v4.i4.151>

INTRODUCTION

Malignant fibrous histiocytoma (MFH) is a pleomorphic sarcoma. It was first described as malignant histiocytoma and fibrous xanthoma by Ozello *et al* in 1963^[1], and was established by O'Brien and Stout as a soft tissue sarcoma arising from fibroblasts and histiocytes in 1964^[1,2]. MFH is a relatively rare tumor that occurs throughout the body^[3]. However, it is also the most common sarcoma

appearing in late adult life (6th-7th decades) and men are more often affected than women. The most frequent site of MFH is the extremities (lower extremity 49%, upper extremity 19%). The second most prevalent site is the retroperitoneum (16%) and peritoneal cavity (5%-10%)^[4]. Occurrence of this lesion in visceral organs and the gastrointestinal tract is very rare, and there is a marked paucity of reports describing MFH in these locations. Our purpose was to study the computed tomography (CT) features of abdominal MFH in various rare locations.

MATERIALS AND METHODS

Subjects

Cases of MFH of the abdominal cavity registered in the pathological department of our institution from 2000 to 2010 were identified. The search yielded 9 cases, the reports of which were reviewed. One was excluded due to unavailability of clinical data. For the remaining 8 cases, complete hospital records (history, diagnostic imaging, operative findings and pathological reports) were reviewed. Particular attention was paid to details regarding imaging features and histological types. Clinical data were reviewed for age, sex, and presenting complaints. Ethical approval from the institutional review board at our hospital was obtained to conduct this study.

CT scanning and image analysis

CT data were available on PACS (picture archiving and communication system, Marotech) of all patients which were studied by two radiologists. All CT examinations were performed using a 16 slice CT scanner (Light speed, GE Health Care, USA). Scans were obtained with a tube voltage of 120 kV, tube current of 280-320 mAs, slice thickness 5 mm and section interval of 5 mm. With the exception of the patient with the ileum mass, all underwent a contrast scan. For the contrast-enhanced scan, 80-120 mL of non-ionic contrast agent (Ultravist) was injected at the rate of 3.5-4 mL/s. All images were reviewed on a PACS monitor and were retrospectively analyzed with regard to the location of the lesions, tumor morphology and enhancement pattern.

Pathologic analysis

With the exception of the patient with a mesenteric lesion who only underwent CT-guided biopsy, the other patients were treated surgically. Each specimen was examined microscopically and immunohistochemically to confirm the diagnosis. The pathology records of each patient were reviewed to establish the histological subtypes of the lesions.

RESULTS

The study population consisted of seven men and one woman, who had an age range of 23-79 years (mean 52.5 years). Seven patients had some physical symptoms, while one was incidentally detected during a regular

health check-up. The sites of origin were liver ($n = 3$), greater omentum ($n = 1$), superior mesentery ($n = 1$), ileum ($n = 1$), right psoas muscle ($n = 1$) and right kidney ($n = 1$) (Table 1). With the exception of the ileum lesion, all were of huge size. The contours of the lesions were more or less clear, except one, in the left lobe of the liver. Foci of necrosis were present in six lesions ($n = 6$). On plain CT scan, all lesions were hypo to iso dense, seven lesions were soft tissue masses of density ranging from 30-47 HU in the plain scan. The lesion in the greater omentum was cystic with a density of 15-23 HU. Contrast scans showed significant enhancement in one lesion ($n = 1$) and the cystic lesion showed mild peripheral enhancement. The central necrotic zone in the mesenteric lesion was more evident in the contrast scan. An abundance of blood vessels surrounding the mass was seen in two lesions ($n = 2$), both of which were the inflammatory variety. The lesion in the ileum had peritoneal metastasis at the time of diagnosis. The greater omentum lesion recurred within 3 mo of surgery. The patient with the mesentery lesion could not undergo surgery due to multiple distant metastatic foci. Pathological examination revealed storiform-pleomorphic variety ($n = 4$), inflammatory variety ($n = 3$) and myxoid variety ($n = 1$). Two patients with inflammatory MFH had a clinical presentation of fever and one was afebrile, however, blood investigations in all three showed leukocytosis.

DISCUSSION

MFH is a well-established sarcoma arising in the adult population. It is considered to arise from primitive mesenchymal cells and can occur in any part of the body. Despite this ubiquity, involvement of the visceral organs and peritoneal cavity is uncommon. The cause of its origin is not clear. However, it has been recognized as a complication resulting from radiation, chronic postoperative repair, trauma, surgical incisions or burn scars^[1], but this would explain only a minority of cases. Sun exposure does not seem to be an important risk factor^[5]. MFH mainly involves extremities followed by the retroperitoneum. Uncommon locations include the head and neck region, dura mater, brain, lung, heart, aorta, pancreas, liver, spleen, breast, intestine and mesentery^[6-10].

MFH pathological and clinical features

MFH is composed of both histiocytic and fibrous elements, according to their content and arrangement, MFH was divided into five major groups by Enzinger *et al.*^[11]: storiform-pleomorphic, myxoid, giant cells, inflammatory and angiomatoid. The first two types, namely storiform-pleomorphic and myxoid types are usually high grade, whereas the others tend to be lower grade^[1]. Of these types, the storiform-pleomorphic type is most common, accounting for two thirds of cases. It is composed of spindle-shaped cells arranged in short fascicles in a cartwheel or storiform pattern, along with plump histiocytic cells showing mitotic features^[4]. The myxoid subtype is the second

Table 1 Clinical, computed tomography and pathological findings of cases

S. No.	Age (yr)/sex	Clinical presentations	Location	Size (cm)	Necrosis	CT		Histological subtypes
						Plain	Contrast	
1	31/F	Fever, abdominal pain	Liver lt. lobe	9.7 × 5.8 × 3.6	-	Hypodense	Significant	Inflammatory
2	47/M	Upper abdominal pain	Liver rt. lobe	7.9 × 8.8 × 3.3	+	Hypodense	Mild	Storiform-pleomorphic
3	54/M	Jaundice, upper abdominal pain	Liver lt. lobe	7.5 × 6.2 × 1.2	+	Hypodense	Mild	Myxoid
4	34/M	Fever, polyuria	Greater omentum	12.0 × 11.0 × 22.6	+	Hypodense	Mild peripheral	Inflammatory
5	64/M	Abdominal pain, weight loss	Mesentery	6.3 × 4.1 × 2.4	+	Hypodense	Mild in equilibrium phase	Inflammatory
6	79/M	Abdominal discomfort	Ileum	3.3 × 2.3 × 5.0	-	Hypodense	-	Storiform-pleomorphic
7	59/M	Occasional Lower abdominal pain	Retroperitoneal - psoas muscle	9.4 × 7.7 × 10.0	+	Isodense	Mild	Storiform-pleomorphic
8	23/M	Health check up	Rt. Kidney	7.0 × 6.4 × 1.8	+	Hypodense	Mild in equilibrium phase	Storiform-pleomorphic

CT: Computed tomography; +: Present; -: Absent.



Figure 1 A 31-year-old female with liver malignant fibrous histiocytoma. A: Plain computed tomography scan shows well demarcated mass with direct contact to the left lobe of liver and uniform density of 38 HU; B: Contrast scan arterial phase shows heterogeneous enhancement of mass compare to normal liver parenchyma with surrounding blood vessels; C: Pathological specimen HE (× 400) showing multinucleated spindle shape tumor cells with inflammatory cells.

most common variant, with definite metastatic potential, but a relatively indolent natural history compared with the storiform-pleomorphic variant^[12]. The inflammatory MFH was first described by Kyriakos *et al*^[13] in 1976. Unlike other types of MFHs, inflammatory MFH is more likely to develop in the retroperitoneum than in extremities^[14]. Although the mechanism is poorly understood, patients often present with striking features of infection such as fever and pathologically acute inflammatory infiltration mainly by neutrophils, together with a small number of other types of inflammatory cells^[15]. On immunohistochemistry examination, MFH frequently expresses a positive reaction to vimentin, actin, CD-68, and α 1-antitrypsin^[1,16].

Liver MFH

Liver is an exceptional site of involvement. Since the first report in 1985, only about 30 cases of hepatic MFH have been reported in the English literature^[17,20]. There is no predilection for lobe or the site of origin. The prognosis is poor, with the overall 2-year survival rate approximately 60%^[18]. Unenhanced CT findings of hepatic MFH include poorly demarcated or a well circumscribed, large or multinodular mass showing heterogeneous low attenuation density, with frequent areas of necrosis and occasional intratumoral calcification^[19,22]. Smaller tumors may show a solid mass without prominent internal necro-

sis^[21]. Following contrast injection, heterogeneous mild to moderate enhancement of the mass with several necrotic areas may be evident, and rarely enhancing peripheral pseudo-capsule or significant enhancement is noted^[17]. Although the vascularity of MFH is variable, the majority of lesions are moderately hypervascular with the tumor supply derived from multiple surrounding vessels^[23].

One of three patients with inflammatory MFH in our study showed marked enhancement and abundant blood vessels surrounding the tumor mass (Figure 1), and in the other two cases the enhancement was mild (Figure 2). The patient with a mass in the left liver lobe showed a poorly demarcated tumor margin (Figure 3), while the other two had well demarcated margins. The tumors may involve the liver capsule and adjacent organs, but there is no evidence of portal vein invasion, bile duct obstruction, or regional lymph node metastasis^[17,21]. A report of a mass undergoing complete necrosis and significant intratumoral hemorrhage involving the hemoperitoneum has also been published^[23]. The differential diagnosis of liver MFH includes hepatocellular carcinoma and other sarcomas such as leiomyosarcoma, fibrosarcoma and angiosarcoma.

Greater omentum MFH

Despite the ubiquity of MFHs, involvement of the omentum is uncommon. Involvement of the peritoneal



Figure 2 A 47-year-old male with liver malignant fibrous histiocytoma. Contrast-enhanced computed tomography scan arterial phase shows a mass with a clear boundary in the right-posterior lobe of liver segment 6 and 7. No obvious enhancement with areas of hypodensity is evident.

cavity is seen in 5%-10% of MFHs^[4,24]. During a MEDLINE search we found only 5 cases of MFH in the English literature with specific occurrence in the omentum including ours. On CT, MFH has a density predominantly equivalent to muscle^[2,6]. Hypodense areas represent necrosis which frequently exist within the lesions and these are more apparent on post-contrast study. It is difficult to determine the true origin of omentum MFH because the tumor is usually huge. A few authors have even described the mass undergoing complete necrosis and resembling a cyst or abscess in the imaging study^[6,20]. Approximately 5% of MFHs may eventually develop spontaneous intratumoral hemorrhage, especially when the MFH arises from the peritoneum or omentum. The intratumoral hemorrhage can be so extensive as to obscure the underlying neoplasm and could create a large cyst-like space that might be mistaken for a hematoma, abscess or cystic tumor^[23]. Similarly, in our case, the mass was completely cystic with a density of 15 to 23 HU extending to the pelvic cavity and it was very difficult to determine its site of origin, which corresponded to the findings of Huang *et al.*^[6]. Therefore, the preoperative diagnosis was difficult (Figure 4). However, due to the size and presence of abundant blood vessels surrounding the mass, a malignant lesion was suspected. The patient underwent preoperative embolization of the feeding vessels to minimize the risk of bleeding. Intra-operative findings revealed a greater omentum cystic mass with adherence to the small bowel and sigmoid colon. The pathological diagnosis revealed the inflammatory variety of MFH. The tumor recurred during the subsequent 3-mo follow-up, which was inconsistent with the previous report commenting on the inflammatory variety which had a low rate of recurrence and metastasis^[2]. Differential diagnosis in cystic omental MFH includes gastrointestinal stromal tumors, cystic mesothelioma, lymphangioma, hematoma and abscess.

Superior mesentery MFH

MFH of the mesentery is an extremely rare and highly malignant neoplasm with early metastatic spread. There are only a few reported cases of MFH of the superior

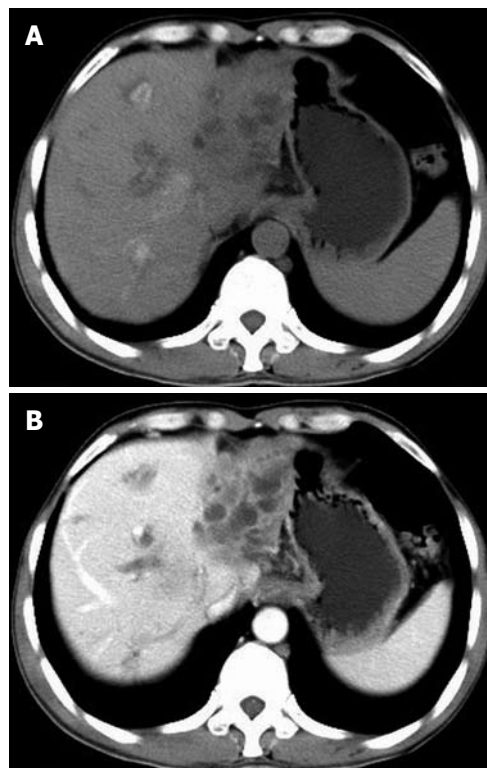


Figure 3 A 54-year-old male with liver malignant fibrous histiocytoma. A: Non-contrast computed tomography shows ill defined lesion of density 30 HU in the left lobe with dilated intrahepatic biliary duct; B: Contrast scan portal vein phase shows low enhancement compared to normal liver parenchyma and multiple areas of low attenuation.

mesentery. During a MEDLINE search we found only 14 reported cases in the English literature including ours. On CT, MFH typically presents as a poorly margined or well circumscribed soft tissue mass, with hypodense areas due to necrosis^[9,25]. Eccentrically located lumpy and ring-like calcifications due to osteoid and chondroid metaplasia have been reported on CT in 16% of abdominal MFHs^[6]. As in our patient, the mass was of soft tissue density with central necrotic areas which were more evident on the contrast scan. CT-guided biopsy was performed, and pathological findings revealed tissue composed of fibroblastic and histiocytic elements with marked inflammatory cell infiltrates. The area of low attenuation corresponded to necrosis and cystic degeneration (Figure 5). The diagnosis of mesenteric MFH must be differentiated from gastrointestinal stromal tumors which account for most primary mesenchymal tumors of the gastrointestinal tract. Other differential diagnoses include leiomyoma, leiomyosarcoma, fibrosarcoma, and liposarcoma^[26].

Ileum MFH

Primary malignant mesenchymal tumors of the small intestine are seldom found in clinical practice. The occurrence of MFH in the alimentary tract is less well documented in the English literature. In our MEDLINE search we could only yield 11 cases of primary ileum MFH including ours^[1,27-29]. Compared to MFHs in other

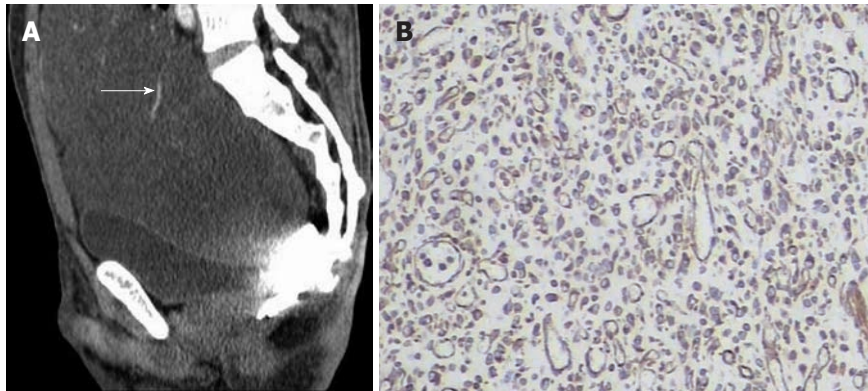


Figure 4 A 34-year-old male with greater omentum malignant fibrous histiocytoma. A: Contrast-enhanced computed tomography scan sagittal view shows a well demarcated cystic mass extending from the abdominal to the pelvic cavity, note the blood vessel on the surface (arrow); B: Immunohistochemistry shows positive staining to vimentin ($\times 400$).

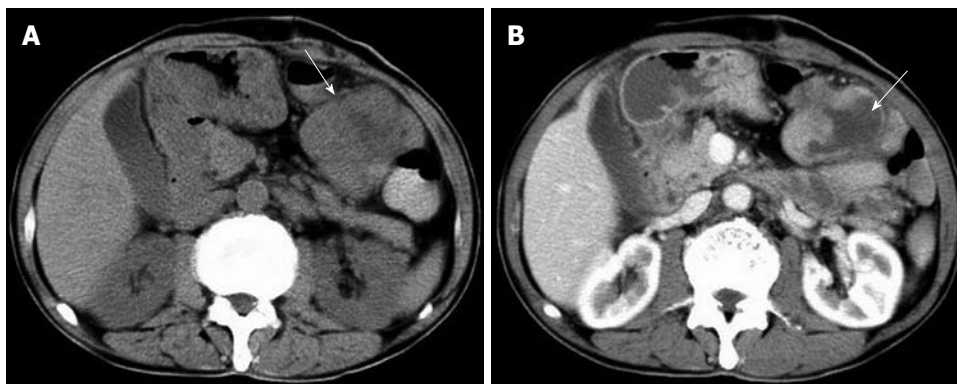


Figure 5 A 64-year-old male with superior mesentery malignant fibrous histiocytoma. A: Non-contrast computed tomography scan shows mass (arrow) in the peritoneal cavity of 33 HU with a clear margin and central area of hypodensity; B: Contrast-enhanced scan venous phase shows mild enhancement with more pronounced central necrotic zone (arrow).

parts of the body, small intestinal MFHs are relatively smaller in size. Patients mainly present with features of obstruction such as abdominal pain, vomiting and melena due to dynamic obstruction by mass or by intussusception. By reviewing previous reports we found that the ileum is the preferred site compared with the duodenum and jejunum. The prognosis associated with ileum MFH is unclear, but most of the reports suggest that it is poor. According to Kobayashi *et al.*^[29], the 1-year survival rate is 53.6% and 2-year survival rate is 42.9%. Primary MFH must also be distinguished from gastrointestinal metastasis or invasions from other parts of the body. We regarded the tumor in our patient to be a primary ileum lesion, rather than an extension of a mesenteric or retroperitoneal tumor, because of the exophytic nature of the lesion with intraluminal and intramural growth (Figure 6). Although this tumor was smaller than the average visceral MFH, CT showed dilatation of the small intestine causing incomplete obstruction with nodules in the pelvic peritoneum which were later confirmed as metastases. A correct diagnosis of MFH in the small intestine is difficult before surgery, because it usually presents as a sub-mucosal tumor. The diagnosis of ileum MFH depends on an accurate differential diagnosis from primary small

intestinal carcinoma and other sarcomas such as pleomorphic liposarcoma and rhabdomyosarcoma.

Retroperitoneal MFH

Retroperitoneal sarcomas represent between 10% to 15% of all soft tissue sarcomas in adults^[30,31]. Previous studies emphasize that most retroperitoneal MFHs are *de novo*. MFH is often referred to as the most usual type of soft-tissue sarcoma. Fletcher *et al.*^[30,31] suggested that it may only represent a common morphologic appearance shared by various soft-tissue sarcomas during their tumoral progression^[32]. The most frequent tumors encountered in this location are liposarcoma, well-differentiated or dedifferentiated types, followed by leiomyosarcoma and MFH. Dedifferentiated liposarcomas mainly occur in the retroperitoneal space, and the most common pattern of dedifferentiated areas consists of high grade pleomorphic MFH or storiform fibroblastic MFH^[33-35]. A recent study reported that a subgroup of MFH was associated with a specific genetic pattern similar to that of dedifferentiated liposarcomas^[36], particularly when they are located in the retroperitoneum. In the retroperitoneal space, MFH represents 7% to 30% of sarcomas^[33]. In our case, CT showed a mass in the right retroperitoneal space, a fat

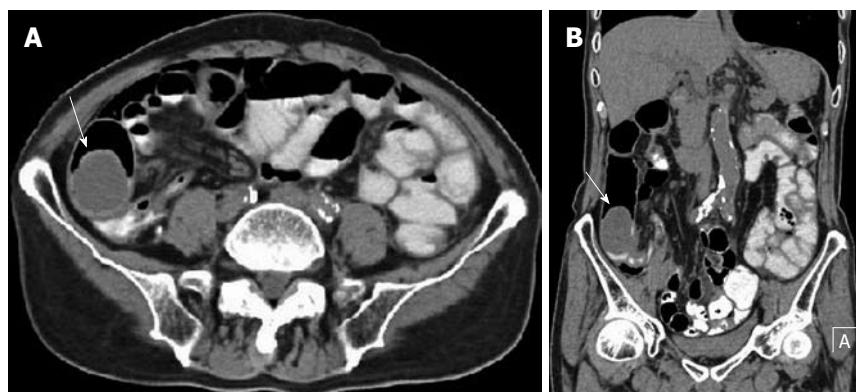


Figure 6 A 79-year-old male with ileum malignant fibrous histiocytoma, plain computed tomography scan abdomen. A, B: Axial (A) and coronal view (B) show intraluminal and intramural soft tissue mass of density 34 HU in the ileo-cecal region (arrows) without significant areas of necrosis. Note the oral contrast stagnation in the proximal loop of the small intestine and dilatation of the ascending colon.

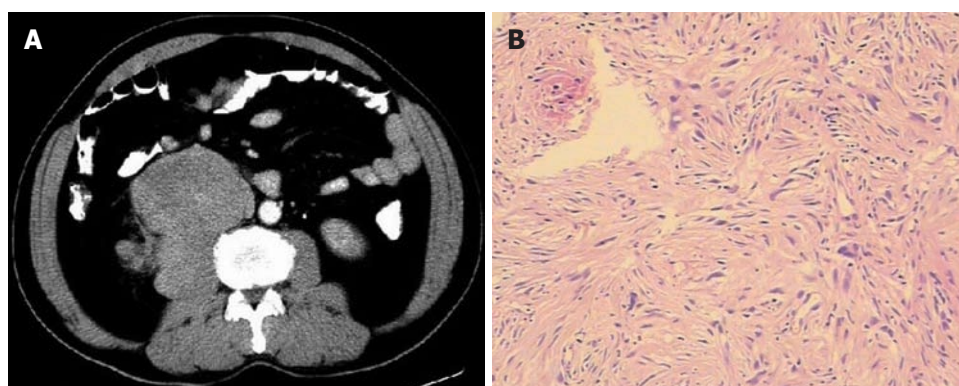


Figure 7 A 59-year-old male with retroperitoneal psoas muscle malignant fibrous histiocytoma. A: Contrast-enhanced computed tomography scan arterial phase shows mass in retroperitoneum with clear margin, no obvious enhancement of mass and area of low density corresponding to necrosis. Note that the fat plane between the mass and psoas muscle is not evident, and the mass seems to be in direct contact with the right psoas muscle; B: Pathological specimen HE stain ($\times 400$) shows spindle to oval tumor cells arranged in a criss-cross fashion.

plane between the mass and the adjacent psoas muscle was not visible. The mass was in direct relation to the psoas muscle with an area of necrosis (Figure 7), and contrast enhancement was mild. Pathological examination revealed the storiform-pleomorphic variety of MFH. With respect to differential diagnosis, differentiation from rhabdomyosarcoma, neurofibroma, lipomatous tumour, leiomyosarcoma, lymphoma and lymph node metastasis may also be difficult. When imaging alone is not conclusive, CT-guided biopsy may be a better alternative due to convenience in the retroperitoneal space.

Kidney MFH

Primary renal MFH is a rare tumor of kidney. To date, there are only 54 reported cases of MFH arising from kidney^[37,38]. The other reported sites of MFH occurring in the genitourinary system are the urinary bladder, prostate and spermatic cord^[39-42]. Kidney MFH is clinically and radiologically indistinguishable from renal cell carcinoma. Patients usually present with abdominal or flank pain, generalized weakness and weight loss. An abdominal mass and hematuria may be evident but are less common. In contrast, these symptoms are seen in renal cell carcinoma

and preoperative differentiation can be difficult^[37]. However, selective renal arteriography usually reveals a hypovascular tumor as compared to renal cell carcinoma^[38]. Our case showed a soft tissue mass with a density of 38 HU on the upper pole of the right kidney (Figure 8). The mass appeared encapsulated with peripheral areas of necrosis and mild enhancement on equilibrium phase.

MFH treatment and prognosis

MFH is an aggressive tumor, with a high local recurrence rate and a significant metastasis rate^[43]. Distant metastasis may spread *via* blood (30%) and the lymphatic system (12%). The risk of local recurrence and distant metastasis correlates with the depth and size of the primary tumor^[4]. The liver is the most common site of sarcoma metastasis, occurring in 64%-70% of patients^[44]. Recurrence of the tumor is not uncommon even when the resection margins are tumor free^[43]. Most reports suggest that the prognosis associated with abdominal MFH is poorer than tumors in the extremities, due to late detection owing to location. Weiss and Einzinger's analysis of MFH^[1,2] showed that the 2-year survival rate with the storiform-pleomorphic type of MFH is 60% and the rate of me-

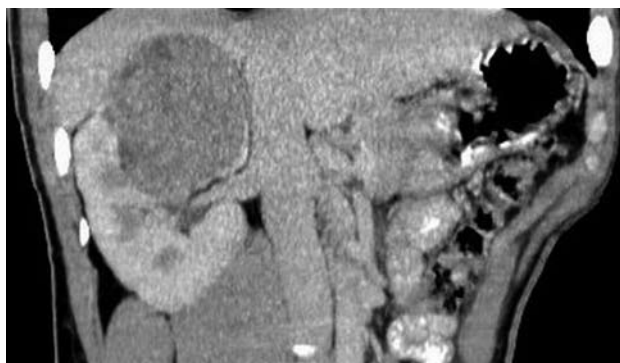


Figure 8 A 23-year-old male with right kidney malignant fibrous histiocytoma. Non-contrast computed tomography scan coronal view shows soft tissue mass of 47 HU in the upper pole of the right kidney extending toward the renal pelvis.

tastases is 42%. Tumor site, location, size, and histology are not significant determinants of final outcome^[45]. For metastasis and relapse, the major determinants are histology (myxoid) and tumor size. Myxoid tumors have low metastatic propensity (13%, 10-year metastatic rate) compared to non-myxoid tumors (40%, 10-year metastatic rate)^[1]. Depending on the stage of disease and the depth of invasion by the tumor, surgical resection is the treatment of choice. Radiotherapy, chemotherapy, and immunotherapy are other therapeutic modalities. Long term follow-up with regular chest X-rays and CT scans of the abdomen to detect tumor recurrence, metastasis and any lymph node involvement are mandatory^[4]. Postoperative recurrent leukocytosis and elevated CRP level may be predictors for recurrence of inflammatory MFH^[1].

In summary, we present a series of patients with MFHs occurring as primary tumors in the abdominal cavity. Although our study consisted of a small sample size, our cases exhibited variable morphological findings at CT. However, signs suggestive of malignancy such as huge size, heterogeneous density, necrotic areas and heterogeneous mild to moderate enhancement were present. On plain CT, most lesions were hypointense and showed areas of low attenuation corresponding to necrosis. On contrast scan, solid components showed variable enhancement, depending on tumor vascularity and extent of necrosis. The intensity of enhancement may be dependent on the amount of fibrosis. Unlike previous findings, there was no evidence of calcification in our cases. Inflammatory varieties were more vascular and had a high metastatic propensity. Thus, we conclude that primary MFH of the abdominal viscera and gastrointestinal tract can be suggested as a diagnosis in a patient with a huge soft tissue mass containing areas of low attenuation and mild to moderate contrast enhancement.

COMMENTS

Background

Malignant fibrous histiocytoma (MFH) is a relatively rare tumor with very limited data which mainly focus on treatment. Thus, the authors retrospectively reviewed the computed tomography (CT) appearance of pathologically diagnosed

cases of abdominal MFH to investigate CT features, which may help in early differentiation and the planning of necessary treatment modalities.

Research frontiers

Knowledge of the CT features of MFH is essential for correct identification and accurate differentiation, which are necessary for effective treatment.

Innovations and breakthroughs

The CT characteristics of abdominal MFH were described. The authors believe that CT which is readily available can better characterize the lesion and identify local and distant metastasis.

Applications

As a starting point in the abdominal imaging work-up, CT always follows ultrasound. This is a very important imaging modality because of its availability and depiction of the tumor mass, which is very important for planning treatment modalities and assessing prognosis. Contrast-enhanced scans should always be added which better delineate tumor vascularity and malignant potential. Authors hope that this illustration of the appearance of MFH helps radiologists and clinicians to achieve an appropriate imaging interpretation and clinical decision.

Peer review

This is not a scientific paper, but a pictorial essay. Abdominal MFH is rare disease and this pictorial essay is therefore important.

REFERENCES

- 1 Fu DL, Yang F, Maskay A, Long J, Jin C, Yu XJ, Xu J, Zhou ZW, Ni QX. Primary intestinal malignant fibrous histiocytoma: two case reports. *World J Gastroenterol* 2007; **13**: 1299-1302
- 2 Weiss SW, Enzinger FM. Malignant fibrous histiocytoma: an analysis of 200 cases. *Cancer* 1978; **41**: 2250-2266
- 3 Kearney MM, Soule EH, Ivins JC. Malignant fibrous histiocytoma: a retrospective study of 167 cases. *Cancer* 1980; **45**: 167-178
- 4 Atmatzidis KS, Pavlidis TE, Galanis IN, Papaziogas BT, Papaziogas TB. Malignant fibrous histiocytoma of the abdominal cavity: report of a case. *Surg Today* 2003; **33**: 794-796
- 5 Stadler FJ, Scott GA, Brown MD. Malignant fibrous tumors. *Semin Cutan Med Surg* 1998; **17**: 141-152
- 6 Huang CC, Ko SF, Ng SH, Lee TY, Wan YL, Lin JW, Chen WJ. Cystic malignant fibrous histiocytoma of the gastrocolic ligament. *Br J Radiol* 2001; **74**: 651-653
- 7 Ros PR, Viamonte M, Rywlin AM. Malignant fibrous histiocytoma: mesenchymal tumor of ubiquitous origin. *AJR Am J Roentgenol* 1984; **142**: 753-759
- 8 Bruneton JN, Drouillard J, Rogopoulos A, Laurent F, Normand F, Balu-Maestro C, Monticelli J. Extraretroperitoneal abdominal malignant fibrous histiocytoma. *Gastrointest Radiol* 1988; **13**: 299-305
- 9 Ko SF, Wan YL, Lee TY, Ng SH, Lin JW, Chen WJ. CT features of calcifications in abdominal malignant fibrous histiocytoma. *Clin Imaging* 1998; **22**: 408-413
- 10 Castillo M, Davis PC, Takei YD, Schwartzberg DG, Hoffman JC. Intracranial cystic malignant fibrous histiocytoma in a child: sonographic and CT findings. *Pediatr Radiol* 1990; **20**: 194-195
- 11 Enzinger FM, Weiss SW. Malignant fibrohistiocytic tumors. In: Stamathis G, editor. *Soft Tissue Tumors*, 2nd ed. St. Louis, MO: Mosby, 1988: 269-300
- 12 Ajisaka H, Maeda K, Uchiyama A, Miwa A. Myxoid malignant fibrous histiocytoma of the breast: report of a case. *Surg Today* 2002; **32**: 887-890
- 13 Kyriakos M, Kempson RL. Inflammatory fibrous histiocytoma. An aggressive and lethal lesion. *Cancer* 1976; **37**: 1584-1606
- 14 Kato T, Kojima T, Shimizu T, Sasaki H, Abe M, Okushiba S, Kondo S, Kato H, Sato H. Inflammatory malignant fibrous histiocytoma of the gallbladder: report of a case. *Surg Today* 2002; **32**: 81-85
- 15 Murata I, Makiyama K, Miyazaki K, Kawamoto AS, Yoshida N, Muta K, Itsuno M, Hara K, Nakagoe T, Tomita M. A case of inflammatory malignant fibrous histiocytoma of the colon.

- Gastroenterol Jpn* 1993; **28**: 554-563
- 16 **Rosenberg AE**. Malignant fibrous histiocytoma: past, present, and future. *Skeletal Radiol* 2003; **32**: 613-618
- 17 **Yu RS**, Chen Y, Jiang B, Wang LH, Xu XF. Primary hepatic sarcomas: CT findings. *Eur Radiol* 2008; **18**: 2196-2205
- 18 **Ding GH**, Wu MC, Yang JH, Cheng SQ, Li N, Liu K, Dai BH, Cong WM. Primary hepatic malignant fibrous histiocytoma mimicking cystadenocarcinoma: a case report. *Hepatobiliary Pancreat Dis Int* 2006; **5**: 620-623
- 19 **Anagnostopoulos G**, Sakorafas GH, Grigoriadis K, Kostopoulos P. Malignant fibrous histiocytoma of the liver: a case report and review of the literature. *Mt Sinai J Med* 2005; **72**: 50-52
- 20 **Ferrozzi F**, Bova D. Hepatic malignant fibrous histiocytoma: CT findings. *Clin Radiol* 1998; **53**: 699-701
- 21 **Yu JS**, Kim KW, Kim CS, Yoon KH, Jeong HJ, Lee DG. Primary malignant fibrous histiocytoma of the liver: imaging features of five surgically confirmed cases. *Abdom Imaging* 1999; **24**: 386-391
- 22 **Wunderbaldinger P**, Schima W, Harisinghani M, Saini S. Primary malignant fibrous histiocytoma of the liver: CT and MR findings. *AJR Am J Roentgenol* 1998; **171**: 900-901
- 23 **Chen HC**, Chen CJ, Jeng CM, Yang CM. Malignant fibrous histiocytoma presenting as hemoperitoneum mimicking hepatocellular carcinoma rupture. *World J Gastroenterol* 2007; **13**: 6441-6443
- 24 **Kweon JH**, Choi CS, Im CJ, Seo GS, Choi SC. Malignant fibrous histiocytoma arising from the omentum presenting as hemoperitoneum. *Gut Liver* 2010; **4**: 241-244
- 25 **Goldman SM**, Hartman DS, Weiss SW. The varied radiographic manifestations of retroperitoneal malignant fibrous histiocytoma revealed through 27 cases. *J Urol* 1986; **135**: 33-38
- 26 **Kim HC**, Lee JM, Kim SH, Kim KW, Lee M, Kim YJ, Han JK, Choi BI. Primary gastrointestinal stromal tumors in the omentum and mesentery: CT findings and pathologic correlations. *AJR Am J Roentgenol* 2004; **182**: 1463-1467
- 27 **Hasegawa S**, Kawachi H, Kurosawa H, Obi Y, Yamanaka K, Nakamura K, Abe T. Malignant fibrous histiocytoma in the ileum associated with intussusception. *Dig Dis Sci* 2004; **49**: 1156-1160
- 28 **Kotan C**, Kosem M, Alici S, Ilhan M, Tuncer I, Harman M. Primary malignant fibrous histiocytoma of the small intestine presenting as an intussusception: report of a case. *Surg Today* 2002; **32**: 1091-1095
- 29 **Kobayashi K**, Narita H, Morimoto K, Hato M, Ito A, Sugiyama K. Primary malignant fibrous histiocytoma of the ileum: report of a case. *Surg Today* 2001; **31**: 727-731
- 30 **Fletcher CD**, Gustafson P, Rydholm A, Willén H, Akerman M. Clinicopathologic re-evaluation of 100 malignant fibrous histiocytomas: prognostic relevance of subclassification. *J Clin Oncol* 2001; **19**: 3045-3050
- 31 **Fletcher CD**. Pleomorphic malignant fibrous histiocytoma: fact or fiction? A critical reappraisal based on 159 tumors diagnosed as pleomorphic sarcoma. *Am J Surg Pathol* 1992; **16**: 213-228
- 32 **Fabre-Guillevin E**, Coindre JM, Somerhausen Nde S, Bonichon F, Stoeckle E, Bui NB. Retroperitoneal liposarcomas: follow-up analysis of dedifferentiation after clinicopathologic reexamination of 86 liposarcomas and malignant fibrous histiocytomas. *Cancer* 2006; **106**: 2725-2733
- 33 **Coindre JM**, Mariani O, Chibon F, Mairal A, De Saint Aubain Somerhausen N, Favre-Guillevin E, Bui NB, Stoeckle E, Hostein I, Aurias A. Most malignant fibrous histiocytomas developed in the retroperitoneum are dedifferentiated liposarcomas: a review of 25 cases initially diagnosed as malignant fibrous histiocytoma. *Mod Pathol* 2003; **16**: 256-262
- 34 **McCormick D**, Mentzel T, Beham A, Fletcher CD. Dedifferentiated liposarcoma. Clinicopathologic analysis of 32 cases suggesting a better prognostic subgroup among pleomorphic sarcomas. *Am J Surg Pathol* 1994; **18**: 1213-1223
- 35 **Henricks WH**, Chu YC, Goldblum JR, Weiss SW. Dedifferentiated liposarcoma: a clinicopathological analysis of 155 cases with a proposal for an expanded definition of dedifferentiation. *Am J Surg Pathol* 1997; **21**: 271-281
- 36 **Chibon F**, Mariani O, Derré J, Malinge S, Coindre JM, Guilhou L, Lagacé R, Aurias A. A subgroup of malignant fibrous histiocytomas is associated with genetic changes similar to those of well-differentiated liposarcomas. *Cancer Genet Cytogenet* 2002; **139**: 24-29
- 37 **Kim SJ**, Ahn BC, Kim SR, Kim YB, Joo HJ, Lee KB, Kim YS. Primary malignant fibrous histiocytoma of the kidney. *Yonsei Med J* 2002; **43**: 399-402
- 38 **Matsui Y**, Kobayashi S, Sugino Y, Iwamura H, Oka H, Fukuzawa S, Takeuchi H. [Malignant fibrous histiocytoma originating in a renal capsule: a case report]. *Hinyokika Kiyo* 2001; **47**: 727-729
- 39 **Goodman AJ**, Greaney MG. Malignant fibrous histiocytoma of the bladder. *Br J Urol* 1985; **57**: 106-107
- 40 **Zhang G**, Chen KK, Manivel C, Fraley EE. Sarcomas of the retroperitoneum and genitourinary tract. *J Urol* 1989; **141**: 1107-1110
- 41 **Kulmala RV**, Seppänen JH, Vaajalahti PJ, Tammela TL. Malignant fibrous histiocytoma of the prostate. Case report. *Scand J Urol Nephrol* 1994; **28**: 429-431
- 42 **Glazier DB**, Vates TS, Cummings KB, Pickens RL. Malignant fibrous histiocytoma of the spermatic cord. *J Urol* 1996; **155**: 955-957
- 43 **Lee YT**. Leiomyosarcoma of the gastro-intestinal tract: general pattern of metastasis and recurrence. *Cancer Treat Rev* 1983; **10**: 91-101
- 44 **Qureshi NA**, Hallissey MT, Fielding JW, Gourevitch D. Primary intra-abdominal malignant fibrous histiocytoma presenting as pyrexia of unknown origin--report of a case with review of literature. *Int Semin Surg Oncol* 2006; **3**: 15
- 45 **Zagars GK**, Mullen JR, Pollack A. Malignant fibrous histiocytoma: outcome and prognostic factors following conservation surgery and radiotherapy. *Int J Radiat Oncol Biol Phys* 1996; **34**: 983-994

S- Editor Cheng JX L- Editor Webster JR E- Editor Zheng XM



Multimodal morphometry and functional magnetic resonance imaging in schizophrenia and auditory hallucinations

Gracián García-Martí, Eduardo Jesús Aguilar, Luis Martí-Bonmatí, M José Escartí, Julio Sanjuán

Gracián García-Martí, Eduardo Jesús Aguilar, M José Escartí, Julio Sanjuán, CIBERSAM, University of Valencia, Avenue Blasco Ibañez 15, 46010 Valencia, Spain

Gracián García-Martí, Department of Radiology, Quiron Hospital, Avenue Blasco Ibañez 14, 46010 Valencia, Spain

Eduardo Jesús Aguilar, Psychiatry Service, Sagunto Hospital, Avenue Ramón y Cajal unnumbered, 46520 Sagunto, Spain

Luis Martí-Bonmatí, Radiology Unit, Medicine Department, University of Valencia, Avenue Blasco Ibañez 15, 46010 Valencia, Spain

M José Escartí, Julio Sanjuán, Psychiatry Service, Clinic University Hospital, Avenue Blasco Ibañez 15, 46010 Valencia, Spain

Author contributions: All authors have contributed sufficiently to this manuscript and meet the authorship standards established by the International Committee of Medical Journal Editors; all authors and their institutions approved this work and agreed with the exposed data; Aguilar EJ wrote the first draft which was revised by the rest of the authors; all authors approved the final version and discussed the conception of the study and interpretation of data; García-Martí G acquired magnetic resonance data and performed data analysis; Martí-Bonmatí L designed the coincidence methodology and was supported by García-Martí G in technical aspects; Aguilar EJ, Escartí MJ and Sanjuán J are the psychiatrists in charge of patients.

Supported by The research network CIBERSAM

Correspondence to: Gracián García-Martí, Cp. D, PhD, CIBERSAM, Faculty of Medicine, University of Valencia, Avenue Blasco Ibañez 15, 46010 Valencia, Spain. gracian.garcia@gmail.com

Telephone: +34-96-3983379 Fax: +34-91-5570812

Received: January 4, 2012 Revised: March 31, 2012

Accepted: April 7, 2012

Published online: April 28, 2012

and Statistical Manual of Mental Disorders (fourth edition, DSM-IV) criteria for schizophrenia and experiencing persistent hallucinations together with 28 healthy controls were evaluated with structural and functional MR imaging with an auditory paradigm designed to replicate those emotions related to the patients' hallucinatory experiences. Coincidence maps were obtained by combining structural maps of gray matter reduction with emotional functional increased activation. Abnormal areas were correlated with the brief psychiatric rating scale (BPRS) and the psychotic symptom rating scale (PSYRATS) scales.

RESULTS: The coincidence analysis showed areas with coexistence gray matter reductions and emotional activation in bilateral middle temporal and superior temporal gyri. Significant negative correlations between BPRS and PSYRATS scales were observed. BPRS scores were negatively correlated in the middle temporal gyrus (right) ($t = 6.86$, $P = 0.001$), while negative PSYRATS correlation affected regions in both the superior temporal gyrus (left) ($t = 7.85$, $P = 0.001$) and middle temporal gyrus (left) ($t = 4.97$, $P = 0.002$).

CONCLUSION: Our data identify left superior and middle temporal gyri as relevant areas for the understanding of auditory hallucinations in schizophrenia. The use of multimodal approaches, sharing structural and functional information, may demonstrate areas specifically linked to the severity of auditory hallucinations.

© 2012 Baishideng. All rights reserved.

Abstract

AIM: To validate a multimodal [structural and functional magnetic resonance (MR)] approach as coincidence brain clusters are hypothesized to correlate with clinical severity of auditory hallucinations.

METHODS: Twenty-two patients meeting Diagnostic

Key words: Functional; Morphometry; Magnetic resonance; Schizophrenia; Auditory hallucinations; Multimodal; Coincidence

Peer reviewer: Eduardo J Aguilar, MD, PhD, Coordinador de Salud Mental, Psiquiatría, Hospital de Sagunto, Avda. Ramón y Cajal s/n, 46520 Sagunto, Spain

García-Martí G, Aguilar EJ, Martí-Bonmatí L, Escartí MJ, Sanjuán J. Multimodal morphometry and functional magnetic resonance imaging in schizophrenia and auditory hallucinations. *World J Radiol* 2012; 4(4): 159-166. Available from: URL: <http://www.wjgnet.com/1949-8470/full/v4/i4/159.htm> DOI: <http://dx.doi.org/10.4329/wjr.v4.i4.159>

INTRODUCTION

Schizophrenia is a heterogeneous illness with neurobiological underpinnings that are not fully understood. Recent neuroimaging techniques have helped to disentangle brain mechanisms that may explain distinct aspects of this deteriorating condition. Several neuroimaging modalities may be combined to create multimodal approaches, which will undoubtedly help to enhance our knowledge clarifying the neurobiological basis of this illness.

Relevant data have been obtained from several magnetic resonance (MR) imaging unimodal studies using structural (morphometric MR imaging, mMRI), functional (functional MR imaging, fMRI), diffusion-tensor imaging and MR spectroscopy; mMRI and fMRI are currently the most extensively used techniques in the field. Structural abnormalities in patients with schizophrenia have repeatedly been demonstrated with the use of region of interest approaches and with non-hypothetically-driven techniques such as voxel-based morphometry (VBM)^[1-7]. In 15 evaluated studies, Honea *et al*^[1] found that gray matter reductions in the left medial and superior temporal areas were the most frequently reported. However, this has been confronted by a recent meta-analysis that failed to demonstrate a crucial role for the superior temporal gyrus in schizophrenia^[8]. Several neuropathological processes may be merging in patients with schizophrenia and those related to the pathogenesis of auditory hallucinations may be overshadowed. In addition to technical difficulties inherent to meta-analytic techniques, disease heterogeneity may further obscure relevant findings for a particular manifestation such as auditory hallucinations, considering that some brain abnormalities may be present only in a particular subgroup of patients. This has been confirmed in a recent meta-analysis that has demonstrated a relevant role for the superior temporal gyrus and other fronto-temporal areas in the pathogenesis of auditory hallucinations^[9]. However, although other brain areas may be involved, functional studies and sound theoretical models suggest that the superior temporal gyrus is a key area affecting auditory hallucinations^[10].

Multimodal approaches based on a combination of techniques will help to improve our knowledge of this illness. Only a few multimodal studies are currently available for patients with schizophrenia. Calhoun *et al*^[11] used a joint independent component analysis to analyze gray matter and fMRI activation images. They found group differences between schizophrenic patients and controls in the bilateral parietal, frontal and posterior temporal regions in gray matter associated with bilateral temporal

regions activated by auditory oddball target stimuli. Bilateral anterior temporal lobe regions were found to have less gray matter in patients with schizophrenia and less hemodynamic activity for target detection. Resting state fMRI has several potential advantages over task-activation fMRI in terms of its clinical applicability^[12]. Lui *et al*^[13] used optimized VBM and resting state functional connectivity analysis in a sample of 68 antipsychotic-naïve first-episode schizophrenia patients and 68 matched healthy controls. They reported that clinical symptom severity assessed by Global Assessment of Function and Positive and Negative Syndrome Scale was associated with alterations in gray matter reductions in the right superior temporal gyrus, right middle temporal gyrus and functional temporal regions.

Functional studies designed to approach a specific symptom or dimension together with VBM studies on a highly homogeneous group of patients may be useful to clarify the biological basis of a disease. Horn *et al*^[14] reported overlapping gray matter deficits in the left posterior superior temporal gyrus and left angular gyrus when using VBM and resting fMRI in 13 patients with schizophrenic formal thought disorder. They also observed positive correlations between the severity of formal thought disorder and both functional alterations and gray matter deficits in several brain regions.

One approach to validate a neuroimaging technique based on the MR analysis of coincidence between gray matter loss and emotional auditory functional activation^[15] is to search for correlations between auditory hallucinations severity and multivariate coinciding clusters in specific brain areas.

The purpose of this study was to evaluate if MR functional abnormalities associated with auditory emotional stimuli coexist with focal brain reductions in schizophrenic patients with persistent auditory hallucinations. Our assumptions are focused on the functional segregation of the brain, looking for areas specifically linked to the pathogenesis of auditory hallucinations using a block design paradigm. We hypothesized that there will be a specific correlation with brief psychiatric rating scale (BPRS) and psychotic symptom rating scale (PSYRATS) scales between coinciding clusters in the superior temporal gyrus and the severity of auditory hallucinations.

MATERIALS AND METHODS

The study sample comprised 50 subjects. Twenty-two patients exhibited DSM-IV (Diagnostic and Statistical Manual of Mental Disorders, fourth edition) schizophrenia and persistent auditory hallucinations with a mean age of 29.8 ± 11.7 years (range 22-34 years) and a mean disease duration of 13.6 years. Twenty-eight control subjects were also evaluated using the same protocol; the mean age of the control group was 31.9 ± 11 years (range 20-70 years). All patients and subjects were right-handed and male to reduce confounding bias within the population. Handedness was assessed with the Edinburgh

Table 1 Clinical and demographic data (mean \pm SD)

	Schizophrenia with auditory hallucinations (<i>n</i> = 22)	Control subjects (<i>n</i> = 28)
Age (yr)	29.78 \pm 11.68	31.89 \pm 11.01
Age first hallucinations (yr)	21.86 \pm 12.21	-
Illness duration (yr)	13.55 \pm 6.72	-
GAF	39.86 \pm 10.34	-
BPRS	53.86 \pm 8.51	-
PSYRATS	33.91 \pm 15.21	-
PANSS total	73.36 \pm 16.01	-
PANSS positive	19.86 \pm 4.77	-
PANSS negative	18.23 \pm 7.78	-
PANSS general	35.27 \pm 8.39	-

GAF: Global assessment of function; BPRS: Brief psychiatric rating scale; PSYRATS: Psychotic symptom rating scale; PANSS: Positive and negative syndrome scale.

Questionnaire^[16]. None of the patients had problems of hearing loss. Table 1 shows the most relevant clinical and demographic variables.

All patients met the following selection criteria for persistent hallucinations: (1) persistence of hallucinations even after the use of two antipsychotic drugs at doses equivalent to at least 600 mg/d of chlorpromazine within the last year; (2) voices unmodified in any way by treatment; and (3) voices present at least once per day within the past year. Patients were assessed for general psychopathology using the BPRS^[17] and for severity of auditory hallucinations using the PSYRATS^[18]. At the end of the trial, every subject was asked if they have experienced hallucinations during the scanning.

The local ethics committee approved this study, and all the participants gave written informed consents.

Data acquisition

MR images were acquired on a 1.5 T MR magnet (Intera, Philips Medical Systems, Best, Netherlands). fMRI images were obtained with a dynamic Echo Planar Imaging T2* weighted sequence (TR = 2000 ms, TE = 50 ms, 5 mm slice thickness with no inter-slice gap, 24 slices; acquisition matrix = 128 \times 128, field of view = 220 mm and flip angle = 65°, voxel size = 1.72 mm \times 1.72 mm \times 5.0 mm). Additionally, a high spatial resolution 3D spoiled gradient echo T1-weighted MR sequence was employed to obtain an entire set of brain images with 96 axial slices covering the whole brain (TR = 7 ms, TE = 1.9 ms, 1.25 mm section thickness with no inter-slice gap; acquisition matrix = 256 \times 256, field of view = 220 mm and flip angle = 8°, achieving a voxel size of 0.86 mm \times 0.86 mm \times 1.25 mm).

Auditory paradigm

The auditory paradigm was previously defined by our group^[19]. So that the selection of the words with emotional content was specific for psychosis, 82 patients with schizophrenia according to DSM-IV criteria and who had suffered auditory hallucinations according to their clinical

record were selected. Patients were asked about the words of their hallucinations which were recorded on a tape recording machine. These recordings were transcribed and the most frequently appearing words were analyzed. A total of 13 emotional words were chosen and were distributed in four categories: 4 negative content imperative words, 3 insults, 2 with imperative tone, 2 exclamations related with emotions, and 2 having positive content. Additionally, 13 words with neutral content were selected to match the emotional ones according to their pleasantness and the number of syllables.

Design

The fMRI design consists of 4 blocks with 20 s long stimuli mixed with 4 blocks with 20 s of rest. The order of both acquisitions (emotional and neutral) was random to avoid introducing bias (adaptation, tiredness, saturation surprise). Two sessions (neutral and emotional) were presented to each subject. Each session consisted of 80 dynamics (2 s long each one) covering the entire brain, assigning 10 dynamics to each block. The global duration of the sequence was 160 s. During the experiment, 4 blocks in rest and 4 during activation were alternately studied. Subjects wore earphones adjusted to their heads and connected by a pair of air tubes to an external audio compact disc player. Both sessions were separated by no less than 40 s.

Data processing

SPM5 software (<http://www.fil.ion.ucl.ac.uk/spm>) was used to process structural and functional data. The tests were performed using MATLAB version 6.5 (The MathWorks, Natick, MA, USA) under LINUX platform.

Structural analysis

Anatomical differences between patients and healthy subjects were measured using the optimized VBM protocol. Custom templates were created in order to minimize the bias induced by using standard anatomical templates in the normalization processes. This process involved the normalization of each raw image with the International Consortium for Brain Mapping 152 template as a reference, applying a 12-parameter affine transformation. The normalized images were segmented to obtain gray matter, white matter and cerebrospinal fluid maps, which were averaged and smoothed with an 8 mm \times 8 mm \times 8 mm full width at half maximum (FWHM) filter.

These templates were used for the normalization of each original T1 MR image. Normalized data was then segmented to obtain gray matter, white matter and cerebrospinal fluid tissue maps. At this stage, the segmentation process involved a cleaning process, removing non-useful tissue like scalp, skull and dural venous sinus. A non-linear spatial normalization process between segmented images and templates were estimated and applied to warp the original T1 images. Images were interpolated to 1 mm \times 1 mm \times 1 mm voxels. Finally, warped images were segmented and smoothed by a 12 mm \times 12 mm \times 12 mm FWHM Gaussian kernel.

Table 2 Relevant areas showing gray matter density reduction in schizophrenic patients with auditory hallucinations when compared with control subjects

Coordinates (mm)			Label	Hemisphere	<i>t</i> value	<i>P</i> _{corrected}	Brodmann area
X	Y	Z					
-42	10	-11	Insula	L	7.41	0.001	48
59	-33	50	Insula	R	7.39	0.001	48
-54	-19	4	Superior temporal gyrus	L	5.69	0.001	22
-5	42	14	Anterior cingulate gyrus	L	5.36	0.001	32
66	-16	3	Superior temporal gyrus	R	5.15	0.001	22
52	-48	36	Inferior parietal gyrus	R	5.05	0.001	40
-61	-53	16	Middle temporal gyrus	L	4.85	0.002	21
19	-3	-13	Amygdala	R	4.75	0.002	34
60	-42	4	Middle temporal gyrus	R	4.55	0.002	22
-20	1	-15	Amygdala	L	4.45	0.003	34

P < 0.005 false discovery rate corrected, *k* = 45.

Functional analysis

To process fMRI data, spatial (realignment) and temporal (slice timing) corrections were applied to eliminate head motion effects and to correct for the delay between acquisition of the first and last slices. Images were then transformed to standard space (MNI350, Montreal Neurological Institute) and smoothed by a three-dimensional 6 mm × 6 mm × 6 mm FWHM kernel. In the individual analysis, a design matrix was defined for each subject. Both an ideal hemodynamic response function and the mean value of each fMRI session were included in the design matrix.

Contrast images of subtraction between emotional and non-emotional content words (both against the rest task) were then extracted for every schizophrenic and control subject. These images were considered to be maps of emotional activation associated with the auditory stimulus. A two sample *t*-test map was calculated testing the differences in activation between both groups of subjects and patients for the contrast of subtraction referred before (Random Effects Analyses were applied).

Statistical analysis

Statistical analyses were performed under the General Linear Model framework. Although the sample was quite homogeneous, two covariates of interest for each subject (age and total intracranial volume) were included in the designed model. Statistical parametric maps were obtained by performing Student-*t* tests voxel-by-voxel, using SPM one-tailed contrasts in order to measure interactions between groups (patients < controls and patients > controls).

To perform the correlation analysis between PSYRATS and BPRS scales with the affected areas, a new statistical model was built. Maps of coincidence, PSYRATS and BPRS scores, total intracranial volume and age factor were included in a General Linear Model design matrix.

Significance criteria were established by using a *P* < 0.005 and a correction for multiple comparisons following the false discovery rate (FDR) methodology. Only areas with a minimum expected number of voxels per

cluster (*k*) of 45 were reported and labeled with the Automated Anatomical Labeling software. The coordinates were defined by the maximum Student-*t* value in the corresponding brain areas.

Maps of coincidence

Both contrast images with gray matter reduction (gray matter_{patients} < gray matter_{controls}) and maps of emotional hyperactivation in the schizophrenic patients (emotional_{patients} > emotional_{controls}) were overlaid in order to depict the common abnormalities found out by both techniques. The coincidence map was then voxel-by-voxel generated multiplying the emotional functional images with the gray matter concentration differences maps, so that the higher the activation area and the higher the concentration differences, the more highlighted that area would appear. This procedure allowed determination of whether fMRI activation areas associated with hearing emotional words were coincident with focal brain gray matter reductions.

RESULTS

There were no significant differences in age between both groups (*t* = 0.81, *P* = 0.85). Additionally, total intracranial volume did not differ between schizophrenic patients (1266.8 ± 68.4 mL) and control subjects (1195.3 ± 64.2 mL) (*t* = 1.33, *P* = 0.72). As expected, schizophrenic patients with auditory hallucinations showed gray matter density reductions when compared with control subjects. The most relevant areas with significant gray matter reductions were the insula (bilateral), the superior temporal gyrus (bilateral), anterior cingulate gyrus (left), inferior parietal gyrus (right), middle temporal gyrus (bilateral) and amygdala (bilateral) (Table 2, *P* < 0.005 FDR corrected, *k* = 45).

In fMRI experiments, significant areas of emotional auditory activation were primarily found in schizophrenic patients when comparing with control subjects in the middle temporal gyrus (bilateral), superior temporal gyrus (bilateral), amygdala (bilateral), hippocampus (left) and precuneus (right) (Table 3, *P* < 0.005 FDR corrected, *k* = 45).

Table 3 Relevant areas of emotional activation in schizophrenic patients with auditory hallucinations

Coordinates (mm)			Label	Hemisphere	<i>t</i> value	<i>P</i> _{corrected}	Brodmann area
X	Y	Z					
-53	4	-17	Middle temporal pole	L	15.53	0.000	21
54	-10	-12	Middle temporal gyrus	R	14.68	0.000	22
-56	-23	-3	Superior temporal gyrus	L	14.55	0.000	22
58	-7	-3	Superior temporal gyrus	R	14.69	0.000	22
-22	-1	-17	Amygdala	L	11.89	0.000	34
-21	-29	-3	Hippocampus	L	10.65	0.000	27
50	-11	-9	Middle temporal gyrus	R	9.88	0.001	22
1	-52	15	Precuneus	R	9.71	0.001	30
21	-5	-17	Amygdala	R	8.05	0.001	34

$P < 0.005$ false discovery rate corrected, $k = 45$.

Table 4 Areas showing concordance between gray matter reductions and emotional activation in schizophrenic patients with auditory hallucinations

Coordinates (mm)			Label	Hemisphere	Brodmann area
X	Y	Z			
-59	-53	4	Middle temporal gyrus	L	21
-53	-17	4	Superior temporal gyrus	L	48
66	-20	3	Superior temporal gyrus	R	22
62	-47	10	Middle temporal gyrus	R	21

$P < 0.005$ false discovery rate corrected, $k = 45$.

Table 5 Areas negatively correlated between brief psychiatric rating scale and the psychotic symptom rating scale in areas of coincidence between gray matter reduction and emotional activation

Coordinates (mm)			Label	Hemisphere	<i>t</i> value	<i>p</i> _{corrected}	Brodmann area
X	Y	Z					
BPRS							
61	-50	5	Middle temporal gyrus	R	6.86	0.001	21
PSYRATS							
-56	-15	7	Superior temporal gyrus	L	7.85	0.001	48
-59	-52	15	Middle temporal gyrus	L	4.97	0.002	21

$P < 0.005$ false discovery rate corrected, $k = 45$. BPRS: Brief psychiatric rating scale; PSYRATS: Psychotic symptom rating scale.

The coincidence analysis showed areas with concomitant gray matter reductions and abnormal emotional activation in the middle temporal gyrus (bilateral) and superior temporal gyrus (bilateral) (Table 4) in schizophrenic patients.

Values of the BPRS and PSYRATS scales evaluated in the schizophrenic patients group were 53.86 ± 8.51 and 33.91 ± 15.21 , respectively. Significant negative correlations between these scales were observed with the coincidence areas ($P < 0.005$ FDR corrected, $k = 45$). The BPRS variable was negatively correlated in the middle temporal gyrus (right) ($r^2 = 0.62$, $P = 0.001$), while negative PSYRATS correlation affected regions in both the superior temporal gyrus (left) ($r^2 = 0.68$, $P = 0.001$) and middle temporal gyrus (left) ($r^2 = 0.51$, $P = 0.002$) (Table 5, Figure 1). No linear correlation was found between BPRS and PSYRATS covariates ($R = 0.08$).

DISCUSSION

By means of coincidence parametric maps applied on patients with schizophrenia, we have demonstrated the presence of neuronal clusters located in the left superior temporal and bilateral middle temporal gyri with both functional abnormal activation after an emotional auditory paradigm and gray matter reduction.

Auditory hallucinations bilaterally activate the superior and middle temporal gyri. Bilateral middle temporal gyri have been involved in emotion^[20]. Structures activated during the perception of external voices are also activated during auditory hallucinations with the additional activation found in areas responsible for the processing of emotion^[10]. Data are consistent on a negative correlation between the left superior temporal gyrus volumes and auditory hallucinations^[2]. This finding was expected

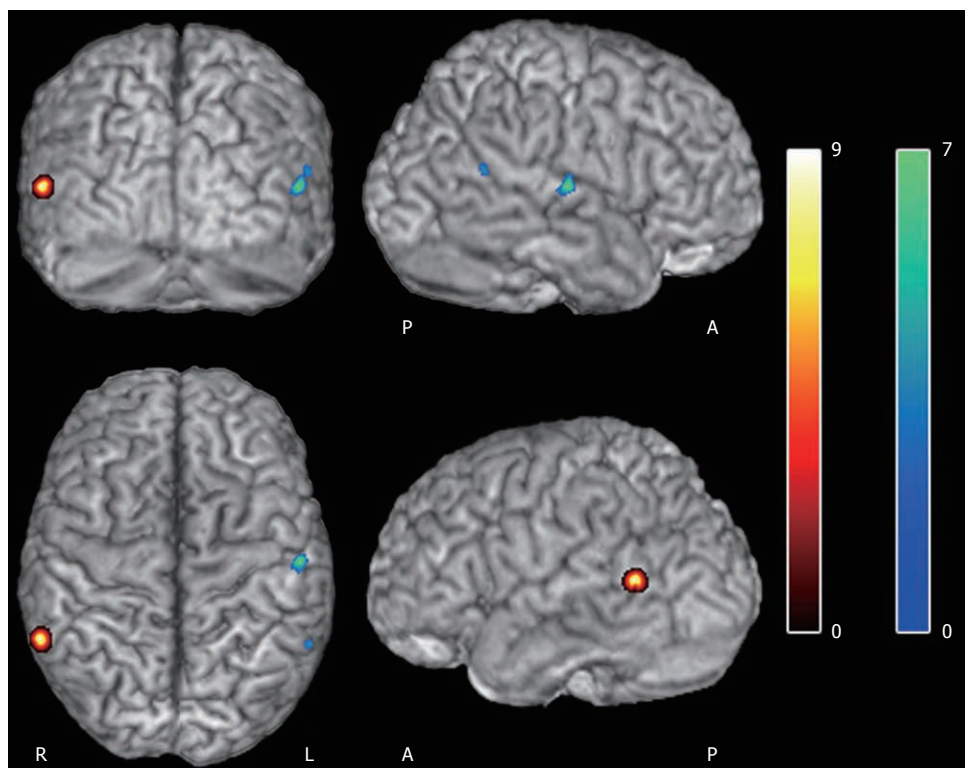


Figure 1 Areas of negative correlation between brief psychiatric rating scale (yellow-red bar) and psychotic symptom rating scale (green-blue bar) scales in areas of coincidence (gray matter reduction and abnormal emotional activation). $P < 0.005$ false discovery rate corrected, $k = 45$.

according to the emotional task that was used in the experiment which was designed to elicit the emotional response that patients with schizophrenia have when facing their auditory verbal hallucinations. It is a task aimed to draw out the key areas involved in the pathogenesis of auditory hallucinations and is therefore concordant with many studies of functional auditory stimulation.

It is not surprising that the superior temporal gyrus and middle temporal gyrus are key elements of all pathological models which have been proposed to explain auditory hallucinations. Most of the activity studies have shown that auditory hallucinations are also associated to regional blood flow increases in the left superior temporal gyrus and other fronto-temporal areas^[9]. A neurophysiological interaction among psychopathology (auditory hallucinations), brain function (increased hemodynamic) and structure (gray matter deficits) has been previously hypothesized^[15]. It is generally accepted that areas of decreased perfusion parallel decreases in gray matter concentration as occurs with age-related brain reduction, which is probably associated with a decrease in blood flow and metabolism in those areas. Nevertheless, our findings suggest the contrary effect, showing that in schizophrenic patients an abnormal hyperactivation is found in specific areas of maximal neural density decrement. These areas of coincidence where the same voxels have hemodynamic functional changes associated with the emotional auditory-triggered response and focal decreased density may express a compensation phenomenon in which regions with decreased volume need a

larger hemodynamic response to a well-defined paradigm.

An influential model for the pathogenesis of auditory hallucinations in which the superior temporal and middle temporal gyri are key areas has been postulated^[10]. A “top-down” network, presenting an altered activation in speech production areas (i.e., inferior frontal gyrus) and altered coupling with monitoring areas (anterior cingulate) and language reception areas (Wernicke’s area) was suggested. There would also be a “bottom-up” dysfunction through over-activation of secondary and occasionally primary sensory cortices that lead to the experience of vivid perceptions in the absence of sensory stimuli.

The neurobiological basis for temporal gyrus volume reduction is unknown. Abnormal brain maturation processes influenced by multiple genes interact with other potentially causative factors for psychoses such as substance abuse, stress and dysregulation of the hypothalamic-pituitary-adrenal axis function. Other factors may also interfere including poor diet and exercise, smoking, psychosocial and socioeconomic influences, and associated physical comorbidity as well as neuroleptics and other medications^[21].

Structural and functional abnormalities in the superior temporal and middle temporal gyrus may also be relevant in the pathogenesis of schizophrenia. Several findings support the idea that decreasing superior temporal gyrus volume is a potential endophenotype for schizophrenia-spectrum disorders. Firstly, an MR imaging study in 29 young, non-psychotic subjects with a schizophrenic parent had reported bilateral superior temporal gyrus volume

reduction compared to controls with no psychiatric family history^[22]. Secondly, reduced superior temporal gyrus volume has been consistently reported in patients with schizotypal personality disorder^[23]. The superior temporal gyrus is also particularly affected during the first years of illness through progressive gray matter reductions. This is the case even during the prodromal phase and probably has clinical implications^[24].

The study presented here contains several limitations. Our relatively small sample size may have hampered the ability to detect significant correlations in other potentially relevant areas, although it has been reported that a sample of 20 or more subjects is sufficient to obtain reliable functional neuroimaging data^[25]. The results obtained from a high homogeneous sample (only schizophrenic patients with persistent auditory hallucinations were included) cannot be generalized to all patients with schizophrenia. We assessed our multimodal approach to be a strategy for determining brain areas that should be further assessed to study the neurobiological basis of one particular symptom or aspect of a disorder. Additionally, hallucinatory experiences during fMRI scanning were answered subjectively according to the patients' perception, with the subsequent lack of certainty derived from this qualitative approach. Finally, all our study patients were medicated with a wide range of first- and second-generation antipsychotics. Our findings can hardly be attributed to medication. In fact, a recent study in antipsychotic-naïve first-episode schizophrenia with [(18)F] fluorodeoxyglucose (FDG) positron emission tomography has shown that patients experiencing auditory hallucinations during FDG uptake had significantly higher metabolic rates in the left superior and middle temporal cortices, and other brain areas^[26]. Moreover, a neuroleptic-naïve sample would have been out of the scope of this study, as we have chosen to include a highly homogeneous sample of patients based on their refractory behavior to antipsychotic medications.

In conclusion, we identified the left superior and middle temporal gyri as relevant areas in patients with auditory hallucinations. Our findings provide support for the use of multimodal structural and functional MR approaches in the search for areas specifically linked to the pathogenesis of auditory hallucinations. This core approach appears to be a good strategy for studying the neurobiological basis of clinical dimensions which may be particularly indicated at this stage. Similar multimodal approaches could also be used for studying other features as long as specific paradigms for the functional study of such symptoms are provided.

COMMENTS

Background

Schizophrenia affects up to 1% of the population. Understanding the neural substrates of this heterogeneous disorder involves a precise study of the brain, in terms of anatomy and function.

Research frontiers

To study the specific schizophrenia phenotypes is one of the most significant is-

sues in psychiatry. The use of a multimodal (structural and functional) approach will help to develop new phenomenological models of anatomical and functional abnormalities in schizophrenic patients suffering from auditory hallucinations.

Innovations and breakthroughs

Several studies have reported both structural and functional alterations when evaluating patients with schizophrenia. Nevertheless, the clinical heterogeneity of the samples is associated with large variability in the results. This is the first study that uses a multimodal methodology to evaluate areas where functional and structural alterations coexist in a high specific sample of patients with schizophrenia and auditory hallucinations.

Applications

The use of the proposed methodology will be useful to obtain concordance maps showing areas with functional abnormalities and focal brain reductions in psychiatric and neurodegenerative diseases.

Terminology

Semiautomatic morphometric methods are used to detect subtle differences in terms of gray and white matter between groups. The functional evaluation of a patient can detect activated areas that strongly correlate with the stimulation paradigm.

Peer review

The authors present a validation study of a multimodal methodology (structural and functional MR) through the identification of key areas for the biological underpinnings of auditory hallucinations. The importance of this research is the potentiality of this approach to identify key areas for particular phenotypes. The authors combine this multimodal technique with an extreme phenotype approach, which is fairly innovative in psychiatry. The paper is well-written and readable with no ethical objections. The different sections are clearly differentiated.

REFERENCES

- 1 Honea R, Crow TJ, Passingham D, Mackay CE. Regional deficits in brain volume in schizophrenia: a meta-analysis of voxel-based morphometry studies. *Am J Psychiatry* 2005; **162**: 2233-2245
- 2 Sun J, Maller JJ, Guo L, Fitzgerald PB. Superior temporal gyrus volume change in schizophrenia: a review on region of interest volumetric studies. *Brain Res Rev* 2009; **61**: 14-32
- 3 García-Martí G, Aguilar EJ, Lull JJ, Martí-Bonmati L, Escartí MJ, Manjón JV, Moratal D, Robles M, Sanjuán J. Schizophrenia with auditory hallucinations: a voxel-based morphometry study. *Prog Neuropsychopharmacol Biol Psychiatry* 2008; **32**: 72-80
- 4 Ashburner J, Friston KJ. Voxel-based morphometry--the methods. *Neuroimage* 2000; **11**: 805-821
- 5 Kawasaki Y, Suzuki M, Nohara S, Hagino H, Takahashi T, Matsui M, Yamashita I, Chitnis XA, McGuire PK, Seto H, Kurachi M. Structural brain differences in patients with schizophrenia and schizotypal disorder demonstrated by voxel-based morphometry. *Eur Arch Psychiatry Clin Neurosci* 2004; **254**: 406-414
- 6 Job DE, Whalley HC, McConnell S, Glabus M, Johnstone EC, Lawrie SM. Structural gray matter differences between first-episode schizophrenics and normal controls using voxel-based morphometry. *Neuroimage* 2002; **17**: 880-889
- 7 Kubicki M, Shenton ME, Salisbury DF, Hirayasu Y, Kasai K, Kikinis R, Jolesz FA, McCarley RW. Voxel-based morphometric analysis of gray matter in first episode schizophrenia. *Neuroimage* 2002; **17**: 1711-1719
- 8 Fornito A, Yücel M, Patti J, Wood SJ, Pantelis C. Mapping grey matter reductions in schizophrenia: an anatomical likelihood estimation analysis of voxel-based morphometry studies. *Schizophr Res* 2009; **108**: 104-113
- 9 Jardri R, Pouchet A, Pins D, Thomas P. Cortical activations during auditory verbal hallucinations in schizophrenia: a coordinate-based meta-analysis. *Am J Psychiatry* 2011; **168**: 73-81
- 10 Allen P, Larøi F, McGuire PK, Aleman A. The hallucinating

- brain: a review of structural and functional neuroimaging studies of hallucinations. *Neurosci Biobehav Rev* 2008; **32**: 175-191
- 11 **Calhoun VD**, Adali T, Giuliani NR, Pekar JJ, Kiehl KA, Pearlson GD. Method for multimodal analysis of independent source differences in schizophrenia: combining gray matter structural and auditory oddball functional data. *Hum Brain Mapp* 2006; **27**: 47-62
- 12 **Tomasi D**, Volkow ND. Functional connectivity hubs in the human brain. *Neuroimage* 2011; **57**: 908-917
- 13 **Lui S**, Deng W, Huang X, Jiang L, Ma X, Chen H, Zhang T, Li X, Li D, Zou L, Tang H, Zhou XJ, Mechelli A, Collier DA, Sweeney JA, Li T, Gong Q. Association of cerebral deficits with clinical symptoms in antipsychotic-naïve first-episode schizophrenia: an optimized voxel-based morphometry and resting state functional connectivity study. *Am J Psychiatry* 2009; **166**: 196-205
- 14 **Horn H**, Federspiel A, Wirth M, Müller TJ, Wiest R, Wang JJ, Strik W. Structural and metabolic changes in language areas linked to formal thought disorder. *Br J Psychiatry* 2009; **194**: 130-138
- 15 **Martí-Bonmatí L**, Lull JJ, García-Martí G, Aguilar EJ, Moratal-Pérez D, Poyatos C, Robles M, Sanjuán J. Chronic auditory hallucinations in schizophrenic patients: MR analysis of the coincidence between functional and morphologic abnormalities. *Radiology* 2007; **244**: 549-556
- 16 **Oldfield RC**. The assessment and analysis of handedness: the Edinburgh inventory. *Neuropsychologia* 1971; **9**: 97-113
- 17 **Overall JE**, Gorham DR. The brief psychiatric rating scale. *Psychol Rep* 1962; **10**: 799-812
- 18 **Haddock G**, McCarron J, Tarrier N, Faragher EB. Scales to measure dimensions of hallucinations and delusions: the psychotic symptom rating scales (PSYRATS). *Psychol Med* 1999; **29**: 879-889
- 19 **Sanjuan J**, Lull JJ, Aguilar EJ, Martí-Bonmatí L, Moratal D, Gonzalez JC, Robles M, Keshavan MS. Emotional words induce enhanced brain activity in schizophrenic patients with auditory hallucinations. *Psychiatry Res* 2007; **154**: 21-29
- 20 **Phillips ML**, Bullmore ET, Howard R, Woodruff PW, Wright IC, Williams SC, Simmons A, Andrew C, Brammer M, David AS. Investigation of facial recognition memory and happy and sad facial expression perception: an fMRI study. *Psychiatry Res* 1998; **83**: 127-138
- 21 **Pantelis C**, Yücel M, Wood SJ, Velakoulis D, Sun D, Berger G, Stuart GW, Yung A, Phillips L, McGorry PD. Structural brain imaging evidence for multiple pathological processes at different stages of brain development in schizophrenia. *Schizophr Bull* 2005; **31**: 672-696
- 22 **Rajarethinam R**, Sahni S, Rosenberg DR, Keshavan MS. Reduced superior temporal gyrus volume in young offspring of patients with schizophrenia. *Am J Psychiatry* 2004; **161**: 1121-1124
- 23 **Goldstein KE**, Hazlett EA, New AS, Haznedar MM, Newmark RE, Zelmanova Y, Passarelli V, Weinstein SR, Canfield EL, Meyerson DA, Tang CY, Buchsbaum MS, Siever LJ. Smaller superior temporal gyrus volume specificity in schizotypal personality disorder. *Schizophr Res* 2009; **112**: 14-23
- 24 **Takahashi T**, Wood SJ, Yung AR, Soulsby B, McGorry PD, Suzuki M, Kawasaki Y, Phillips LJ, Velakoulis D, Pantelis C. Progressive gray matter reduction of the superior temporal gyrus during transition to psychosis. *Arch Gen Psychiatry* 2009; **66**: 366-376
- 25 **Thirion B**, Pinel P, Mériaux S, Roche A, Dehaene S, Poline JB. Analysis of a large fMRI cohort: Statistical and methodological issues for group analyses. *Neuroimage* 2007; **35**: 105-120
- 26 **Horga G**, Parellada E, Lomeña F, Fernández-Egea E, Mané A, Font M, Falcón C, Konova AB, Pavia J, Ros D, Bernardo M. Differential brain glucose metabolic patterns in antipsychotic-naïve first-episode schizophrenia with and without auditory verbal hallucinations. *J Psychiatry Neurosci* 2011; **36**: 312-321

S- Editor Cheng JX L- Editor O'Neill M E- Editor Zheng XM

Virtual nonenhanced abdominal dual-energy MDCT: Analysis of image characteristics

Jacob Sosna, Shmuel Mahgerefteh, Liran Goshen, Galit Kafri, Galit Aviram, Arye Blachar

Jacob Sosna, Shmuel Mahgerefteh, Department of Radiology, Hadassah-Hebrew University Medical Center, Jerusalem 91120, Israel

Jacob Sosna, Department of Radiology, Beth Israel Deaconess Medical Center, Boston, MA 02215, United States

Liran Goshen, Galit Kafri, Philips Healthcare, Haifa 31004, Israel
 Galit Aviram, Arye Blachar, Department of Radiology, Tel Aviv Sourasky Medical Center, Sackler School of Medicine, Tel Aviv University, Tel Aviv 64239, Israel

Author contributions: Sosna J guaranteed the integrity for this entire study; Sosna J and Blachar A contributed to study concepts and study design; Mahgerefteh S, Goshen L and Kafri G analysed data analysis; Sosna J, Aviram G, Mahgerefteh S and Blachar A drafted manuscript; all authors approved final revision.

Correspondence to: **Jacob Sosna, MD**, Department of Radiology, Hadassah Hebrew University Medical Center, POB 12000, Jerusalem 91120, Israel. jacobs@hadassah.org.il

Telephone: +972-2-6776901 Fax: +972-2-6776901

Received: October 28, 2011 Revised: February 20, 2012

Accepted: February 27, 2012

Published online: April 28, 2012

Abstract

AIM: To evaluate abdominal and pelvic image characteristics and artifacts on virtual nonenhanced (VNE) images generated from contrast-enhanced dual-energy multidetector computed tomography (MDCT) studies.

METHODS: Hadassah-Hebrew University Medical Institutional Review Board approval was obtained; 22 patients underwent clinically-indicated abdominal and pelvic single-source dual-energy MDCT (Philips Healthcare, Cleveland, OH, USA), pre- and post-IV administration of Omnipaque 300 contrast (100 cc). Various solid and vascular structures were evaluated. VNE images were generated from the portal contrast-enhanced phase using probabilistic separation. Contrast-enhanced-, regular nonenhanced (RNE)-, and VNE images were evaluated with a total of 1494 density measurements. The ratio of iodine contrast deletion was calculated. Visualization of calcifications, urinary tract stones, and image artifacts in VNE images were assessed.

RESULTS: VNE images were successfully generated in all patients. Significant portal-phase iodine contrast deletion was seen in the kidney (61.7%), adrenal gland (55.3%), iliac artery (55.0%), aorta (51.6%), and spleen (34.5%). Contrast deletion was also significant in the right atrium (RA) (51.5%) and portal vein (39.3%), but insignificant in the iliac vein and inferior vena cava (IVC). Average post contrast-to-VNE HU differences were significant ($P < 0.05$) in the: RA -135.3 (SD 121.8), aorta -114.1 (SD 48.5), iliac artery -104.6 (SD 53.7), kidney -30.3 (SD 34.9), spleen -9.2 (SD 8.8), and portal vein -7.7 (SD 13.2). Average VNE-to-RNE HU differences were significant in all organs but the prostate and subcutaneous fat: aorta 38.0 (SD 9.3), RA 37.8 (SD 16.1), portal vein 21.8 (SD 12.0), IVC 12.2 (SD 11.6), muscle 3.3 (SD 4.9), liver 5.7 (SD 6.4), spleen 22.3 (SD 9.8), kidney 40.5 (SD 6.8), and adrenal 20.7 (SD 13.5). On VNE images, 196/213 calcifications (92%) and 5/6 renal stones (84%) were visualized. Lytic-like artifacts in the vertebral bodies were seen in all studies.

CONCLUSION: Iodine deletion in VNE images is most significant in arteries, and less significant in solid organs and veins. Most vascular and intra-abdominal organ calcifications are preserved.

© 2012 Baishideng. All rights reserved.

Key words: Abdominal computed tomography; Dual-energy computed tomography; Pelvic computed tomography; Virtual nonenhanced computed tomography

Peer reviewer: Filippo Cademartiri, MD, PhD, Departmento of Radiology - c/o Piastra Tecnica - Piano 0, Azienda Ospedaliero-Universitaria di Parma, Via Gramsci, 14 - 43100 Parma, Italy

Sosna J, Mahgerefteh S, Goshen L, Kafri G, Aviram G, Blachar A. Virtual nonenhanced abdominal dual-energy MDCT: Analysis of image characteristics. *World J Radiol* 2012; 4(4): 167-173 Available from: URL: <http://www.wjgnet.com/1949-8470/full/v4/i4/167.htm> DOI: <http://dx.doi.org/10.4329/wjr.v4.i4.167>

INTRODUCTION

The past years have been characterized by tremendous progress in computed tomography (CT) technology. With the introduction of multidetector (MD) scanners that produce very high quality images, CT use has increased markedly. Recently, MDCT and dual-energy imaging capabilities were combined. Dual-energy techniques are designed to capture information from varying responses of materials with a range of Compton and photoelectric effects to X-rays at different energies^[1].

Dual-energy acquisition enables reconstruction of virtual nonenhanced (VNE) images, wherein the iodine content of contrast-enhanced CT images is subtracted using image post-processing techniques^[2]. VNE images have been shown to be useful in various clinical settings, ranging from the detection of masses and stones to evaluation of vascular disease^[3]. The virtual deletion of iodine is appealing, as it may obviate the need for the nonenhanced imaging phase in multiphase studies; thus, VNE has the potential to significantly reduce X-ray exposure for patients and shorten CT study times^[3].

To the best of our knowledge, a comparative evaluation of VNE at the various abdominal and pelvic organs has never been carried out. We aimed to systematically evaluate VNE images generated from a dual-energy multi-detector CT using probabilistic separation and a VNE algorithm, and to assess iodine contrast deletion, depiction of calcifications, and extent of image artifacts in abdominal and pelvic scans.

MATERIALS AND METHODS

Authors who are not employees of Philips Healthcare (JS, SM, GA, AB) had continuous control of all information and research data in this study, with JS acting as the guarantor of integrity for the entire study.

The dual-energy CT system

The study was performed on a prototype single-source dual-energy MDCT available for research purposes (Philips Healthcare, Cleveland, OH, USA). The scanner tube was conventional, without modulation capabilities. Dual-energy was based on dual detector capability, with the upper layer primarily absorbing the lower X-ray energy spectrum, and the lower detector layer absorbing the remainder of the spectrum, mainly in the higher energy range^[4]. Each layer has 32 detector rows and a 50 cm full field-of-view. Data from each layer, corresponding to lower- and higher energies, are independently reconstructed. In addition, a combined standard CT image is reconstructed from weighted raw signals of the two layers. As the evaluated scanner is based on a single-source dual-energy layer, a single kVp is provided, with separation of the low- and high-energy images at the detector level.

Study population

Hadassah-Hebrew University Medical Institutional Re-

view Board approval was obtained. All participants had clinical indications for abdominal and pelvic CT, and signed an informed consent. The consent form included information on the research scanner and a statement that radiological interpretation would be based solely on the conventional averaged CT image. Twenty-two consecutive patients referred for clinically indicated CT studies were included in the study, including eight women and 14 men ranging in age from 38-71 years (mean 60 years, SD 10 years). CT studies were performed using collimation of 32×0.625 mm, FOV of 50 cm, slice thickness and increment of 1-3 mm, 140 kVp, 250-300 mAs, and kernel B. Air calibration was performed before each scan.

All patients were scanned before and after intravenous administration of 100 cc of iohexol (Omnipaque 300, Amersham Health, Princeton NJ, USA), injected at a rate of 3-4 cc/s using a mechanical injector (Medrad, Warrendale, PA, USA). Scans were performed within 60 s from initiation of injection.

Solid organs evaluated were subcutaneous fat, erector spinae muscle, spleen, liver, adrenal gland, kidney, and prostate. Vascular structures evaluated were the right atrium (RA), aorta, inferior vena cava (IVC), portal vein, common iliac artery and vein, external iliac artery and vein, and common femoral artery and vein.

VNE generation technique

The analysis consisted of two steps^[2]: (1) estimation of material response vectors; and (2) iodine-calcium separation. The first step was accomplished using an automatic algorithm that estimated the material response vectors of iodine, calcium, and soft tissue on the dual-energy map. This algorithm was applied for each slice in the study to eliminate beam-hardening effects that may impact on the orientation of material response vectors. The algorithm presented the distribution of voxel distance from material response vectors in the energy map as a probability model to estimate combinations of iodine, calcium, and soft tissue voxels.

The second step was implemented using a separation algorithm to estimate the probability for each voxel to be either iodine or calcium. The algorithm incorporated the estimated response vectors to approximate prior probabilities that iodine or calcium were depicted in each region of the volume.

Systematic image analysis

CT scans were loaded on a Kodak PACS viewing station (Carestream Health, Rochester NY, USA). Contrast enhanced-, regular nonenhanced (RNE)-, and VNE images were evaluated separately using the combined weighted CT for the RNE and contrast enhanced studies. Multiple attenuation measurements were performed on various organs. Measurements were performed by a research fellow with 12 mo experience in dual-energy CT (SM) using regions-of-interest (ROI) that were identical in size and location on all VNE and RNE images. ROI measurements of organs were obtained with care to avoid calcifi-

cations and vessels within the organs, as well as obvious masses. ROI size varied from 0.7 to 2.5 cm². Standard deviations were calculated for each measurement. A total of 1494 density measurements were performed, including 22 measurements in each female patient, and 23 for each male patient, including the prostate.

Densities were measured in the RA and in a number of vessels, including the aorta, IVC, main portal vein, right common iliac and right external iliac artery and vein, and right common femoral artery and vein. Multiple intra-abdominal organ densities were measured, including the right hepatic lobe (at the level of the right portal vein), left hepatic lobe (at the level of the left portal vein), spleen (at the level of the splenic hilum), prostate, left adrenal, right kidney (cortex, at a subcapsular location), left erector spinae muscle, and right posterior subcutaneous fat.

Evaluation of virtual contrast deletion: To determine the difference in attenuation between VNE- and post contrast images, we subtracted attenuation values measured on VNE images from values on images showing contrast enhancement. To determine the difference in attenuation between VNE- and RNE images, we subtracted attenuation values measured on VNE images from values on the RNE images. We calculated the average difference for each measured area. The ratio of these two subtractions was then calculated to generate the percentage of contrast deletion, defined as (contrast-VNE)/(contrast-NE).

Calcifications and urinary stones: The presence of organ calcifications and urinary stones was evaluated in consensus by two experienced abdominal radiologists (AB and JS) with 14 and 12 years of experience, respectively. Each organ calcification identified in an RNE image was evaluated on the VNE images as still visible or completely deleted in comparison to the RNE study. Since there is no accurate system enabling precise evaluation of the change in aortic calcifications on VNC images, we evaluated these calcifications subjectively. The most heavily calcified 5 cm section of each vessel was chosen. Calcifications seen on RNE and VNE images were measured, including calcifications in arterial walls, as well as intraluminal densities of arteries and veins. Urinary stones were assessed separately.

Artifacts: The presence and nature of artifacts on VNE images were evaluated to identify focal changes in VNE image quality that were not seen on the RNE image and that were not anatomical or pathological.

Statistical analysis

Descriptive statistics were used where appropriate. The sign test was used to compare the differences in attenuation between contrast enhanced-, RNE-, and VNE images to test the hypothesis that there is no difference between RNE and VNE in a situation when paired samples could be drawn. All analyses were performed with SAS

Table 1 Subtraction of the average HU measurements of organs evaluated: Enhanced computed tomography minus virtual nonenhanced images

Organ	mean \pm SD	P value	Percent deletion
Adrenal gland	1.8 \pm 6.9	< 0.0001	55.3
Kidney	30.279 \pm 34.91	< 0.0001	61.7
Spleen	9.202 \pm 8.79	< 0.0001	34.5
Liver	3.619 \pm 9.21	0.490	10.2
Subcutaneous fat	0.330 \pm 2.52	0.8318	2.3
Prostate	-0.183 \pm 1.63	1.0000	13.3
Erector spinae muscle	-0.403 \pm 2.64	0.5235	7.7
Right atrium	135.4 \pm 16.0	< 0.0001	51.5
Portal vein	7.6 \pm 2.3	0.0015	39.3
Inferior vena cava	1.7 \pm 2.0	0.5235	26.6
Aorta	114.1 \pm 1.2	< 0.0001	51.6
Iliac vein	3.616 \pm 3.04	0.0625	25.3
Iliac artery	104.64 \pm 53.66	< 0.0001	55.0

statistical analysis software (version 9.1, SAS Institute, Cary NC, USA). $P < 0.05$ was considered significant.

RESULTS

Contrast deletion

VNE images were generated successfully in all 22 patients, using probabilistic separation. Evaluation of the RA and multiple intra-abdominal organ and vascular densities showed that contrast deletion was indeed substantial (Table 1). Contrast material deletion was significant at 51.6% and 55.0% in the aorta and iliac artery, respectively. Among the veins, only the portal vein showed statistically significant deletion, at 39.3%; deletions at the IVC and iliac vein were both insignificant at around 25%, however, the RA showed significant deletion at 51.5%. Intra-abdominal organs demonstrating significant contrast deletion were spleen (34.5%), adrenal (55.3%) and the kidney at the portal phase (61.7%) (Figure 1). Deletion in the prostate was about 13% and insignificant. Deletion was heterogeneous and insignificant in the liver, averaging about 10% overall. Subcutaneous tissues and muscles showed the least contrast enhancement, as well as the lowest degree of contrast deletion.

The differences in density between RNE and VNE are shown in Table 2. These differences were statistically significant for all organs but the iliac vein, prostate, erector spinae muscle, and subcutaneous fat. Among solid intra-abdominal organs, the mean differences ranged between 20-40 HU for the kidney, adrenal and spleen ($P < 0.001$) and did not exceed 6 HU for the liver ($P < 0.01$). For vessels, deletion ranged from 8.3 HU for the iliac vein ($P = 0.02$) to about 38 HU for the RA, aorta and iliac artery ($P < 0.0001$).

Organ and vascular calcifications

Evaluation of the arteries on RNE studies revealed 213 calcifications, of which 196 (92%) were visualized on the VNE images (Figure 2). There were six renal stones ranging in size from 1-8 mm. Only one renal stone, 2 mm in

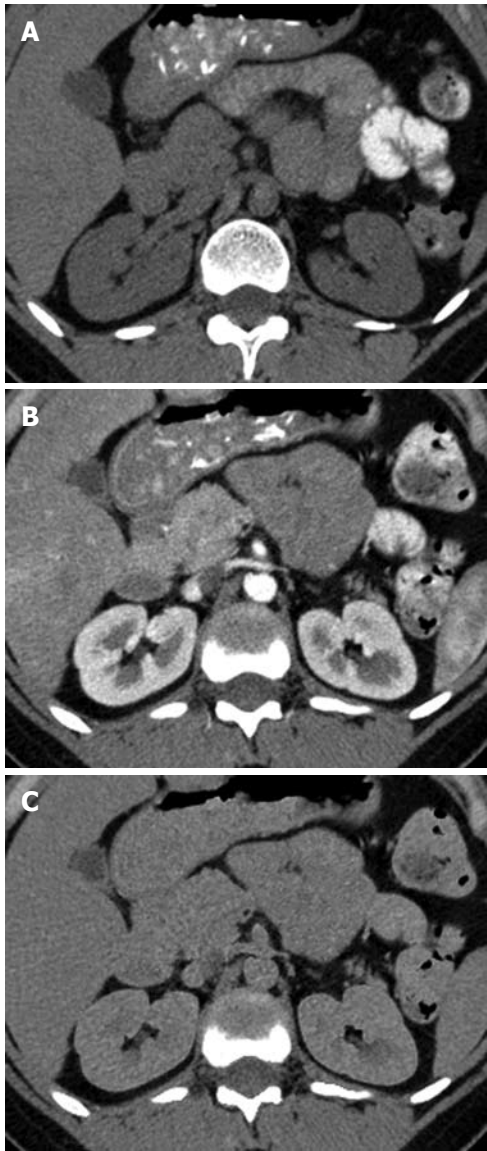


Figure 1 A 52-year-old female with the kidney contrast deletion. A, B: The regular nonenhanced (A) and contrast-enhanced (B) images demonstrate kidneys with normal appearance; C: Virtual nonenhanced shows substantial deletion of contrast from the kidney parenchyma.

Table 2 Average HU differences in densities of organs evaluated on virtual nonenhanced minus regular nonenhanced images		
Organ	mean \pm SD	P value
Adrenal gland	20.7 \pm 13.5	< 0.0001
Kidney	40.5 \pm 6.8	< 0.0001
Spleen	22.3 \pm 9.8	< 0.0001
Liver	5.8 \pm 6.9	0.0072
Subcutaneous fat	-0.3 \pm 4.54	1.0000
Prostate	4.3 \pm 6.6	0.5000
Erector spinae muscle	3.3 \pm 4.9	0.0169
Right atrium	37.8 \pm 16.1	< 0.0001
Portal vein	21.8 \pm 12.0	0.0002
Inferior vena cava	12.2 \pm 11.6	< 0.0001
Aorta	38.0 \pm 9.3	< 0.0001
Iliac vein	8.3 \pm 7.9	0.0225
Iliac artery	38.4 \pm 15.0	< 0.0001

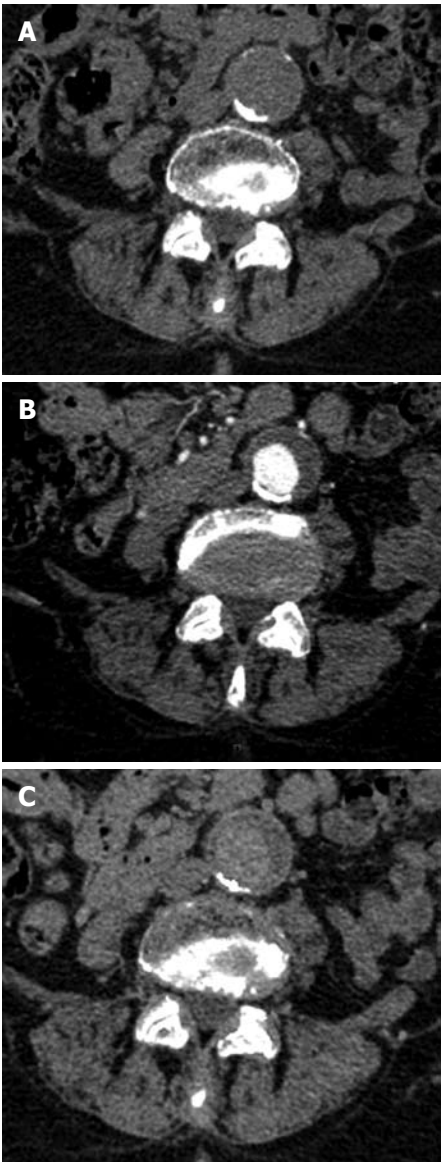


Figure 2 A 60-year-old male with an abdominal aortic aneurysm. A: Regular nonenhanced image demonstrates a curved calcification in the posterior border of the aneurysm with some smaller calcifications in the anterior border; B: The contrast enhanced image shows opacification of the lumen; C: Virtual non-enhanced shows preserved posterior calcifications with deletion of the smaller anterior calcifications.

diameter, was deleted on VNE images; other stones were visible and only partially deleted (Figure 3).

Artifacts

Artifacts were seen in all VNE studies. In the vertebral bodies, they were seen as lytic-like lesions. These were easily identified as artifacts and were not expected to cause the VNE studies to be non-diagnostic (Figure 4).

DISCUSSION

Before the use of VNE imaging becomes widespread, a systematic comparative evaluation of the characteristics of iodine deletion and artifacts at various abdominal or-

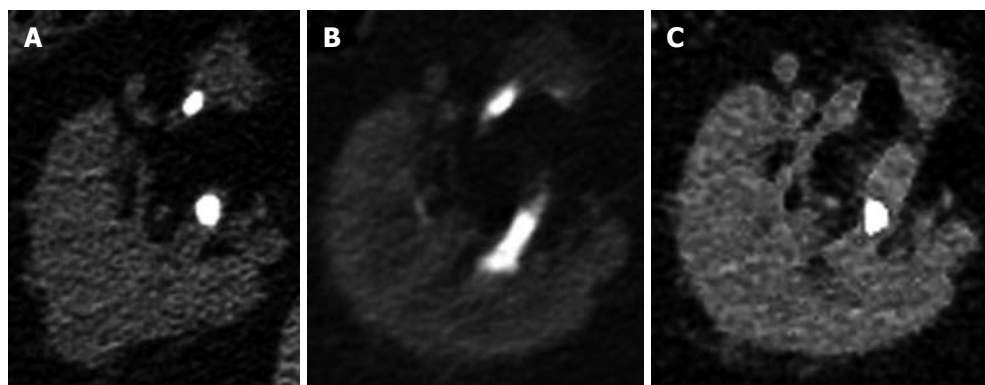


Figure 3 Regular nonenhanced image (A) demonstrates two stones in the right kidney of a 64-year-old male. B: In the contrast-enhanced image, contrast excretion into the collecting system is inhibited by the stones, which are obscured; C: In the virtual nonenhanced image, the posterior stone is maintained while the anterior stone is deleted.

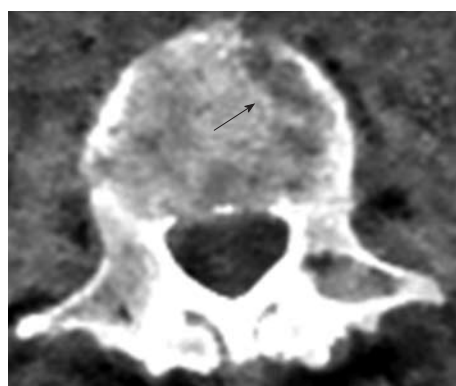


Figure 4 Virtual nonenhanced image of this 58-year-old female shows a lytic-like artifact in the vertebral body. The "lesion" was easily identified as an artifact.

gans is important to assess the clinical potential of these studies for specific applications. Our study demonstrates the technical feasibility and imaging characteristics of VNE images. In this series, iodine deletion reached as high as 50%-60% in arterial vessels, RA, adrenal and kidney. It was less pronounced in veins and in the remaining abdominal organs. The majority of vascular calcifications and renal stones were preserved. Specific, easily recognized artifacts could be attributed to this technique.

The importance of noncontrast imaging as a part of CT protocols has been shown previously^[5]. At CT angiography, a noncontrast study is usually obtained first to identify high attenuation in the aortic wall, which is consistent with intramural hematoma and may indicate early or impending rupture. Noncontrast images are also useful in evaluating and defining high attenuating structures such as calcium or metal that may be confused with enhancement on post-contrast images, for example in patients evaluated after abdominal aortic aneurysm repair.

Noncontrast images of the liver are used to demonstrate calcifications and fibrosis, and to provide important information in the characterization of hepatic masses^[6]. In the kidneys, noncontrast images are used to detect the presence of calcifications and their degree of enhance-

ment^[7]. Imaging and characterization of adrenal masses also currently relies on noncontrast image acquisition^[8]. Multiphasic imaging of the liver, pancreas, kidney and thorax has therefore become standard practice^[9].

Recently, it has been shown that dual-energy dual-source CT scans performed during the delayed phase, with reconstruction of VNE images, enables detection of endoleaks after endovascular abdominal aortic aneurysm repair with high accuracy and a considerably lower patient radiation dose^[10-12]. Chow *et al.*^[11] have shown that 94% of VNE images are diagnostic; similarly, in our study, all images were diagnostic. The Sommer group reported at least minimal subtraction of calcifications in 70% of their VNE images^[11], whereas we found only 8% subtraction. This difference might be attributed to differences in the dual-energy algorithms used for iodine deletion from the CT images.

VNE imaging has already been used in the characterization of pulmonary nodules. Chae *et al.*^[13] reported detection of 85.0% of calcifications (17 of 20) in solitary pulmonary nodules and 97.8% of calcifications (44 of 45) in the lymph nodes on VNE images, although apparent size was smaller on VNE- compared with non-enhanced weighted average images. These results are in accordance with our findings in relation to the preservation of calcifications.

Dual-energy contrast-enhanced CT acquisition with VNE reformation has shown sensitivity, specificity, and positive- and negative predictive values of 83%, 100%, 100%, and 88%, respectively, for the detection of urinary stone disease^[14]. In our study, most urinary stones were also preserved. This may be beneficial in CT urography studies, since it may enable stone detection with omission of the nonenhanced phase.

Graser *et al.*^[15] have shown the reliability of VNE imaging for assessment of renal masses with similar density on VNE and RNE images. In our study, however, there were differences in density on VNE and RNE images of the kidney. This may be attributable to differences in timing of contrast injection, and the use of different dual-energy scanning techniques; Graser *et al.*^[15] used a

dual-source, while we used a dual-detector scanner in our study. On the other hand, differences in liver density on VNE and RNE images were minimal in our study; thus VNE may be performed in the future to avoid the need for a nonenhanced phase in multi-phasic liver studies. Zhang *et al*^[16] showed that arterial- and portovenous-phase-derived VNE images can detect 91% and 81% of focal liver lesions, respectively.

The ability of DECT-derived VNE images to depict urinary stones in an iodine solution was tested in a phantom model^[17]. Stone visibility rates varied with changes in iodine concentration and kVp. The study showed that VNE is capable of depicting urinary stones in iodine solutions of a diverse range of concentrations in a phantom study. With regard to urinary stones, our *in vivo* study supports the findings obtained in a phantom model from this earlier study.

Since contrast deletion occurred mainly from arteries in our study, it would seem more logical to perform VNE algorithms at the arterial phase rather than the venous phase, when there is also less iodine in the parenchyma. Compared to the portal venous phase, the hepatic arterial phase of dual-energy VNE was shown to provide better image quality and may be more diagnostic^[16,18]. The reason for the improved contrast deletion from arteries is probably related to the higher iodine concentration within vessels with higher HU values, and more specifically within the pixels with iodine content. Further phantom and clinical studies are needed to assess differences in VNE images derived from the arterial and venous phases, as well as variation due to differences in deletion algorithms.

VNE has the potential to significantly decrease patient exposure to ionizing radiation, an issue of increasing concern. The National Council on Radiation Protection and Measurements estimates that the annual medical radiation dose in the general population has increased by a factor of nearly six since the early 1980s^[19,20]. The number of CT scans performed in the US increased from 18.3 million in 1993 to 67 million in 2006^[20]. It is estimated that CT scans constituted only 17% of all medical radiation procedures, but contributed about 49% of the collective dose in 2006^[20].

In the past decade, both the clinical utility and the availability of CT have increased significantly, resulting in a dramatic increase in CT utilization^[21]. It is thus important that patient radiation exposure is carefully considered, particularly in the case of multiphasic, repeated, or multiple examinations^[22-25]. Further study of the clinical role for VNE reformation would thus appear to be a high priority. Depending on the setting in which it is implicated, VNE has the potential to reduce radiation dose by as much as 60% in a single study^[3].

There are some limitations to our study. The population was relatively small. We have also evaluated only one type of dual-energy scanner. Other techniques for dual-energy CT imaging may yield different levels of iodine contrast deletion; acquisition techniques and reformation

algorithms are unique for each commercially available system. It should also be noted that our RNE images were weighted averages of dual-energy datasets, derived from DECT technology with the unique capability for simultaneous dual- and single-energy image construction following a single scan. In theory, our RNE images should represent true single-scan data, however, it is possible that comparison of our VNE images to RNE images acquired at conventional MDCT might yield different results than those described here.

In conclusion, VNE images can be obtained with dual energy CT, with iodine mainly deleted from arteries and solid organs rich in blood supply such as the kidneys, adrenal gland, and spleen. A lesser degree of iodine deletion is seen in other abdominal solid organs such as the liver, as well as in the veins. Most vascular and intra-abdominal organ calcifications are preserved. VNE technology may potentially obviate the need for RNE image acquisition when multi-phase studies are needed, thereby reducing the overall radiation burden, but this must be investigated further in abdominal organs.

ACKNOWLEDGMENTS

Jacob Sosna, Professor is the principle investigator under a research agreement with Philips HealthCare. Dr. Liran Goshen and Dr. Galit Kafri are employees of Philips HealthCare. The other authors have no conflicts of interest to disclose.

The authors wish to thank Shifra Fraifeld, MBA, a Research Associate in the Department of Radiology at Hadassah Medical Center, for her contribution to database development and management, and her editorial assistance in the preparation of this manuscript.

COMMENTS

Background

Dual-energy acquisition enables reconstruction of virtual nonenhanced (VNE) images, wherein the iodine content of contrast-enhanced computed tomography (CT) images is subtracted using image post-processing techniques. VNE images have been shown to be useful in various clinical settings, ranging from detection of masses and stones to evaluation of vascular disease. The virtual deletion of iodine is appealing, as it may obviate the need for the nonenhanced imaging phase in multiphase studies; thus, VNE has the potential to significantly reduce X-ray exposure for patients and shorten CT study times.

Research frontiers

The paper aimed to systematically evaluate VNE images generated from a dual-energy multidetector CT (MDCT) using probabilistic separation and a VNE algorithm, and to assess iodine contrast deletion, depiction of calcifications, and extent of image artifacts in abdominal and pelvic scans.

Innovations and breakthroughs

The study demonstrates the technical feasibility and imaging characteristics of VNE images. In this series, iodine deletion reached as high as 50%-60% in arterial vessels, right atrium, adrenal and kidney. It was less pronounced in veins and in the remaining abdominal organs. The majority of vascular calcifications and renal stones were preserved. Specific artifacts could be attributed to this technique, and these were easily recognized as such. All images were diagnostic, with only 8% of calcifications being subtracted. In previous series, findings in renal parenchyma showed similar density on VNE and regular nonenhanced (RNE) images. In the study, however, there were differences in density on VNE and RNE images of the kidney. This may be attributable to differences in timing

of contrast injection, and the use of different dual-energy scanning techniques. On the other hand, differences in liver density on VNE and RNE images were minimal in the study; thus VNE may be performed in the future to avoid the need for a nonenhanced phase in multi-phasic liver studies. Since contrast deletion occurred mainly from arteries in our study, it would seem more logical to perform VNE algorithms at the arterial phase rather than the venous phase, when there is also less iodine in the parenchyma. Compared to the portal venous phase, the hepatic arterial phase of dual-energy VNE has been previously shown to provide better image quality and may be more diagnostic.

Applications

VNE images can be obtained with dual-energy CT, with iodine mainly deleted from arteries and solid organs rich in blood supply such as the kidney, adrenal gland, and spleen. A lesser degree of iodine deletion is seen in other abdominal solid organs such as the liver, as well as in the veins. Most vascular and intra-abdominal organ calcifications are preserved. VNE technology may potentially obviate the need for RNE image acquisition in abdominal imaging when multi-phase studies are needed, thereby reducing the overall radiation burden.

Terminology

Dual-energy CT: An emerging CT imaging technique in which two datasets are obtained at a single scan, corresponding to two distinct energy spectra; these distinct datasets are then analyzed to reveal material-specific information. VNE image: An image derived from postprocessing of data acquired at dual-energy CT, in which iodinated contrast material is digitally deleted from the original contrast-enhanced image.

Peer review

This study represents an important step in the advancement of dual-energy CT in general and VNE imaging in particular. While other VNE studies have focused on specific organs or disease entities, this study provides the first comprehensive demonstration of the clinical feasibility and utility of VNE imaging within the abdomen as a whole. The results presented here support the advancement of this unique imaging technique in abdominal imaging, whereby radiation exposure to patients can be dramatically reduced. Further studies should compare the performances of the various dual-energy data acquisition systems and VNE algorithms in the abdomen.

REFERENCES

- Avrin DE, Macovski A, Zatz LE. Clinical application of Compton and photo-electric reconstruction in computed tomography: preliminary results. *Invest Radiol* 1978; **13**: 217-222
- Goshen L, Sosna J, Carmi R, Kafri G, Iancu I, Altman A. An iodine-calcium separation analysis and virtually non-contrasted image generation obtained with single source dual energy MDCT. *IEEE Nucl Sci Symp Conf Rec* 2008; 3868-3870
- Mahgerefteh S, Blachar A, Fraifeld S, Sosna J. Dual-energy derived virtual nonenhanced computed tomography imaging: current status and applications. *Semin Ultrasound CT MR* 2010; **31**: 321-327
- Carmi R, Naveh G, Altman A. Material separation with dual-layer CT. *IEEE Nuclear Sci Symp Conf Rec* 2005; **4**: 1876-1878
- Bhalla S, Menias CO, Heiken JP. CT of acute abdominal aortic disorders. *Radiol Clin North Am* 2003; **41**: 1153-1169
- Federle MP, Blachar A. CT evaluation of the liver: principles and techniques. *Semin Liver Dis* 2001; **21**: 135-145
- Yuh BI, Cohan RH. Different phases of renal enhancement: role in detecting and characterizing renal masses during helical CT. *AJR Am J Roentgenol* 1999; **173**: 747-755
- Korobkin M, Francis IR. Imaging of adrenal masses. *Urol Clin North Am* 1997; **24**: 603-622
- Tatli S, Yucel EK, Lipton MJ. CT and MR imaging of the thoracic aorta: current techniques and clinical applications.

- Radiol Clin North Am* 2004; **42**: 565-585, vi
- Stolzmann P, Frauenfelder T, Pfammatter T, Peter N, Scheffel H, Lachat M, Schmidt B, Marincek B, Alkadhi H, Schertler T. Endoleaks after endovascular abdominal aortic aneurysm repair: detection with dual-energy dual-source CT. *Radiology* 2008; **249**: 682-691
- Chow LC, Kwan SW, Olcott EW, Sommer G. Split-bolus MDCT urography with synchronous nephrographic and excretory phase enhancement. *AJR Am J Roentgenol* 2007; **189**: 314-322
- Chandarana H, Godoy MC, Vlahos I, Graser A, Babb J, Leidecker C, Macari M. Abdominal aorta: evaluation with dual-source dual-energy multidetector CT after endovascular repair of aneurysms--initial observations. *Radiology* 2008; **249**: 692-700
- Chae EJ, Song JW, Seo JB, Krauss B, Jang YM, Song KS. Clinical utility of dual-energy CT in the evaluation of solitary pulmonary nodules: initial experience. *Radiology* 2008; **249**: 671-681
- Scheffel H, Stolzmann P, Frauenfelder T, Schertler T, Desbiolles L, Leschka S, Marincek B, Alkadhi H. Dual-energy contrast-enhanced computed tomography for the detection of urinary stone disease. *Invest Radiol* 2007; **42**: 823-829
- Graser A, Johnson TR, Hecht EM, Becker CR, Leidecker C, Staehler M, Stief CG, Hildebrandt H, Godoy MC, Finn ME, Stepansky F, Reiser MF, Macari M. Dual-energy CT in patients suspected of having renal masses: can virtual nonenhanced images replace true nonenhanced images? *Radiology* 2009; **252**: 433-440
- Zhang LJ, Peng J, Wu SY, Wang ZJ, Wu XS, Zhou CS, Ji XM, Lu GM. Liver virtual non-enhanced CT with dual-source, dual-energy CT: a preliminary study. *Eur Radiol* 2010; **20**: 2257-2264
- Takahashi N, Hartman RP, Vrtiska TJ, Kawashima A, Primak AN, Dzyubak OP, Mandrekar JN, Fletcher JG, McCollough CH. Dual-energy CT iodine-subtraction virtual nonenhanced technique to detect urinary stones in an iodine-filled collecting system: a phantom study. *AJR Am J Roentgenol* 2008; **190**: 1169-1173
- Peng J, Zhang LJ, Wu S, Lu GM. A preliminary study of epigastrium dual energy virtual noncontrast CT of dual source CT. Chicago, IL: Radiological Society of North America, 2009
- National Council on Radiation Protection and Measurements. Ionizing Radiation Exposure of the Population of the United States. Bethesda, MD: National Council on Radiation Protection and Measurements, 2009
- Mettler FA, Thomadsen BR, Bhargavan M, Gilley DB, Gray JE, Lipoti JA, McCrohan J, Yoshizumi TT, Mahesh M. Medical radiation exposure in the U.S. in 2006: preliminary results. *Health Phys* 2008; **95**: 502-507
- Huda W, Vance A. Patient radiation doses from adult and pediatric CT. *AJR Am J Roentgenol* 2007; **188**: 540-546
- Catalano C, Francione M, Ascarelli A, Mangia M, Iacucci I, Passariello R. Optimizing radiation dose and image quality. *Eur Radiol* 2007; **17** Suppl 6: F26-F32
- Fazel R, Krumholz HM, Wang Y, Ross JS, Chen J, Ting HH, Shah ND, Nasir K, Einstein AJ, Nallamothu BK. Exposure to low-dose ionizing radiation from medical imaging procedures. *N Engl J Med* 2009; **361**: 849-857
- Frush DP. Review of radiation issues for computed tomography. *Semin Ultrasound CT MR* 2004; **25**: 17-24
- Valentin J. Managing patient dose in multi-detector computed tomography(MDCT). ICRP Publication 102. *Ann ICRP* 2007; **37**: 1-79, iii

S- Editor Cheng JX L- Editor Webster JR E- Editor Zheng XM

ARFI elastography for the evaluation of diffuse thyroid gland pathology: Preliminary results

Ioan Sporea, Roxana Sirli, Simona Bota, Mihaela Vlad, Alina Popescu, Ioana Zosin

Ioan Sporea, Roxana Sirli, Simona Bota, Alina Popescu, Department of Gastroenterology and Hepatology, University of Medicine and Pharmacy Timisoara, 300736 Timisoara, Romania
 Mihaela Vlad, Ioana Zosin, Department of Endocrinology, University of Medicine and Pharmacy Timisoara, 300736 Timisoara, Romania

Author contributions: Sporea I designed, supervised and revised the manuscript; Sirli R and Bota S wrote the manuscript draft; Bota S, Sirli R, Popescu A, Vlad M and Zosin I performed the research; Bota S analyzed the data; Sporea I, Vlad M, Popescu A and Zosin I revised the manuscript draft; all authors approved the final version of the manuscript.

Correspondence to: Dr. Ioan Sporea, Professor, Department of Gastroenterology and Hepatology, University of Medicine and Pharmacy Timisoara, 13, Snagov Street, 300482 Timisoara, Romania. isporea@umft.ro

Telephone: +40-256-309455 Fax: +40-256-488003

Received: October 7, 2011 Revised: March 17, 2012

Accepted: March 24, 2012

Published online: April 28, 2012

of ARFI in healthy subjects (2 ± 0.40 m/s) was significantly lower than in GD (2.67 ± 0.53 m/s) ($P < 0.0001$) and CAT patients (2.43 ± 0.58 m/s) ($P = 0.0002$), but the differences were not significant between GD vs CAT patients ($P = 0.053$). The optimal cut-off value for the prediction of diffuse thyroid pathology was 2.36 m/s. For this cut-off value, TS had 62.5% sensitivity, 79.5% specificity, 87.6% predictive positive value, 55.5% negative predictive value and 72.7% accuracy for the presence of diffuse thyroid gland pathology (AUROC = 0.804). There were no significant differences between the TS values obtained with linear vs convex probes and when 5 vs 10 measurements were taken in each lobe (median values).

CONCLUSION: ARFI seems to be a useful method for the assessment of diffuse thyroid gland pathology.

© 2012 Baishideng. All rights reserved.

Key words: Acoustic radiation force impulse elastography; Thyroid stiffness; Thyroid pathology

Peer reviewer: AAK Abdel Razek, MD, Professor, Diagnostic Radiology Department, 62 El Nokri St, Meet Hadr, Mansoura Faculty of Medicine, Mansoura 35111, Egypt

Sporea I, Sirli R, Bota S, Vlad M, Popescu A, Zosin I. ARFI elastography for the evaluation of diffuse thyroid gland pathology: Preliminary results. *World J Radiol* 2012; 4(4): 174-178 Available from: URL: <http://www.wjgnet.com/1949-8470/full/v4/i4/174.htm> DOI: <http://dx.doi.org/10.4329/wjr.v4.i4.174>

Abstract

AIM: To assess whether acoustic radiation force impulse (ARFI) elastography can differentiate normal from pathological thyroid parenchyma.

METHODS: We evaluated 136 subjects (mean age 45.8 ± 15.6 years, 106 women and 30 men): 44 (32.3%) without thyroid pathology, 48 (35.3%) with Basedow-Graves' disease (GD), 37 (27.2%) with chronic autoimmune thyroiditis (CAT; diagnosed by specific tests), 4 (2.9%) with diffuse thyroid goiter and 3 (2.2%) cases with thyroid pathology induced by amiodarone. In all patients, 10 elastographic measurements were made in the right thyroid lobe and 10 in the left thyroid lobe, using a 1-4.5 MHz convex probe and a 4-9 MHz linear probe, respectively. Median values were calculated for thyroid stiffness and expressed in meters/second (m/s).

RESULTS: Thyroid stiffness (TS) assessed by means

INTRODUCTION

Clinical evaluation through thyroid palpation is the classical method for assessing this superficial gland. In the last years, elastography has been developed as a new dynamic technique that uses ultrasound waves for the evaluation of tissue stiffness. The principle of ultrasound

elastography is that compression of the examined tissue induces less strain in hard tissues than in soft ones. The ultrasound probe manually or automatically produces an acoustic “push” pulse that generates shear-waves which propagate into the tissue. The propagation speed increases with fibrosis^[1,2].

Recently, several studies have assessed the value of different types of elastography (transient elastography, real time elastography or acoustic radiation force impulse elastography) for the evaluation of liver stiffness in an attempt to replace liver biopsy. Elastographic methods are also used for the assessment of focal lesions or of diffuse pathologies (especially chronic hepatopathies)^[3-8]. Many studies have proved these methods to be valuable, especially for the diagnosis of advanced fibrosis in diffuse liver diseases^[7,9-14].

Considering the analogy of the two parenchymatous organs, liver and thyroid, we tried to assess whether ultrasound-based elastography by means of the acoustic radiation force impulse (ARFI) technique could be useful for the evaluation of thyroid diffuse pathology.

The aim of our paper was to see whether, by using ARFI elastography, we can differentiate a normal thyroid from a pathological one (considering only diffuse thyroid diseases) and secondly, to establish technical parameters for thyroid stiffness (TS) evaluation using ARFI elastography.

MATERIALS AND METHODS

We evaluated 136 subjects (mean age 45.8 ± 15.6 years, 106 women and 30 men): 44 (32.3%) without thyroid pathology, 48 (35.3%) with Basedow-Graves' disease (GD), 37 (27.2%) with chronic autoimmune thyroiditis (CAT), 4 (2.9%) with diffuse thyroid goiter and 3 (2.2%) cases with thyroid pathology induced by amiodarone. All patients agreed to participate in our study which was approved by the local Ethics Committee.

The diagnosis of GD was based on the following criteria: thyrotoxicosis at the beginning confirmed by low thyroid stimulating hormone (TSH), high FT₄ and FT₃; diffuse hypoechoic goiter on ultrasound; and high titers of anti-TSH receptor antibodies. Some of the cases were evaluated by ARFI at the onset of the disease and some while under antithyroid therapy.

The diagnosis of CAT was based on high titers of antithyroid antibodies (anti-TPO and/or antiTg); diffuse hypoechogenicity of the thyroid parenchyma on ultrasound; and normal or low thyroid function. Some of the cases had goiters (Hashimoto type) and some had a normal thyroid volume on ultrasound examination. All amiodarone treated patients developed type II thyrotoxicosis, diagnosed by means of established criteria^[15].

ARFI elastography was performed with a Siemens Acuson S2000™ ultrasound system. In all patients, 10 elastographic measurements were taken in the right thyroid lobe (RTL) and 10 in the left thyroid lobe (LTL) using a convex probe of 1-4.5 MHz. Median values were calcu-

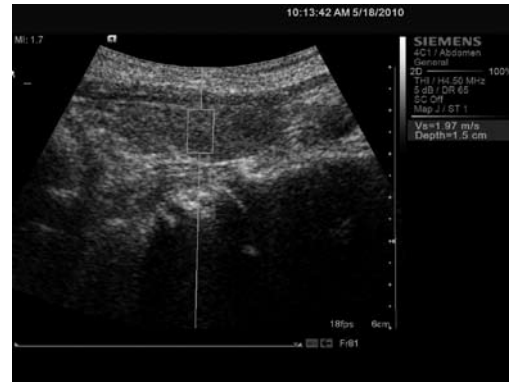


Figure 1 Acoustic radiation force impulse measurement in the left thyroid lobe (with convex probe).

lated and expressed in meters/second (m/s) (Figure 1).

We calculated mean TS values in the RTL and LTL. To see whether the probe type (linear or convex) influences TS measurements, in 45 patients we performed 10 elastographic measurements each in the RTL and LTL, using a convex probe of 1-4.5 MHz and a linear probe of 4-9 MHz, respectively. We also calculated mean TS values for each probe (resulting from the median TS values in RTL and LTL).

Data obtained from our cases were collected in a Microsoft Excel file, the statistical analysis being performed using the MedCalc program. ARFI measurements were numeric variables, so the mean values and standard deviation were calculated. The t test was used to compare mean ARFI values of TS.

The diagnostic performance of ARFI elastography was assessed using ROC curves that were constructed for prediction of thyroid pathology. Optimal cut-off values were chosen to maximize the sum of sensitivity (Se) and specificity (Sp). Se and Sp were calculated according to standard methods.

RESULTS

The mean TS values assessed by ARFI in normal and pathologic thyroid for the LTL and RTL, and the median values for LTL plus RTL are presented in Table 1.

TS assessed by means of ARFI in healthy subjects was significantly lower than in GD ($P < 0.0001$) and CAT patients ($P = 0.0002$), but the differences were not statistically significant between GD *vs* CAT cases ($P = 0.053$) (Figure 2).

The optimal cut-off value (in which the sum of Se and Sp was highest) for the prediction of diffuse thyroid pathology was 2.36 m/s. For this cut-off value, TS had 62.5% Se, 79.5% Sp, 87.6% positive predictive value (PPV), 55.5% negative predictive value (NPV) and 72.7% accuracy for the presence of diffuse thyroid pathology (AUROC = 0.804).

To obtain a Se > 90%, the best TS cut-off for predicting diffuse thyroid pathology was 1.81 m/s (90.2% Se, 40.9% Sp, 76.1% PPV, 66.6% NPV and 74.2% accuracy).

Table 1 Mean thyroid stiffness values assessed by acoustic radiation force impulse in normal patients and in patients with diffuse thyroid pathology

	RTL (m/s)	LTL (m/s)	P value	Mean ARFI (m/s)
Normal	1.98 ± 0.37	2.01 ± 0.48	0.74 (NS)	2 ± 0.40
GD	2.62 ± 0.58	2.72 ± 0.61	0.41 (NS)	2.67 ± 0.53
CAT	2.34 ± 0.61	2.53 ± 0.68	0.20 (NS)	2.43 ± 0.58

GD: Graves' disease; CAT: Chronic autoimmune thyroiditis; RTL: Right thyroid lobe; LTL: Left thyroid lobe; m/s: Meters/second; ARFI: Acoustic radiation force impulse; NS: Not significant.

Table 2 Mean acoustic radiation force impulse thyroid stiffness values in normal and diffuse thyroid pathology, with convex and linear probes, median of 10 measurements *vs* median of 5 measurements

	10 measurements (m/s)	5 measurements (m/s)	P value
Normal	2.01 ± 0.40	2.01 ± 0.40	1 (NS)
GD	2.64 ± 0.52	2.59 ± 0.54	0.66 (NS)
CAT	2.50 ± 0.56	2.45 ± 0.54	0.72 (NS)
Convex probe	2.09 ± 0.39	2.11 ± 0.45	0.85 (NS)
Linear probe	2.03 ± 0.36	2.06 ± 0.38	0.75 (NS)

GD: Graves' disease; CAT: Chronic autoimmune thyroiditis; NS: Not significant; m/s: Meters/second.

Table 3 Thyroid stiffness acoustic radiation force impulse measurements according to thyroid stimulating hormone levels

	ARFI values in patients with normal TSH (m/s)	ARFI values in patients with abnormal TSH (m/s)	P value
All patients	2.35 ± 0.49 (20 patients)	2.64 ± 0.56 (46 patients)	0.04
GD	2.12 ± 0.27 (6 patients)	2.67 ± 0.51 (29 patients)	0.01
CAT	2.42 ± 0.55 (11 patients)	2.49 ± 0.52 (14 patients)	0.74

GD: Graves' disease; CAT: Chronic autoimmune thyroiditis; ARFI: Acoustic radiation force impulse; TSH: thyroid stimulating hormone; m/s: Meters/second.

To obtain a Sp > 90% the best TS cut-off assessed by ARFI elastography was 2.53 m/s (54.3% Se, 90.9% Sp, 92.5% PPV, 48.7% NPV and 66.1% accuracy).

If we compared mean TS values obtained by convex *vs* linear probe, those obtained with the convex one were slightly higher, but not significantly so, than those obtained with the linear one (2.17 ± 0.51 m/s *vs* 2.04 ± 0.43 m/s, *P* = 0.19) (Table 2). Also, if only 5 ARFI measurements were performed in each thyroid lobe, their median values were not significantly different from the median values of 10 ARFI measurements (Table 2), in normal as well as in diffuse thyroid disease.

Also, if only 5 ARFI measurements were performed, the TS assessed by means of convex probe was slightly higher, but not significantly so, than those obtained with the linear probe (2.11 ± 0.45 m/s *vs* 2.06 ± 0.38 m/s, *P* = 0.63).

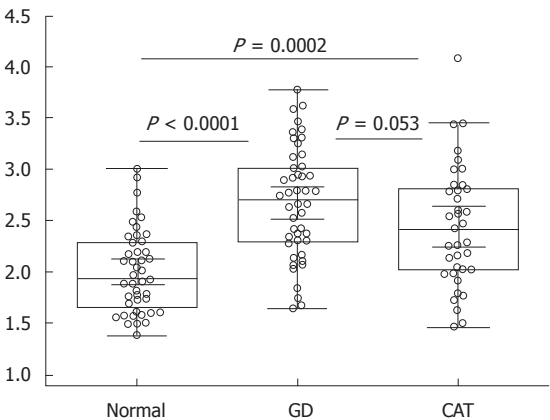


Figure 2 Mean thyroid stiffness values assessed by acoustic radiation force impulse elastography in healthy subjects *vs* patients with thyroid pathology. GD: Graves' disease; CAT: Chronic autoimmune thyroiditis.

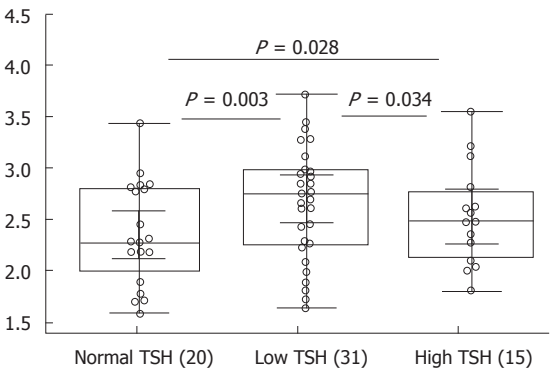


Figure 3 Mean thyroid stiffness values according to thyroid stimulating hormone levels. TSH: thyroid stimulating hormone.

The mean ARFI values were significantly higher in patients with thyroid pathology and low levels of TSH *vs* those with normal TSH (*P* = 0.03); however the mean ARFI values were similar in patients with low TSH *vs* higher TSH *P* = 0.34 and in patients with normal TSH *vs* higher TSH levels (*P* = 0.28) (Table 3, Figure 3). Also, TS was not correlated with the TSH levels: Spearman *r* coefficient = -0.157, *P* = 0.20.

DISCUSSION

GD is an autoimmune thyroid disorder characterized by diffuse goiter, thyrotoxicosis, orbitopathy and occasionally, infiltrative dermopathy. The clinical exam of the goiter by palpation reveals a parenchymatous elastic consistency and a specific bruit. CAT is another autoimmune thyroid disease that can induce goiter and/or thyroid dysfunction. Thyroid function is normal, low or rarely high. The classic form of CAT (Hashimoto's disease) presents a diffuse goiter with hard consistency at palpation. If GD is characterized by circulating anti-TSH immunoglobulins, CAT expresses serum antithyroid autoantibodies which, in time, damage the thyroid's morphofunctionality.

In previously published papers, thyroid elastography

has been used to evaluate thyroid nodule stiffness in order to differentiate malignant from benign ones^[16-22], usually using real time elastography (Hi RT-E). There is only one published study (also by our group) that evaluated thyroid stiffness by means of ARFI elastography in a group of 74 subjects, as a predictor of diffuse thyroid pathology^[23].

ARFI elastography involves targeting an anatomical region to be investigated for elastic properties with the use of an ROI cursor, while performing real-time B-mode imaging. Tissue in the ROI area is mechanically excited using short-duration (262 μ s) acoustic pulses with a fixed transmit frequency of 2.67 MHz to generate localized tissue displacement. The displacement results in shear wave propagation away from the region of excitation and is tracked using ultrasound correlation-based methods^[1,2]. The shear wave propagation velocity is proportional to the square root of tissue elasticity so that the propagation speed increases with fibrosis. Using image-based localization and a proprietary implementation of ARFI technology, shear wave speed may be quantified. Results are expressed in m/s. Measurement value and depth are also reported.

Considering that there are no manufacturer recommendations for TS evaluation, we performed 10 ARFI measurements in each thyroid lobe, after which a median value was calculated, similar to the evaluation of liver stiffness by means of transient elastography (TE) or ARFI. Thereafter, we retrospectively analyzed the results, when only the first 5 ARFI measurements were taken into consideration. TS values assessed by means of ARFI were not statistically significant different if 10 *vs* 5 ARFI measurements were performed in each thyroid lobe (Table 2), so that we can conclude that for TS assessment 5 measurements are enough.

In the practical evaluation of liver stiffness through elastographic methods (TE or ARFI), the high level of aminotransferases modifies the values obtained for liver stiffness^[24-26]. For this reason, we wanted to see if a modified thyroid function plays a role in the TS evaluation. We found that ARFI values were not correlated with TSH: Spearman *r* coefficient = -0.157, *P* = 0.20. Considering all the patients with thyroid pathology, the mean ARFI values were significantly higher in patients with abnormal TSH, as compared with those with normal TSH (Table 3).

In a very recently published study by Friedrich-Rust *et al.*^[20], ARFI was used for the evaluation of 55 patients with 60 thyroid nodules. TS measured by ARFI in the healthy tissue surrounding the nodule was compared to the nodules' stiffness. While no significant difference in median velocity was found between healthy thyroid tissue and benign thyroid nodules, a significant difference was found between malignant thyroid nodules on the one hand, and healthy thyroid tissue (*P* = 0.018) or benign thyroid nodules (*P* = 0.014) on the other hand.

Other elastographic methods have been used for TS assessment. In such a study, Bahn *et al.*^[27] used magnetic resonance elastography (MRE) to evaluate TS in cases

without thyroid pathology (12 subjects), in patients with Hashimoto thyroiditis (5 subjects), in patients with benign thyroid nodules (8 subjects) and with malignant thyroid nodules (2 subjects). Statistically significant differences were found between TS values in normal subjects (1.9 ± 0.6 kPa at 100 Hz and 1.3 ± 0.5 kPa at 80 Hz) and those with Hashimoto thyroiditis (2.8 ± 0.6 kPa at 100 Hz and 1.8 ± 0.6 kPa at 80 Hz) (*P* = 0.004 at 100 Hz). In the same MRE study, elastographic parameters could not differentiate benign from malignant thyroid nodules in this small cohort of patients.

In our study, TS assessed by means of ARFI in healthy subjects was significantly lower than in GD (*P* < 0.0001) and CAT patients (*P* = 0.0002), but the differences were not statistically significant between GD *vs* CAT patients (*P* = 0.053), meaning that even if we cannot differentiate by means of ARFI patients with GD from those with CAT, ARFI elastography could be used in clinical practice for differentiating normal thyroid from diffuse disease of the thyroid, maybe even as a first-line method, immediately after performing routine ultrasound examination of the gland.

ARFI elastography of the thyroid is feasible with either linear or convex probes and 5 measurements in every lobe are enough (median values) for an accurate assessment. ARFI evaluation seems to be a useful method for predicting the presence of autoimmune diffuse thyroid pathology, with high Sp and PPV (> 90%) for cut-off values > 2.53 m/s; being able to make a first differentiation between a normal thyroid and diffuse thyroid diseases immediately after ultrasound evaluation, thus opening a new field in thyroid elastography.

COMMENTS

Background

Elastographic methods are non-invasive means used for liver fibrosis evaluation. There is very limited knowledge regarding the use of elastography for diffuse thyroid pathology assessment. Considering the analogy of the two parenchymatous organs, liver and thyroid, authors tried to assess whether ultrasound-based elastography, by means of the acoustic radiation force impulse (ARFI) technique, could be useful for the evaluation of thyroid diffuse pathology.

Innovations and breakthroughs

ARFI elastography is a new method, based on ultrasound, used for the evaluation of tissue stiffness. In this study, the authors measured mean thyroid stiffness values assessed by ARFI elastography in healthy subjects *vs* patients with thyroid pathology. In the study, for a cut-off value > 2.36 m/s, thyroid stiffness assessed by ARFI elastography was accurate enough to predict the presence of diffuse thyroid pathology (AUROC = 0.804). For a cut-off value > 2.53 m/s, the specificity and positive predictive value were higher than 90%.

Peer review

This study supports the conclusion that thyroid ARFI evaluation seems to be a useful method for diffuse thyroid gland pathology assessment, as a first-line method immediately after ultrasound evaluation.

REFERENCES

- 1 Nightingale K, Soo MS, Nightingale R, Trahey G. Acoustic radiation force impulse imaging: in vivo demonstration of clinical feasibility. *Ultrasound Med Biol* 2002; **28**: 227-235
- 2 Mauldin FW, Zhu HT, Behler RH, Nichols TC, Gallippi CM. Robust principal component analysis and clustering meth-

- ods for automated classification of tissue response to ARFI excitation. *Ultrasound Med Biol* 2008; **34**: 309-325
- 3 **Ziol M**, Handra-Luca A, Kettaneh A, Christidis C, Mal F, Kazemi F, de Lédighen V, Marcellin P, Dhumeaux D, Trinchet JC, Beaugrand M. Noninvasive assessment of liver fibrosis by measurement of stiffness in patients with chronic hepatitis C. *Hepatology* 2005; **41**: 48-54
- 4 **Castéra L**, Vergniol J, Foucher J, Le Bail B, Chanteloup E, Haaser M, Darriet M, Couzigou P, De Lédighen V. Prospective comparison of transient elastography, Fibrotest, APRI, and liver biopsy for the assessment of fibrosis in chronic hepatitis C. *Gastroenterology* 2005; **128**: 343-350
- 5 **Afdhal N**. Debate: Are non-invasive tests ready to replace liver biopsy. favor of the use of non-invasive tests. *Clinical Care Options* 2006: 7-19
- 6 **Talwalkar JA**, Kurtz DM, Schoenleber SJ, West CP, Montori VM. Ultrasound-based transient elastography for the detection of hepatic fibrosis: systematic review and meta-analysis. *Clin Gastroenterol Hepatol* 2007; **5**: 1214-1220
- 7 **Friedrich-Rust M**, Ong MF, Martens S, Sarrazin C, Bojunga J, Zeuzem S, Herrmann E. Performance of transient elastography for the staging of liver fibrosis: a meta-analysis. *Gastroenterology* 2008; **134**: 960-974
- 8 **Castéra L**, Foucher J, Bernard PH, Carvalho F, Allaix D, Merrouche W, Couzigou P, de Lédighen V. Pitfalls of liver stiffness measurement: a 5-year prospective study of 13,369 examinations. *Hepatology* 2010; **51**: 828-835
- 9 **Lupsor M**, Badea R, Stefanescu H, Sparchez Z, Branda H, Serban A, Maniu A. Performance of a new elastographic method (ARFI technology) compared to unidimensional transient elastography in the noninvasive assessment of chronic hepatitis C. Preliminary results. *J Gastrointest Liver Dis* 2009; **18**: 303-310
- 10 **Sporea I**, Sirli RL, Deleanu A, Popescu A, Focsa M, Danila M, Tudora A. Acoustic radiation force impulse elastography as compared to transient elastography and liver biopsy in patients with chronic hepatopathies. *Ultraschall Med* 2011; **32** Suppl 1: S46-S52
- 11 **Goertz RS**, Zopf Y, Jugl V, Heide R, Janson C, Strobel D, Bernatik T, Haendl T. Measurement of liver elasticity with acoustic radiation force impulse (ARFI) technology: an alternative noninvasive method for staging liver fibrosis in viral hepatitis. *Ultraschall Med* 2010; **31**: 151-155
- 12 **Sporea I**, Sirli R, Deleanu A, Tudora A, Popescu A, Curescu M, Bota S. Liver stiffness measurements in patients with HBV vs HCV chronic hepatitis: a comparative study. *World J Gastroenterol* 2010; **16**: 4832-4837
- 13 **Rigamonti C**, Donato MF, Fraquelli M, Agnelli F, Ronchi G, Casazza G, Rossi G, Colombo M. Transient elastography predicts fibrosis progression in patients with recurrent hepatitis C after liver transplantation. *Gut* 2008; **57**: 821-827
- 14 **Riggio S**, Mamone F, Mandraffino G, Maimone S, Alibrandi A, Manti L, Saitta C, Tripodi PF, Sardo MA, Squadrito G, Saitta A. Assessment of liver stiffness in subjects affected by familial combined hyperlipidaemia with hepatic steatosis. *Eur J Clin Invest* 2010; **40**: 722-728
- 15 **Basaria S**, Cooper DS. Amiodarone and the thyroid. *Am J Med* 2005; **118**: 706-714
- 16 **Rago T**, Santini F, Scutari M, Pinchera A, Vitti P. Elastography: new developments in ultrasound for predicting malignancy in thyroid nodules. *J Clin Endocrinol Metab* 2007; **92**: 2917-2922
- 17 **Kagoya R**, Monobe H, Tojima H. Utility of elastography for differential diagnosis of benign and malignant thyroid nodules. *Otolaryngol Head Neck Surg* 2010; **143**: 230-234
- 18 **Wang Y**, Dan HJ, Dan HY, Li T, Hu B. Differential diagnosis of small single solid thyroid nodules using real-time ultrasound elastography. *J Int Med Res* 2010; **38**: 466-472
- 19 **Hong Y**, Liu X, Li Z, Zhang X, Chen M, Luo Z. Real-time ultrasound elastography in the differential diagnosis of benign and malignant thyroid nodules. *J Ultrasound Med* 2009; **28**: 861-867
- 20 **Friedrich-Rust M**, Romenski O, Meyer G, Dauth N, Holzer K, Grünwald F, Kriener S, Herrmann E, Zeuzem S, Bojunga J. Acoustic Radiation Force Impulse-Imaging for the evaluation of the thyroid gland: a limited patient feasibility study. *Ultrasonics* 2012; **52**: 69-74
- 21 **Vorländer C**, Wolff J, Saalabian S, Lienenlücke RH, Wahl RA. Real-time ultrasound elastography—a noninvasive diagnostic procedure for evaluating dominant thyroid nodules. *Langenbecks Arch Surg* 2010; **395**: 865-871
- 22 **Asteria C**, Giovanardi A, Pizzocaro A, Cozzaglio L, Morabito A, Somalvico F, Zoppo A. US-elastography in the differential diagnosis of benign and malignant thyroid nodules. *Thyroid* 2008; **18**: 523-531
- 23 **Sporea I**, Vlad M, Bota S, Sirli RL, Popescu A, Danila M, Sendroiu M, Zosin I. Thyroid stiffness assessment by acoustic radiation force impulse elastography (ARFI). *Ultraschall Med* 2011; **32**: 281-285
- 24 **Coco B**, Oliveri F, Maina AM, Ciccorossi P, Sacco R, Colombaro P, Bonino F, Brunetto MR. Transient elastography: a new surrogate marker of liver fibrosis influenced by major changes of transaminases. *J Viral Hepat* 2007; **14**: 360-369
- 25 **Bota S**, Sporea I, Sirli R, Popescu A, Danila M, Sendroiu M. Factors that influence the correlation of acoustic radiation force impulse (ARFI), elastography with liver fibrosis. *Med Ultrason* 2011; **13**: 135-140
- 26 **Chan HL**, Wong GL, Choi PC, Chan AW, Chim AM, Yiu KK, Chan FK, Sung JJ, Wong VW. Alanine aminotransferase-based algorithms of liver stiffness measurement by transient elastography (Fibroscan) for liver fibrosis in chronic hepatitis B. *J Viral Hepat* 2009; **16**: 36-44
- 27 **Bahn MM**, Brennan MD, Bahn RS, Dean DS, Kugel JL, Ehmman RL. Development and application of magnetic resonance elastography of the normal and pathological thyroid gland in vivo. *J Magn Reson Imaging* 2009; **30**: 1151-1154

S- Editor Cheng JX L- Editor Logan S E- Editor Xiong L



Quantitative measurement of contrast enhancement of esophageal squamous cell carcinoma on clinical MDCT

Rui Li, Tian-Wu Chen, Li-Ying Wang, Li Zhou, Hang Li, Xiao-Li Chen, Chun-Ping Li, Xiao-Ming Zhang, Ru-Hui Xiao

Rui Li, Tian-Wu Chen, Li-Ying Wang, Li Zhou, Hang Li, Xiao-Li Chen, Chun-Ping Li, Xiao-Ming Zhang, Ru-Hui Xiao, Sichuan Key Laboratory of Medical Imaging, and Department of Radiology, Affiliated Hospital of North Sichuan Medical College, Nanchong 637000, Sichuan Province, China

Author contributions: Li R, Chen TW, Wang LY, Zhou L, Li H, Chen XL, Li CP, Zhang XM and Xiao RH designed the research; Li R, Wang LY and Zhou L performed the research; Li R, Chen TW and Li CP contributed analytic tools; Li R, Chen TW, Wang LY and Zhou L analyzed the data; Li R and Chen TW wrote the paper; Li R, Chen TW, Wang LY, Zhou L, Li H, Chen XL, Li CP, Zhang XM and Xiao RH revised the paper.

Supported by The Science Foundation for Distinguished Young Scholars of Sichuan Province, China, No. 2010JQ0039

Correspondence to: Tian-Wu Chen, Professor, Department of Radiology, Affiliated Hospital of North Sichuan Medical College, 63 Wenhua Road, Nanchong 637000, Sichuan Province, China. twchenscu@yahoo.com.cn

Telephone: +86-817-2262236 Fax: +86-817-2262124

Received: December 22, 2011 Revised: March 5, 2012

Accepted: March 12, 2012

Published online: April 28, 2012

Abstract

AIM: To investigate contrast-enhanced computed tomography (CECT) for discriminating esophageal squamous cell carcinoma (ESCC) from normal esophagus and evaluating outcomes within tumors after chemoradiotherapy (CRT).

METHODS: Sixty-four patients with surgical ESCC served as group A, and underwent thoracic contrast-enhanced scan with 16-section multidetector row CT 1 wk before surgery. Thirty-five patients with advanced ESCC receiving 4-wk CRT and showing response to CRT served as group B, and underwent CT scans similar with group A 4 wk after completion of CRT. In group A, differences in CT attenuation values (in HU) between the preoperative ESCC and background normal esophageal wall (delta CT₁), or between different background

normal esophageal walls (delta CT₂) were compared. Furthermore, delta CT₁ between group A and B was also compared.

RESULTS: In group A, mean delta CT₁ was higher than delta CT₂ (23.86 ± 10.59 HU vs 6.24 ± 3.06 HU, $P < 0.05$). When a delta CT₁ of 10.025 HU was employed at a cut-off value to discriminate ESCC from normal esophagus, a sensitivity of 89.1% and specificity of 90.6% were achieved. Mean delta CT₁ was lower in group B than in group A (9.25 ± 10.86 vs 23.86 ± 10.59 , $P < 0.05$), and a delta CT₁ of 15.45 HU was obtained at a cut-off value to assess the CRT changes with a sensitivity of 76.6% and specificity of 77.1%.

CONCLUSION: CECT might be a clinical technique for discriminating ESCC from normal esophagus, and evaluating outcome in the tumors treated with CRT.

© 2012 Baishideng. All rights reserved.

Key words: Esophagus; Squamous cell carcinoma; Multi-detector row computed tomography; Attenuation value; Chemoradiotherapy

Peer reviewer: Sergio Casciaro, PhD, Institute of Clinical Physiology - National Research Council, Campus Universitario Ecotekne, Via Monteroni, 73100 Lecce, Italy

Li R, Chen TW, Wang LY, Zhou L, Li H, Chen XL, Li CP, Zhang XM, Xiao RH. Quantitative measurement of contrast enhancement of esophageal squamous cell carcinoma on clinical MDCT. *World J Radiol* 2012; 4(4): 179-185 Available from: URL: <http://www.wjgnet.com/1949-8470/full/v4/i4/179.htm> DOI: <http://dx.doi.org/10.4329/wjr.v4.i4.179>

INTRODUCTION

Esophageal carcinoma is one of the most frequent causes

of death from digestive systemic malignant tumors, and the squamous cell carcinoma is the frequent histological type^[1]. Tumor resection is a well established curative treatment protocol for patients with nonmetastatic esophageal squamous cell carcinoma (ESCC)^[2]. However, some patients with advanced ESCC have primary cancer associated with systemic spread at diagnosis, and the outcome of surgery alone for these patients was not satisfying^[3,4]. In the process of the tumor cells spreading through the bloodstream to distant tissues, tumor angiogenesis plays a key role^[5,6]. For patients with advanced esophageal carcinoma, chemoradiotherapy (CRT) has been established as an effective treatment which is widely performed in clinical settings^[7].

Several imaging procedures, such as endoscopy and endoscopic ultrasound (EUS), have been used to assess response to neoadjuvant chemotherapy and radiation therapy by comparison of tumor volume between pre- and post-CRT imaging^[8]. However, these methods are limited by their inability to traverse a malignant stricture occurring in 20-30% esophageal carcinoma patients and by their operator dependency^[9,10]. EUS may also have a potential risk of perforation^[11]. As a noninvasive imaging technique, computed tomography (CT) is the most common approach for evaluating cancers, and contrast-enhanced CT (CECT), which can overcome the limitations of endoscopy and EUS, has been clinically applied to detect esophageal primary tumors and lymph node or distant metastasis, and to assess the response to neoadjuvant chemotherapy and radiation therapy^[12-14].

Furthermore, tumor angiogenesis is characterized by an increase in tumor blood vessel count, and this process will impact on CECT^[15-19]. We presume that the level of CT enhancement might be interpreted as an indicator of tumor angiogenesis. To the best of our knowledge, few articles have focused on the CT attenuation value in esophageal tumor and background normal esophagus on CECT in patients treated with or without CRT. Thus, the objective of this study was to investigate the feasibility of CECT to quantitatively distinguish esophageal tumor from background normal esophagus, and for assessing therapeutic outcome in patients with cancer who received CRT in a clinical settings.

MATERIALS AND METHODS

Participants

The institutional ethics committee of our hospital approved this study, and written informed consent was obtained from each participant prior to the study.

According to the therapeutic strategy, there were two groups - group A and B - in our study. Patients were enrolled into group A according to the following inclusion criteria: (1) they had ESCC initially confirmed by endoscopic biopsy; (2) the mass was clearly visible on CECT images; (3) the patients did not receive any tumor-related treatment such as radiotherapy, or chemotherapy prior to the CT examination; and (4) there were no contraindications to tumor resection for therapy with thoracotomy.

Patients were enrolled into group B if ESCC was pathologically confirmed, if there were contraindications to tumor resection for therapy with thoracotomy, if they received CRT and showed a response to CRT, if they underwent CECT at least 4 wk after the therapy, and if the mass was clearly visible on CECT images.

From January to November 2010, 64 consecutive patients (53 men and 11 women; mean age, 61.51 years; age range, 37-79 years) with endoscopic biopsy proven ESCC, who met the inclusion criteria, were enrolled into group A. In this group, the mean coverage of the tumor along the z-axis was 5.33 ± 2.85 cm (range 2.54-8.42 cm). The tumors were located in the lower thoracic portion of the esophagus in 10 patients, in both the midthoracic and lower thoracic portion in 17, in the midthoracic portion in 27, in both the upper thoracic and midthoracic portion in 8, and in upper thoracic portion in 2. One week after the CECT scan, all patients underwent tumor resection with thoracotomy. According to the postoperative pathology, all the surgical margins were not involved by this carcinoma.

During the same period, 35 patients (29 men, 6 women; mean age 56.75 years; age range from 47 to 76 years) with unresectable ESCC, who had already completed a CRT schedule for at least 4 wk, served as group B. The mean coverage of the tumor along the z-axis was 3.79 ± 2.13 cm (range 1.33-6.91 cm). The tumors were located in the lower thoracic portion of esophagus in 9 patients, in both the midthoracic and lower thoracic portion in 4, in the midthoracic portion in 7, in both the upper thoracic and midthoracic portion in 4, and in the upper thoracic portion in 11. CRT consisted of simultaneous radiotherapy and chemotherapy. For radiotherapy, the patients were irradiated using a 10-MV linear accelerator photon beam at a daily dose of 2 Gy, which was continued daily 5 times per week for 4 wk, to a total dose of 40 Gy. The target included the primary tumor and the enlarged regional lymph nodule. The chemotherapy schedule, which was initiated on day 1 of radiotherapy, consisted of cisplatin (7 mg/m^2 per day) by intravenous administration and 5-fluorouracil (350 mg/m^2 per day) by continuous intravenous infusion for 5 d^[20,21]. All patients showed a therapeutic response to CRT, which was assessed 4 wk after the completion of CRT according to the therapeutic criteria defined by the World Health Organization^[22].

Imaging acquisition

Patients in groups A and B underwent spiral thoracic enhanced scans with a 16-section multidetector row CT (MDCT) system (Aquilion 16 CFX Edition, Toshiba Medical System, Japan) 1 wk before tumor resection and 4 wk after completion of CRT, respectively. Each patient received 200-400 mL water as oral esophageal negative contrast material immediately before the examination. A 19-gauge cannula was placed into an antecubital fossa vein after the patient lay supine on the scanner table. Eighty milliliters of a nonionic contrast medium (Ultravist



Figure 1 Oblique sagittal reformatted computed tomography images (A) of a 75-year-old man with squamous cell carcinoma in the lower thoracic portion of the esophagus (black arrows). The surgical cut edge is determined by a radiologist and a pathologist working in consensus (white arrowhead); and the background normal esophagus (white arrows) has been chosen in the thoracic upper portion. To generate the enhanced attenuation, two regions of interest (B and C) for the esophageal cancer and for the background normal esophagus are drawn freehand around the tumor and around the esophageal wall, respectively; the enhanced attenuation values correspond to 84 HU and 57 HU, respectively.

300, Iopamidol, Schering, Germany) containing 300 mg of iodine per milliliter was administered intravenously as a bolus with a flow rate of 2.5-3.0 mL/s using an automatic injector (MEDRAD Vistron CT Injection System, Medrad company, USA). Enhanced CT was performed 35 s after the initiation of the bolus contrast injection using the following scanning parameters: 120 kV, 100 mAs, 0.5 s rotation time, a pitch of 0.938, 400 mm field of view, 7 mm section thickness, and 512 mm × 512 mm matrix. Each scan was performed during a breath-hold to minimize the movement of the esophagus. All data were reconstructed with a 1 mm section thickness at 1 mm intervals, and were then transferred to an image processing workstation (Vitrea 2.0 vital images, Minnesota, USA).

Image analysis

Image data in groups A and B were retrospectively reviewed on the image processing workstation by an experienced radiological professor (the corresponding author with 13 years of experience in thoracoabdominal radiology), and an experienced radiologist (the first author with 4 years of experience in thoracoabdominal radiology) by consensus to keep the accuracy of analysis focusing on the difference in attenuation values (ΔCT , in Hounsfield units) between the tumor and background normal esophageal wall (ΔCT_1 , in Hounsfield units) in group A and B, or between background normal esophageal walls (ΔCT_2 , in Hounsfield units) in group A.

In order to measure the attenuation of the tumor in groups, reconstructed axial images (Figure 1A) were used to reformat the oblique-sagittal images at 1.0 mm intervals with a slice thickness of 1.0 mm to display the extension of esophageal carcinoma. Standard mediastinal window images (window width, 400 HU; window level, 60 HU) were used for displaying the images. Based on the extension of the tumor on the oblique-sagittal view, ten contiguous transverse sections corresponding to the maximal segment of tumors were selected for the representative tumor sections. A reliable tumor region of interest (ROI) within the representative thickened esophageal wall was

manually drawn in the transverse section, and the area of tumor ROI (area range: 36-408 mm²) was more than 60% of that of the entire tumor in the section (Figure 1B). The tumor attenuation value was derived automatically by the software on this image processing workstation. To minimize partial volume averaging with surrounding tissues, care was taken to draw the ROI of the tumor to exclude periesophageal fat and intraluminal gas, and to avoid the necrotic area within the tumor. This previous process and analysis was repeated for each contiguous transverse level, until the ten representative tumor sections had been covered. All ten attenuation values were then averaged across all the sections to be regarded as the representative attenuation values for esophageal carcinomas.

For measuring the attenuation value of background normal esophagus in groups, the ROI of the normal esophagus was determined. In group A, the tumor did not involve the surgical cut edge in all patients confirmed by the postoperative pathology, and the residual portions of esophagus after surgery were determined as background normal esophagus. According to the postoperative pathology and the reformatted images in the oblique-sagittal plane (Figure 1A), five contiguous axial sections corresponding to the background normal esophagus were randomly selected for each patient in group A. In group B, the portions of background esophagus 5 cm away from the irradiating target were determined as background normal esophagus, and five contiguous axial sections corresponding to the background normal esophagus were also randomly selected. The measurement of CT values in the normal esophagus was similar to that in esophageal carcinoma.

Subsequently, ΔCT_1 was calculated by subtracting the referenced attenuation value for the background normal esophageal wall from the representative attenuation value for esophageal carcinomas. ΔCT_2 was defined as the standard deviation of the attenuation value for the portions of background normal esophagus, which was in accordance with the difference in attenuation values between background normal esophageal walls.

Table 1 Repeatability of measurements of ΔCT_1 in group A and group B (mean \pm SD)

Group	Mean differences of replicated measurements			95% Interobserver correlation coefficient
	Differences between two sets of measurements	95% CI of the difference	95% limits of agreement	
A (HU)	-0.2 \pm 9.03	-17.8 to 17.5	-18.26 to 17.86	0.9913 (0.9817 to 0.9933)
B (HU)	-1.2 \pm 12.6	-26 to 23.5	-26.4 to 24	0.9956 (0.9911 to 0.9978)

ΔCT_1 : Difference in attenuation value between esophageal tumor and background normal esophagus.

To clarify the inter-observer agreement on the measurement of ΔCT , we randomly assessed the reproducibility of ΔCT_1 measurement. Data from each group was reanalyzed by the other observers (the third author with 3 years of experience in thoracoabdominal radiology, and the fourth author with 2 years of experience in radiology). We then compared two sets of the measurements, and if good agreement between the replicated measurements was achieved, values of the first set were regarded as the final ΔCT_1 .

Statistical analysis

Repeatability between two sets of measurements for ΔCT_1 was assessed by Bland and Altman analysis^[23]. The mean differences and their 95% CI between two sets of measurements, and 95% limits of agreement for ΔCT_1 were determined to evaluate the difference in replicated measurements. The interclass correlation coefficients and their 95% CI were applied to assess the level of agreement. If the interclass correlation coefficient was greater than 0.99, and the mean difference of the replicated measurements was close to zero, good agreement between the replicated measurements was considered to be obtained^[23].

By using the statistical software (version 13.0 for Windows, SPSS Inc., Chicago, IL, USA), independent sample Student's *t* tests were subsequently performed to compare ΔCT_1 and ΔCT_2 in group A, and ΔCT_1 between group A and B. The probability value of less than 0.05 was considered to indicate a significant difference. If significant difference was proved, receiver operating characteristic (ROC) analysis was then carried out to determine the cutoff of ΔCT_1 for discriminating esophageal carcinoma from background normal esophagus, and for assessing the CRT change of esophageal carcinoma.

RESULTS

Repeatability of measurement of ΔCT_1 in groups

In group A, the mean CT attenuation value of background normal esophagus was 53.77 ± 7.04 HU (range, 30.98 to 68.62 HU). The mean CT attenuation value of esophageal carcinoma was 77.62 ± 9.13 HU (range, 63.18 to 106.23 HU) for the initial measurement. The first set of mean ΔCT_1 was 23.86 ± 10.59 HU (range, -1.85 to 44.86 HU). For the repeated measurement, mean CT attenuation value of esophageal carcinoma was

77.61 ± 9.11 HU (range, 63.06 to 105.86 HU), and the repeated set of mean ΔCT_1 was 23.83 ± 10.60 HU (range, -2.56 to 47.02 HU).

In group B, the mean CT value of background normal esophagus was 55.09 ± 7.30 HU (range, 37.68 to 71 HU). For the initial measurement, the mean CT value of esophageal cancer and mean ΔCT_1 were 64.35 ± 12.89 HU (range from 34.07 to 94.82 HU) and 9.25 ± 10.86 HU (range from -10.02 to 35.67 HU), respectively; and for the replicated measurement, the mean CT attenuation value of esophageal cancer and mean ΔCT_1 were 64.25 ± 12.99 HU (range from 33.98 to 64.26 HU) and 9.16 ± 10.84 HU (range from -10.39 to 34.24), respectively. A high level of repeatability of ΔCT_1 measurements was achieved in groups (Table 1).

Difference in CT values: Between esophageal cancer and background normal esophagus vs between background normal esophageal walls

In patients with esophageal carcinoma in group A, the mean ΔCT_1 was 23.86 ± 10.59 HU, and mean ΔCT_2 was 6.24 ± 3.06 HU (range, 2.39 to 18.66 HU). ΔCT_1 was significantly higher than ΔCT_2 in group A ($P < 0.0001$). To discriminate the visual difference of esophageal carcinoma from that of background normal esophageal walls, the ROC curve analysis (Figure 2A) was performed between ΔCT_1 and ΔCT_2 , and an area under the curve of 0.948 (95% CI: 0.906 to 0.99, $P < 0.0001$) was observed. By using 10.025 HU of ΔCT_1 as the cut-off value, the ROC curve showed a sensitivity of 89.1%, a specificity of 90.6%, a positive predictive value of 90.4%, a negative predictive value of 89.2%, and an accuracy of 89.8%.

Difference in CT values: Tumors with and without CRT

In patients treated with and without CRT, mean ΔCT_1 was 23.86 ± 10.59 HU and 9.25 ± 10.86 HU in group A and group B, respectively. Due to the treatment, mean ΔCT_1 was markedly decreased in group B compared with that in group A ($P < 0.0001$). To assess the therapeutic change, the ROC curve analysis (Figure 2B) was also performed between ΔCT_1 in groups, and an area under the curve of 0.833 (95% CI: 0.746 to 0.920, $P < 0.0001$) was observed. By using 15.45 HU of ΔCT_1 as the cut-off value, the ROC curve showed a sensitivity of 76.6%, a specificity of 77.1%, a positive predictive value of 64.29%, a negative predictive value of 85.96%, and an accuracy of 76.77%.

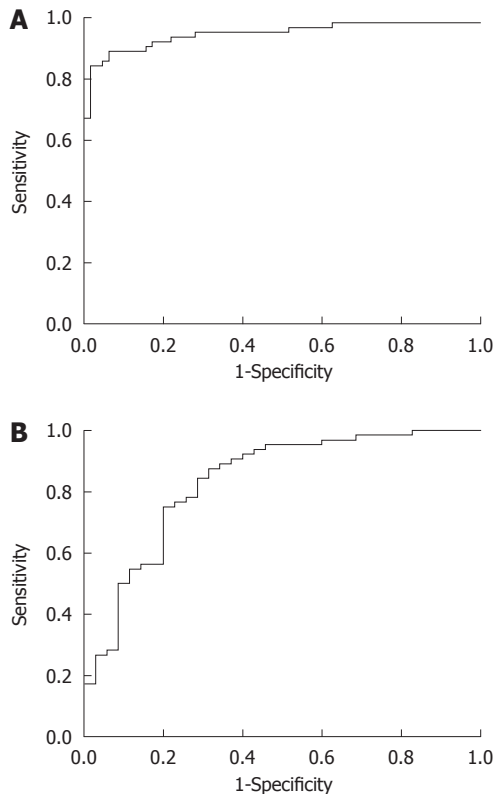


Figure 2 Receiver operating characteristic curve of difference in contrast enhancement between esophageal squamous cell carcinoma and background normal esophagus. A: Discriminating the tumor from background normal esophagus (area under ROC curve = 0.948, $P < 0.0001$); B: Discriminating between the therapeutic change of esophageal squamous carcinoma treated with and without chemoradiotherapy (area under ROC curve = 0.833, $P < 0.0001$).

DISCUSSION

In this study, an unenhanced CT scan was not performed prior to contrast-enhanced scan to control the patient radiation dose by lowering scan time. A 16-section MDCT was used to perform the enhancement data acquisitions, which has better collimation of X-ray beams and newer filter design compared with single section spiral CT^[24,25]. As shown in our study, the measurement of difference in contrast enhancement between esophageal carcinoma and background normal esophageal wall might be a reproducible technique, because good agreement between replicated measurements of the difference was obtained. Thus, we used a contrast-enhanced scan with 16-section MDCT in the present study.

Clinically, the results of our study showed that the contrast-enhanced attenuation value within ESCC was significantly higher than that in the background normal esophageal wall. Our findings were consistent with those obtained by triple-phase dynamic CT (23.86 ± 10.59 HU *vs* 28.3 ± 17.1 HU)^[12]. Our findings may be explained by the fact that ESCC is typically hypervascular^[26,27], and the process of developing a new arterial vessel supply and the formation of tumor microvessels in the tumors could result in a marked increase of enhanced attenuation value.

Because of a significantly higher difference in CT enhancement between the tumor and background normal esophagus *vs* between background normal esophageal walls, the difference in CT enhancement between the tumor and background normal esophagus illustrated by ΔCT_1 could be used as a criterion to differentiate tumor from background normal esophagus. A threshold value of ΔCT_1 was obtained by performing ROC analysis. Our findings suggested that the cut-off ΔCT_1 of 10.025 HU had high sensitivity, specificity, positive predictive value, negative predictive value and accuracy at more than 85%. Therefore, a ΔCT_1 value of 10.025 HU may be used as a criterion to discriminate the microcirculation of ESCCs from that of the background normal esophagus.

Another finding in our study is that the difference in contrast enhancement between the tumor and background normal esophageal wall was significantly lower in patients treated with CRT than without CRT. These phenomena might be attributed to the cytotoxic effects of X-rays on the vascular endothelium cells within squamous cell carcinoma^[28], and the tumor vascularity may shrink after CRT, resulting in lower CECT. We used ROC analysis to evaluate the therapeutic change within tumors and our findings suggested that the cut-off ΔCT_1 of 15.45 HU had sensitivity, specificity, negative predictive value and accuracy at more than 75%. Hence, a ΔCT_1 value of 15.45 HU could be used as a criterion to evaluate therapeutic changes in tumors treated by CRT.

Our research has limitations. Firstly, measurement of CT enhancement is a semi-quantitative method for assessing the tumor vascularity, and is significantly constrained by the impact of patient cardiac output and central blood volume. To try our best to overcome this limitation, we measured the extent of CT enhancement within the tumor by subtracting the attenuation value of background normal esophageal walls from that of esophageal tumors, which may help to avoid the confounding influence of cardiac output and central blood volume. Another limitation is that normal esophagus was more subject to partial volume averaging with adjacent tissue or air, which may influence the accuracy of the measurement of CT enhancements in the esophageal wall. To minimize partial volume averaging, the measurements of CT enhancement were analyzed on thin-section and magnifying images.

The cut-off value of difference in CT enhancement between ESCC and background normal esophagus ($\Delta CT_1 = 10.025$ HU) could be used to quantitatively discriminate tumor from normal esophagus, and the cut-off value of difference in ΔCT_1 between the tumors treated with and without CRT (15.45 HU) could be used to assess the outcomes of CRT *in vivo* in clinical settings. Recently, fully automatic methods for 2D and 3D segmentation of liver structures from CT scans were developed to obtain high accuracy for demonstrating the liver volume, hepatic tumor and vessel morphology^[29,30]. Automated methods for 3D segmentation of esophagus from CT scans had also developed to obtain high accuracy for showing the

anatomy of esophagus^[31]. Based on the difference in CT enhancement between ESCC and background normal esophagus, we hope to develop the techniques of automatic segmentation for depicting the profile of ESCC for surgical planning and to determine the therapeutic outcomes of CRT, which will be performed in our future study.

COMMENTS

Background

Esophageal squamous cell carcinoma (ESCC) is one of the most frequent causes of death from digestive systemic malignant tumors. In the process of the tumor cells spreading through the bloodstream to distant tissues, tumor angiogenesis plays a key role and is characterized by an increase in tumor blood vessel count, which will impact on contrast-enhanced computed tomography (CECT). However, few articles have focused on the CT attenuation value in esophageal tumor and background normal esophagus on CECT in patients treated with or without chemoradiotherapy (CRT).

Research frontiers

CT attenuation values (in HU) of ESCC and background normal esophageal walls were measured on thoracic contrast-enhanced CT data. The differences in CT attenuation values between surgical ESCC and background normal esophageal wall (ΔCT_1), and between different background normal esophageal walls (ΔCT_2) were compared for discriminating ESCC from normal esophagus. In addition, the differences in ΔCT_1 between patients with ESCC treated with and without CRT was compared for evaluating the CRT outcomes.

Innovations and breakthroughs

The cut-off value of difference in CT enhancement between ESCC and background normal esophagus ($\Delta CT_1 = 10.025$ HU) could be used to quantitatively discriminate the tumor from normal esophagus, and the cut-off value of difference in ΔCT_1 between the tumors treated with and without CRT (15.45 HU) could be used to assess the outcomes of CRT *in vivo* in a clinical setting.

Applications

Based on the difference in CT enhancement between ESCC and background normal esophagus, we hope to develop the techniques of automatic segmentation for depicting the profile of ESCC for surgical planning and for determining the therapeutic outcomes of CRT.

Terminology

Thoracic contrast-enhanced CT is a valuable procedure to quantitatively measure the difference in CT enhancement between ESCC and background normal esophageal wall. It is hoped that this can be used to develop automatic segmentation techniques for depicting the profile of ESCC for surgical planning and determination of the therapeutic outcomes of CRT.

Peer review

In this paper, the authors demonstrated that difference in CT enhancement between ESCC and background normal esophagus could quantitatively discriminate the tumor from normal esophagus. The addressed research topic is of great importance in the field and the presented work effectively illustrates the final finding of the study.

REFERENCES

- Jemal A, Siegel R, Ward E, Hao Y, Xu J, Murray T, Thun MJ. Cancer statistics, 2008. *CA Cancer J Clin* 2008; **58**: 71-96
- Kranzfelder M, Büchler P, Lange K, Friess H. Treatment options for squamous cell cancer of the esophagus: a systematic review of the literature. *J Am Coll Surg* 2010; **210**: 351-359
- Daly JM, Karnell LH, Menck HR. National Cancer Data Base report on esophageal carcinoma. *Cancer* 1996; **78**: 1820-1828
- Ohtsu A, Boku N, Muro K, Chin K, Muto M, Yoshida S, Satake M, Ishikura S, Ogino T, Miyata Y, Seki S, Kaneko K, Nakamura A. Definitive chemoradiotherapy for T4 and/or M1 lymph node squamous cell carcinoma of the esophagus. *J Clin Oncol* 1999; **17**: 2915-2921
- Weidner N. Intratumor microvessel density as a prognostic factor in cancer. *Am J Pathol* 1995; **147**: 9-19
- Hanahan D, Folkman J. Patterns and emerging mechanisms of the angiogenic switch during tumorigenesis. *Cell* 1996; **86**: 353-364
- Urschel JD, Ashiku S, Thurer R, Sellke FW. Salvage or planned esophagectomy after chemoradiation therapy for locally advanced esophageal cancer--a review. *Dis Esophagus* 2003; **16**: 60-65
- Cerfolio RJ, Bryant AS, Ohja B, Bartolucci AA, Eloubeidi MA. The accuracy of endoscopic ultrasonography with fine-needle aspiration, integrated positron emission tomography with computed tomography, and computed tomography in restaging patients with esophageal cancer after neoadjuvant chemoradiotherapy. *J Thorac Cardiovasc Surg* 2005; **129**: 1232-1241
- Mallery S, Van Dam J. Increased rate of complete EUS staging of patients with esophageal cancer using the nonoptical, wire-guided echoendoscope. *Gastrointest Endosc* 1999; **50**: 53-57
- Pfau PR, Ginsberg GG, Lew RJ, Faigel DO, Smith DB, Kochman ML. Esophageal dilation for endosonographic evaluation of malignant esophageal strictures is safe and effective. *Am J Gastroenterol* 2000; **95**: 2813-2815
- Wallace MB, Hawes RH, Sahai AV, Van Velse A, Hoffman BJ. Dilation of malignant esophageal stenosis to allow EUS guided fine-needle aspiration: safety and effect on patient management. *Gastrointest Endosc* 2000; **51**: 309-313
- Umeoka S, Koyama T, Togashi K, Saga T, Watanabe G, Shimada Y, Imamura M. Esophageal cancer: evaluation with triple-phase dynamic CT--initial experience. *Radiology* 2006; **239**: 777-783
- Yoon YC, Lee KS, Shim YM, Kim BT, Kim K, Kim TS. Metastasis to regional lymph nodes in patients with esophageal squamous cell carcinoma: CT versus FDG PET for presurgical detection prospective study. *Radiology* 2003; **227**: 764-770
- Wu LF, Wang BZ, Feng JL, Cheng WR, Liu GR, Xu XH, Zheng ZC. Preoperative TN staging of esophageal cancer: comparison of miniprobe ultrasonography, spiral CT and MRI. *World J Gastroenterol* 2003; **9**: 219-224
- Dvorak HF, Brown LF, Detmar M, Dvorak AM. Vascular permeability factor/vascular endothelial growth factor, microvascular hyperpermeability, and angiogenesis. *Am J Pathol* 1995; **146**: 1029-1039
- Baillie CT, Winslet MC, Bradley NJ. Tumour vasculature--a potential therapeutic target. *Br J Cancer* 1995; **72**: 257-267
- Jain RK. Determinants of tumor blood flow: a review. *Cancer Res* 1988; **48**: 2641-2658
- Miles KA. Tumour angiogenesis and its relation to contrast enhancement on computed tomography: a review. *Eur J Radiol* 1999; **30**: 198-205
- Ahn MJ, Jang SJ, Park YW, Choi JH, Oh HS, Lee CB, Paik HK, Park CK. Clinical prognostic values of vascular endothelial growth factor, microvessel density, and p53 expression in esophageal carcinomas. *J Korean Med Sci* 2002; **17**: 201-207
- Doki Y, Takachi K, Ishikawa O, Sasaki Y, Miyashiro I, Ohigashi H, Yano M, Ishihara R, Tsukamoto Y, Nishiyama K, Ishiguro S, Imaoka S. Reduced tumor vessel density and high expression of glucose transporter 1 suggest tumor hypoxia of squamous cell carcinoma of the esophagus surviving after radiotherapy. *Surgery* 2005; **137**: 536-544
- Yano M, Yasuda T, Miyata H, Fujiwara Y, Takiguchi S, Monden M. Correlation between histological effects on the main tumors and nodal status after chemoradiotherapy for squamous cell carcinoma of the esophagus. *J Surg Oncol* 2005; **89**: 244-250; discussion 250
- Miller AB, Hoogstraten B, Staquet M, Winkler A. Reporting results of cancer treatment. *Cancer* 1981; **47**: 207-214
- Bland JM, Altman DG. Statistical methods for assessing agreement between two methods of clinical measurement. *Lancet* 1986; **1**: 307-310

- 24 **Greess H**, Wolf H, Baum U, Lell M, Pirkel M, Kalender W, Bautz WA. Dose reduction in computed tomography by attenuation-based on-line modulation of tube current: evaluation of six anatomical regions. *Eur Radiol* 2000; **10**: 391-394
- 25 **Itoh S**, Koyama S, Ikeda M, Ozaki M, Sawaki A, Iwano S, Ishigaki T. Further reduction of radiation dose in helical CT for lung cancer screening using small tube current and a newly designed filter. *J Thorac Imaging* 2001; **16**: 81-88
- 26 **Chen TW**, Yang ZG, Li Y, Li ZL, Yao J, Sun JY. Quantitative assessment of first-pass perfusion of oesophageal squamous cell carcinoma using 64-section MDCT: initial observation. *Clin Radiol* 2009; **64**: 38-45
- 27 **Chen TW**, Yang ZG, Wang QL, Li Y, Qian LL, Chen HJ. Whole tumour quantitative measurement of first-pass perfusion of oesophageal squamous cell carcinoma using 64-row multidetector computed tomography: correlation with microvessel density. *Eur J Radiol* 2011; **79**: 218-223
- 28 **Sulman EP**, Schwartz DL, Le TT, Ang KK, Morrison WH, Rosenthal DI, Ahamad A, Kies M, Glisson B, Weber R, Garden AS. IMRT reirradiation of head and neck cancer-disease control and morbidity outcomes. *Int J Radiat Oncol Biol Phys* 2009; **73**: 399-409
- 29 **Massoptier L**, Casciaro S. A new fully automatic and robust algorithm for fast segmentation of liver tissue and tumors from CT scans. *Eur Radiol* 2008; **18**: 1658-1665
- 30 **Conversano F**, Franchini R, Demitri C, Massoptier L, Montagna F, Maffezzoli A, Malvasi A, Casciaro S. Hepatic vessel segmentation for 3D planning of liver surgery experimental evaluation of a new fully automatic algorithm. *Acad Radiol* 2011; **18**: 461-470
- 31 **Feulner J**, Zhou SK, Hammon M, Seifert S, Huber M, Comaniciu D, Hornegger J, Cavallaro A. A probabilistic model for automatic segmentation of the esophagus in 3-D CT scans. *IEEE Trans Med Imaging* 2011; **30**: 1252-1264

S- Editor Cheng JX **L- Editor** O'Neill M **E- Editor** Zheng XM



ACKNOWLEDGMENTS

Acknowledgments to reviewers of *World Journal of Radiology*

Many reviewers have contributed their expertise and time to the peer review, a critical process to ensure the quality of *World Journal of Radiology*. The editors and authors of the articles submitted to the journal are grateful to the following reviewers for evaluating the articles (including those published in this issue and those rejected for this issue) during the last editing time period.

Eduardo J Aguilar, MD, PhD, Coordinador de Salud Mental, Psiquiatría, Hospital de Sagunto, Avda. Ramón y Cajal s/n, 46520 Sagunto, Spain

Filippo Cademartiri, MD, PhD, Dipartimento of Radiology - c/o Piastra Tecnica - Piano 0, Azienda Ospedaliero-Universitaria di Parma, Via Gramsci, 14 - 43100 Parma, Italy

Sergio Casciaro, PhD, Institute of Clinical Physiology - National Research Council, Campus Universitario Ecotekne, Via Monteroni, 73100 Lecce, Italy

James Chow, PhD, Radiation Physicist, Radiation Medicine

Program, Princess Margaret Hospital, 610 University Avenue, Toronto, ON M5G 2M9, Canada

Ragab Hani Donkol, Professor, Radiology Department, Aseer Central Hospital, 34 Abha, Saudi Arabia

Francesco Lassandro, MD, Department of Radiology, Monaldi Hospital, Via Leonardo Bianchi, 80129 Napoli, Italy

AAK Abdel Razek, MD, Professor, Diagnostic Radiology Department, 62 El Nokri St, Meet Hadr, Mansoura Faculty of Medicine, Mansoura 35111, Egypt

Jacob Sosna, MD, Section Chief, CT, Director of Research and Imaging Laboratories Department of Radiology, Hadassah Hebrew University Medical Center, Jerusalem 91120, Israel

Vlastimil Valek, Professor, MD, CSc, MBA, Department of Radiology, University Hospital Brno and Med. Faculty Masaryk University Brno, Brno 62800, Czech Republic

Hiroshi Yoshida, Department of Surgery, Nippon Medical School Tama Nagayama Hospital, Tokyo 205-8512, Japan



MEETINGS

Events Calendar 2012

January 3-7, 2012

Imaging at Bachelor Gulch
Beaver Creek, CO 81620,
United States

January 12-14, 2012

IROS 2012: Interventionell
Radiologischen Olbert Symposium
Salzburg, Austria

January 26-29, 2012

American Society of Neuroimaging
2012 35th Annual Meeting
Miami, FL 33169, United States

February 9-11, 2012

JIM joint interventional meeting
2012
Rome, Italy

February 13-16, 2012

Emergency Radiology
Palm Beach, FL 33480, United States

February 16-19, 2012

ASSR 2012 Annual Symposium
Miami Beach, FL 33169,
United States

February 19-23, 2012

Internal Derangements of Joints:
Advanced and Intensive MR
Imaging/With a Special Symposium
on Ankle and Foot
Coronado, CA 92118, United States

February 21-24, 2012

MRI in Practice
Oslo, Norway

March 1-5, 2012

ECR 2012
Vienna, Austria

March 7-10, 2012

ISCD's 18th Annual Meeting
Los Angeles, CA 90001,
United States

March 7-11, 2012

7th Annual Fundamentals of
Musculoskeletal Ultrasound
San Diego, CA 92111, United States

March 25-30, 2012

Diseases of the Brain, Head and
Neck Spine
Davos, Switzerland
April 13-15, 2012
ACR 35th National Conference on
Breast Cancer
Hollywood, FL 33019, United States

April 22-24, 2012

Euroson 2012
Madrid, Spain

April 24-27, 2012

MRI in Practice
Aalst, Belgium

April 25-28, 2012

ECIO 2012 - Third European
Conference on Interventional
Oncology
Florence, Italy

May 15-18, 2012

EURO PCR
Paris, France

May 19-23, 2012

ECTS 2012
Stockholm, Sweden

May 28-June 01, 2012

The International Congress of
Pediatric Radiology
Athens Greece

June 7-9, 2012

ASCI 2012 6th Congress of Asian
Society of Cardiovascular Imaging
Bangkok, Thailand

June 14-16, 2012

ICCIR 2012 - International
Conference on Complications in

Interventional Radiology
Poertschach, Austria

June 16-19, 2012

2nd IDKD Hong Kong 2012,
Diseases of the Abdomen and Pelvis
Hong Kong, China

June 17-20, 2012

14th Annual International
Symposium on Multidetector-Row
CT
San Francisco, CA 94103,
United States

June 27-30, 2012

CARS 2012
Pisa, Italy

July 1-3, 2012

16th Symposium Mammographicum
Harrogate, United Kingdom

July 19-22, 2012

Society of Cardiovascular Computed
Tomography 6th Annual Scientific
Meeting
Baltimore, Maryland

August 30-2, 2012

14th Asian Oceanian Congress of
Radiology
Sydney, Australia

September 6-8, 2012

Update in Abdominal and
Urogenital Imaging
Bruges, Belgium

September 12-15, 2012

ISS 2012
Rome, Italy

September 13-15, 2012

4th ESMINT Congress
Nice, France

September 13-16, 2012

18th Annual Symposium ESUR
Edinburgh, United Kingdom

September 15-19, 2012

CIRSE 2012
Lisbon, Portugal

September 20-23, 2012

2012 SDMS Annual Conference
Seattle, WA 98113, United States

September 24-27, 2012

MRI in Practice
Ballerup, Denmark

October 4-6, 2012

ESMRMB congress 2012 29th Annual
Scientific Meeting
Lisbon, Portugal

October 12-13, 2012

EUSOBI Annual Scientific Meeting
2012
Barcelona, Spain

October 26-28, 2012

22th Annual Meeting of the Society
of Radiologists in Ultrasound
Baltimore, MD 21213, United States

November 10-14, 2012

13th congress of WFITN
Buenos Aires, Argentina

November 14-17, 2012

BSIR Annual Meeting 2012
Bournemouth, United Kingdom

November 27- December 03, 2012

IEEE Nuclear Science Symposium
and Medical Imaging Conference
Anaheim, CA 92805, United States

December 2-4, 2012

ICI 2012 - Innovations in
Cardiovascular Interventions
Meeting
Tel Aviv, Israel

December 4-8, 2012

34rd San Antonio Breast Cancer
Symposium,
San Antonio, TX 78258 ,
United States



INSTRUCTIONS TO AUTHORS

GENERAL INFORMATION

World Journal of Radiology (*World J Radiol*, *WJR*, online ISSN 1949-8470, DOI: 10.4329), is a monthly, open-access (OA), peer-reviewed journal supported by an editorial board of 319 experts in Radiology from 40 countries.

The biggest advantage of the OA model is that it provides free, full-text articles in PDF and other formats for experts and the public without registration, which eliminates the obstacle that traditional journals possess and usually delays the speed of the propagation and communication of scientific research results. The open access model has been proven to be a true approach that may achieve the ultimate goal of the journals, i.e. the maximization of the value to the readers, authors and society.

Maximization of personal benefits

The role of academic journals is to exhibit the scientific levels of a country, a university, a center, a department, and even a scientist, and build an important bridge for communication between scientists and the public. As we all know, the significance of the publication of scientific articles lies not only in disseminating and communicating innovative scientific achievements and academic views, as well as promoting the application of scientific achievements, but also in formally recognizing the "priority" and "copyright" of innovative achievements published, as well as evaluating research performance and academic levels. So, to realize these desired attributes of *WJR* and create a well-recognized journal, the following four types of personal benefits should be maximized. The maximization of personal benefits refers to the pursuit of the maximum personal benefits in a well-considered optimal manner without violation of the laws, ethical rules and the benefits of others. (1) Maximization of the benefits of editorial board members: The primary task of editorial board members is to give a peer review of an unpublished scientific article via online office system to evaluate its innovativeness, scientific and practical values and determine whether it should be published or not. During peer review, editorial board members can also obtain cutting-edge information in that field at first hand. As leaders in their field, they have priority to be invited to write articles and publish commentary articles. We will put peer reviewers' names and affiliations along with the article they reviewed in the journal to acknowledge their contribution; (2) Maximization of the benefits of authors: Since *WJR* is an open-access journal, readers around the world can immediately download and read, free of charge, high-quality, peer-reviewed articles from *WJR* official website, thereby realizing the goals and significance of the communication between authors and peers as well as public reading; (3) Maximization of the benefits of readers: Readers can read or use, free of charge, high-quality peer-reviewed articles without any limits, and cite the arguments, viewpoints, concepts, theories, methods, results, conclusion or facts and data of pertinent literature so as to validate the innovativeness, scientific and practical values of their own research achievements, thus ensuring that their articles have novel arguments or viewpoints, solid evidence and correct conclusion; and (4) Maximization of the benefits of employees: It is an iron law that a first-class journal is unable to exist without first-class editors, and only first-class editors can create a first-class academic journal. We insist on strengthening our team cultivation and construction so that every employee, in an open, fair and transparent environment, could contribute their wisdom to edit and publish high-quality ar-

ticles, thereby realizing the maximization of the personal benefits of editorial board members, authors and readers, and yielding the greatest social and economic benefits.

Aims and scope

The major task of *WJR* is to rapidly report the most recent improvement in the research of medical imaging and radiation therapy by the radiologists. *WJR* accepts papers on the following aspects related to radiology: Abdominal radiology, women health radiology, cardiovascular radiology, chest radiology, genitourinary radiology, neuroradiology, head and neck radiology, interventional radiology, musculoskeletal radiology, molecular imaging, pediatric radiology, experimental radiology, radiological technology, nuclear medicine, PACS and radiology informatics, and ultrasound. We also encourage papers that cover all other areas of radiology as well as basic research.

Columns

The columns in the issues of *WJR* will include: (1) Editorial: To introduce and comment on major advances and developments in the field; (2) Frontier: To review representative achievements, comment on the state of current research, and propose directions for future research; (3) Topic Highlight: This column consists of three formats, including (A) 10 invited review articles on a hot topic, (B) a commentary on common issues of this hot topic, and (C) a commentary on the 10 individual articles; (4) Observation: To update the development of old and new questions, highlight unsolved problems, and provide strategies on how to solve the questions; (5) Guidelines for Basic Research: To provide guidelines for basic research; (6) Guidelines for Clinical Practice: To provide guidelines for clinical diagnosis and treatment; (7) Review: To review systemically progress and unresolved problems in the field, comment on the state of current research, and make suggestions for future work; (8) Original Articles: To report innovative and original findings in radiology; (9) Brief Articles: To briefly report the novel and innovative findings in radiology; (10) Case Report: To report a rare or typical case; (11) Letters to the Editor: To discuss and make reply to the contributions published in *WJR*, or to introduce and comment on a controversial issue of general interest; (12) Book Reviews: To introduce and comment on quality monographs of radiology; and (13) Guidelines: To introduce consensus and guidelines reached by international and national academic authorities worldwide on the research in radiology.

Name of journal

World Journal of Radiology

ISSN

ISSN 1949-8470 (online)

Editor-in-Chief

Filippo Cademartiri, MD, PhD, FESC, FSCCT, Professor, Cardio-Vascular Imaging Unit-Giovanni XXIII Hospital, Via Giovanni XXIII, 7-31050-Monastier di Treviso (TV), Italy

Editorial Office

World Journal of Radiology

Editorial Department: Room 903, Building D,
Ocean International Center, No. 62 Dongsihuan Zhonglu,
Chaoyang District, Beijing 100025, China

Instructions to authors

E-mail: [wjw@wjnet.com](mailto:wjr@wjnet.com)
<http://www.wjnet.com>
Telephone: +86-10-59080039
Fax: +86-10-85381893

Indexed and Abstracted in

PubMed Central, PubMed, Digital Object Identifier, and Directory of Open Access Journals.

Published by

Baishideng Publishing Group Co., Limited.

SPECIAL STATEMENT

All articles published in this journal represent the viewpoints of the authors except where indicated otherwise.

Biostatistical editing

Statistical review is performed after peer review. We invite an expert in Biomedical Statistics from to evaluate the statistical method used in the paper, including *t*-test (group or paired comparisons), chi-squared test, Redit, probit, logit, regression (linear, curvilinear, or stepwise), correlation, analysis of variance, analysis of covariance, *etc.* The reviewing points include: (1) Statistical methods should be described when they are used to verify the results; (2) Whether the statistical techniques are suitable or correct; (3) Only homogeneous data can be averaged. Standard deviations are preferred to standard errors. Give the number of observations and subjects (*n*). Losses in observations, such as drop-outs from the study should be reported; (4) Values such as ED50, LD50, IC50 should have their 95% confidence limits calculated and compared by weighted probit analysis (Bliss and Finney); and (5) The word 'significantly' should be replaced by its synonyms (if it indicates extent) or the *P* value (if it indicates statistical significance).

Conflict-of-interest statement

In the interests of transparency and to help reviewers assess any potential bias, *WJR* requires authors of all papers to declare any competing commercial, personal, political, intellectual, or religious interests in relation to the submitted work. Referees are also asked to indicate any potential conflict they might have reviewing a particular paper. Before submitting, authors are suggested to read "Uniform Requirements for Manuscripts Submitted to Biomedical Journals: Ethical Considerations in the Conduct and Reporting of Research: Conflicts of Interest" from International Committee of Medical Journal Editors (ICMJE), which is available at: http://www.icmje.org/ethical_4conflicts.html.

Sample wording: [Name of individual] has received fees for serving as a speaker, a consultant and an advisory board member for [names of organizations], and has received research funding from [names of organization]. [Name of individual] is an employee of [name of organization]. [Name of individual] owns stocks and shares in [name of organization]. [Name of individual] owns patent [patent identification and brief description].

Statement of informed consent

Manuscripts should contain a statement to the effect that all human studies have been reviewed by the appropriate ethics committee or it should be stated clearly in the text that all persons gave their informed consent prior to their inclusion in the study. Details that might disclose the identity of the subjects under study should be omitted. Authors should also draw attention to the Code of Ethics of the World Medical Association (Declaration of Helsinki, 1964, as revised in 2004).

Statement of human and animal rights

When reporting the results from experiments, authors should follow the highest standards and the trial should conform to Good Clinical Practice (for example, US Food and Drug Administration Good Clinical Practice in FDA-Regulated Clinical Trials; UK Medicines Research Council Guidelines for Good Clinical Practice in Clinical Trials) and/or the World Medical Association Declaration of Helsinki. Generally, we suggest authors follow the lead investigator's national standard. If doubt exists whether the research was conducted

in accordance with the above standards, the authors must explain the rationale for their approach and demonstrate that the institutional review body explicitly approved the doubtful aspects of the study.

Before submitting, authors should make their study approved by the relevant research ethics committee or institutional review board. If human participants were involved, manuscripts must be accompanied by a statement that the experiments were undertaken with the understanding and appropriate informed consent of each. Any personal item or information will not be published without explicit consents from the involved patients. If experimental animals were used, the materials and methods (experimental procedures) section must clearly indicate that appropriate measures were taken to minimize pain or discomfort, and details of animal care should be provided.

SUBMISSION OF MANUSCRIPTS

Manuscripts should be typed in 1.5 line spacing and 12 pt. Book Antiqua with ample margins. Number all pages consecutively, and start each of the following sections on a new page: Title Page, Abstract, Introduction, Materials and Methods, Results, Discussion, Acknowledgements, References, Tables, Figures, and Figure Legends. Neither the editors nor the publisher are responsible for the opinions expressed by contributors. Manuscripts formally accepted for publication become the permanent property of Baishideng Publishing Group Co., Limited, and may not be reproduced by any means, in whole or in part, without the written permission of both the authors and the publisher. We reserve the right to copy-edit and put onto our website accepted manuscripts. Authors should follow the relevant guidelines for the care and use of laboratory animals of their institution or national animal welfare committee. For the sake of transparency in regard to the performance and reporting of clinical trials, we endorse the policy of the ICMJE to refuse to publish papers on clinical trial results if the trial was not recorded in a publicly-accessible registry at its outset. The only register now available, to our knowledge, is <http://www.clinicaltrials.gov> sponsored by the United States National Library of Medicine and we encourage all potential contributors to register with it. However, in the case that other registers become available you will be duly notified. A letter of recommendation from each author's organization should be provided with the contributed article to ensure the privacy and secrecy of research is protected.

Authors should retain one copy of the text, tables, photographs and illustrations because rejected manuscripts will not be returned to the author(s) and the editors will not be responsible for loss or damage to photographs and illustrations sustained during mailing.

Online submissions

Manuscripts should be submitted through the Online Submission System at: <http://www.wjnet.com/1949-8470office>. Authors are highly recommended to consult the ONLINE INSTRUCTIONS TO AUTHORS (http://www.wjnet.com/1949-8470/g_info_20100316162358.htm) before attempting to submit online. For assistance, authors encountering problems with the Online Submission System may send an email describing the problem to [wjw@wjnet.com](mailto:wjr@wjnet.com), or by telephone: +86-10-85381892. If you submit your manuscript online, do not make a postal contribution. Repeated online submission for the same manuscript is strictly prohibited.

MANUSCRIPT PREPARATION

All contributions should be written in English. All articles must be submitted using word-processing software. All submissions must be typed in 1.5 line spacing and 12 pt. Book Antiqua with ample margins. Style should conform to our house format. Required information for each of the manuscript sections is as follows:

Title page

Title: Title should be less than 12 words.

Running title: A short running title of less than 6 words should be provided.

Authorship: Authorship credit should be in accordance with the standard proposed by International Committee of Medical Journal Editors, based on (1) substantial contributions to conception and design, acquisition of data, or analysis and interpretation of data; (2) drafting the article or revising it critically for important intellectual content; and (3) final approval of the version to be published. Authors should meet conditions 1, 2, and 3.

Institution: Author names should be given first, then the complete name of institution, city, province and postcode. For example, Xu-Chen Zhang, Li-Xin Mei, Department of Pathology, Chengde Medical College, Chengde 067000, Hebei Province, China. One author may be represented from two institutions, for example, George Sgourakis, Department of General, Visceral, and Transplantation Surgery, Essen 45122, Germany; George Sgourakis, 2nd Surgical Department, Korgialenio-Benakio Red Cross Hospital, Athens 15451, Greece

Author contributions: The format of this section should be: Author contributions: Wang CL and Liang L contributed equally to this work; Wang CL, Liang L, Fu JF, Zou CC, Hong F and Wu XM designed the research; Wang CL, Zou CC, Hong F and Wu XM performed the research; Xue JZ and Lu JR contributed new reagents/analytic tools; Wang CL, Liang L and Fu JF analyzed the data; and Wang CL, Liang L and Fu JF wrote the paper.

Supportive foundations: The complete name and number of supportive foundations should be provided, e.g., Supported by National Natural Science Foundation of China, No. 30224801

Correspondence to: Only one corresponding address should be provided. Author names should be given first, then author title, affiliation, the complete name of institution, city, postcode, province, country, and email. All the letters in the email should be in lower case. A space interval should be inserted between country name and email address. For example, Montgomery Bissell, MD, Professor of Medicine, Chief, Liver Center, Gastroenterology Division, University of California, Box 0538, San Francisco, CA 94143, United States. montgomery.bissell@ucsf.edu

Telephone and fax: Telephone and fax should consist of +, country number, district number and telephone or fax number, e.g., Telephone: +86-10-85381892 Fax: +86-10-85381893

Peer reviewers: All articles received are subject to peer review. Normally, three experts are invited for each article. Decision for acceptance is made only when at least two experts recommend an article for publication. Reviewers for accepted manuscripts are acknowledged in each manuscript, and reviewers of articles which were not accepted will be acknowledged at the end of each issue. To ensure the quality of the articles published in *WJR*, reviewers of accepted manuscripts will be announced by publishing the name, title/position and institution of the reviewer in the footnote accompanying the printed article. For example, reviewers: Professor Jing-Yuan Fang, Shanghai Institute of Digestive Disease, Shanghai, Affiliated Renji Hospital, Medical Faculty, Shanghai Jiaotong University, Shanghai, China; Professor Xin-Wei Han, Department of Radiology, The First Affiliated Hospital, Zhengzhou University, Zhengzhou, Henan Province, China; and Professor Anren Kuang, Department of Nuclear Medicine, Huaxi Hospital, Sichuan University, Chengdu, Sichuan Province, China.

Abstract

There are unstructured abstracts (no more than 256 words) and structured abstracts (no more than 480). The specific requirements for structured abstracts are as follows:

An informative, structured abstracts of no more than 480 words should accompany each manuscript. Abstracts for original contributions should be structured into the following sections. AIM (no more than 20 words): Only the purpose should be included. Please write the aim as the form of "To investigate/study/...;

MATERIALS AND METHODS (no more than 140 words); RESULTS (no more than 294 words): You should present *P* values where appropriate and must provide relevant data to illustrate how they were obtained, e.g. 6.92 ± 3.86 vs 3.61 ± 1.67 , $P < 0.001$; CONCLUSION (no more than 26 words).

Key words

Please list 5-10 key words, selected mainly from *Index Medicus*, which reflect the content of the study.

Text

For articles of these sections, original articles and brief articles, the main text should be structured into the following sections: INTRODUCTION, MATERIALS AND METHODS, RESULTS and DISCUSSION, and should include appropriate Figures and Tables. Data should be presented in the main text or in Figures and Tables, but not in both. The main text format of these sections, editorial, topic highlight, case report, letters to the editors, can be found at: http://www.wjgnet.com/1949-8470/g_info_20100313183720.htm.

Illustrations

Figures should be numbered as 1, 2, 3, *etc.*, and mentioned clearly in the main text. Provide a brief title for each figure on a separate page. Detailed legends should not be provided under the figures. This part should be added into the text where the figures are applicable. Figures should be either Photoshop or Illustrator files (in tiff, eps, jpeg formats) at high-resolution. Examples can be found at: <http://www.wjgnet.com/1007-9327/13/4520.pdf>; <http://www.wjgnet.com/1007-9327/13/4554.pdf>; <http://www.wjgnet.com/1007-9327/13/4891.pdf>; <http://www.wjgnet.com/1007-9327/13/4986.pdf>; <http://www.wjgnet.com/1007-9327/13/4498.pdf>. Keeping all elements compiled is necessary in line-art image. Scale bars should be used rather than magnification factors, with the length of the bar defined in the legend rather than on the bar itself. File names should identify the figure and panel. Avoid layering type directly over shaded or textured areas. Please use uniform legends for the same subjects. For example: Figure 1 Pathological changes in atrophic gastritis after treatment. A: ...; B: ...; C: ...; D: ...; E: ...; F: ...; G: ... *etc.* It is our principle to publish high resolution-figures for the printed and E-versions.

Tables

Three-line tables should be numbered 1, 2, 3, *etc.*, and mentioned clearly in the main text. Provide a brief title for each table. Detailed legends should not be included under tables, but rather added into the text where applicable. The information should complement, but not duplicate the text. Use one horizontal line under the title, a second under column heads, and a third below the Table, above any footnotes. Vertical and italic lines should be omitted.

Notes in tables and illustrations

Data that are not statistically significant should not be noted. ^a*P* < 0.05, ^b*P* < 0.01 should be noted (*P* > 0.05 should not be noted). If there are other series of *P* values, ^c*P* < 0.05 and ^d*P* < 0.01 are used. A third series of *P* values can be expressed as ^e*P* < 0.05 and ^f*P* < 0.01. Other notes in tables or under illustrations should be expressed as ¹F, ²F, ³F; or sometimes as other symbols with a superscript (Arabic numerals) in the upper left corner. In a multi-curve illustration, each curve should be labeled with ●, ○, ■, □, ▲, △, *etc.*, in a certain sequence.

Acknowledgments

Brief acknowledgments of persons who have made genuine contributions to the manuscript and who endorse the data and conclusions should be included. Authors are responsible for obtaining written permission to use any copyrighted text and/or illustrations.

REFERENCES

Coding system

The author should number the references in Arabic numerals ac-

Instructions to authors

cording to the citation order in the text. Put reference numbers in square brackets in superscript at the end of citation content or after the cited author's name. For citation content which is part of the narration, the coding number and square brackets should be typeset normally. For example, "Crohn's disease (CD) is associated with increased intestinal permeability^[1,2]". If references are cited directly in the text, they should be put together within the text, for example, "From references^[19,22-24], we know that..."

When the authors write the references, please ensure that the order in text is the same as in the references section, and also ensure the spelling accuracy of the first author's name. Do not list the same citation twice.

PMID and DOI

Please provide PubMed citation numbers to the reference list, e.g. PMID and DOI, which can be found at <http://www.ncbi.nlm.nih.gov/sites/entrez?db=pubmed> and <http://www.crossref.org/SimpleTextQuery/>, respectively. The numbers will be used in E-version of this journal.

Style for journal references

Authors: the name of the first author should be typed in bold-faced letters. The family name of all authors should be typed with the initial letter capitalized, followed by their abbreviated first and middle initials. (For example, Lian-Sheng Ma is abbreviated as Ma LS, Bo-Rong Pan as Pan BR). The title of the cited article and italicized journal title (journal title should be in its abbreviated form as shown in PubMed), publication date, volume number (in black), start page, and end page [PMID: 11819634 DOI: 10.3748/wjg.13.5396].

Style for book references

Authors: the name of the first author should be typed in bold-faced letters. The surname of all authors should be typed with the initial letter capitalized, followed by their abbreviated middle and first initials. (For example, Lian-Sheng Ma is abbreviated as Ma LS, Bo-Rong Pan as Pan BR) Book title. Publication number. Publication place: Publication press, Year: start page and end page.

Format

Journals

English journal article (list all authors and include the PMID where applicable)

- 1 **Jung EM**, Clevert DA, Schreyer AG, Schmitt S, Rennert J, Kubale R, Feuerbach S, Jung F. Evaluation of quantitative contrast harmonic imaging to assess malignancy of liver tumors: A prospective controlled two-center study. *World J Gastroenterol* 2007; **13**: 6356-6364 [PMID: 18081224 DOI: 10.3748/wjg.13.6356]

Chinese journal article (list all authors and include the PMID where applicable)

- 2 **Lin GZ**, Wang XZ, Wang P, Lin J, Yang FD. Immunologic effect of Jianpi Yishen decoction in treatment of Pixu-diarhoea. *Shijie Huaren Xiaohua Zazhi* 1999; **7**: 285-287

In press

- 3 **Tian D**, Araki H, Stahl E, Bergelson J, Kreitman M. Signature of balancing selection in Arabidopsis. *Proc Natl Acad Sci USA* 2006; In press

Organization as author

- 4 **Diabetes Prevention Program Research Group**. Hypertension, insulin, and proinsulin in participants with impaired glucose tolerance. *Hypertension* 2002; **40**: 679-686 [PMID: 12411462 PMID:2516377 DOI:10.1161/01.HYP0000035706.28494.09]

Both personal authors and an organization as author

- 5 **Vallancien G**, Emberton M, Harving N, van Moorselaar RJ; Alf-One Study Group. Sexual dysfunction in 1, 274 European men suffering from lower urinary tract symptoms. *J Urol* 2003; **169**: 2257-2261 [PMID: 12771764 DOI:10.1097/01.ju.0000067940.76090.73]

No author given

- 6 21st century heart solution may have a sting in the tail. *BMJ*

2002; **325**: 184 [PMID: 12142303 DOI:10.1136/bmj.325.7357.184]

Volume with supplement

- 7 **Geraud G**, Spierings EL, Keywood C. Tolerability and safety of frovatriptan with short- and long-term use for treatment of migraine and in comparison with sumatriptan. *Headache* 2002; **42** Suppl 2: S93-99 [PMID: 12028325 DOI:10.1046/j.1526-4610.42.s2.7.x]

Issue with no volume

- 8 **Banit DM**, Kaufer H, Hartford JM. Intraoperative frozen section analysis in revision total joint arthroplasty. *Clin Orthop Relat Res* 2002; **(401)**: 230-238 [PMID: 12151900 DOI:10.1097/00003086-200208000-00026]

No volume or issue

- 9 Outreach: Bringing HIV-positive individuals into care. *HRSA Careaction* 2002; 1-6 [PMID: 12154804]

Books

Personal author(s)

- 10 **Sherlock S**, Dooley J. Diseases of the liver and biliary system. 9th ed. Oxford: Blackwell Sci Pub, 1993: 258-296

Chapter in a book (list all authors)

- 11 **Lam SK**. Academic investigator's perspectives of medical treatment for peptic ulcer. In: Swabb EA, Azabo S. Ulcer disease: investigation and basis for therapy. New York: Marcel Dekker, 1991: 431-450

Author(s) and editor(s)

- 12 **Breedlove GK**, Schorfheide AM. Adolescent pregnancy. 2nd ed. Wiczorek RR, editor. White Plains (NY): March of Dimes Education Services, 2001: 20-34

Conference proceedings

- 13 **Harden P**, Joffe JK, Jones WG, editors. Germ cell tumours V. Proceedings of the 5th Germ cell tumours Conference; 2001 Sep 13-15; Leeds, UK. New York: Springer, 2002: 30-56

Conference paper

- 14 **Christensen S**, Oppacher F. An analysis of Koza's computational effort statistic for genetic programming. In: Foster JA, Lutton E, Miller J, Ryan C, Tettamanzi AG, editors. Genetic programming. EuroGP 2002: Proceedings of the 5th European Conference on Genetic Programming; 2002 Apr 3-5; Kinsdale, Ireland. Berlin: Springer, 2002: 182-191

Electronic journal (list all authors)

- 15 Morse SS. Factors in the emergence of infectious diseases. *Emerg Infect Dis* serial online, 1995-01-03, cited 1996-06-05; 1(1): 24 screens. Available from: URL: <http://www.cdc.gov/ncidod/eid/index.htm>

Patent (list all authors)

- 16 **Pagedas AC**, inventor; Ancel Surgical R&D Inc., assignee. Flexible endoscopic grasping and cutting device and positioning tool assembly. United States patent US 20020103498. 2002 Aug 1

Statistical data

Write as mean \pm SD or mean \pm SE.

Statistical expression

Express *t* test as *t* (in italics), *F* test as *F* (in italics), chi square test as χ^2 (in Greek), related coefficient as *r* (in italics), degree of freedom as *v* (in Greek), sample number as *n* (in italics), and probability as *P* (in italics).

Units

Use SI units. For example: body mass, *m* (B) = 78 kg; blood pressure, *p* (B) = 16.2/12.3 kPa; incubation time, *t* (incubation) = 96 h; blood glucose concentration, *c* (glucose) 6.4 ± 2.1 mmol/L; blood CEA mass concentration, *p* (CEA) = 8.6 ± 24.5 μ g/L; CO₂ volume fraction, 50 mL/L CO₂, not 5% CO₂; likewise for 40 g/L formaldehyde, not 10% formalin; and mass fraction, 8 ng/g, *etc.* Arabic numerals such as 23, 243, 641 should be read 23 243 641.

The format for how to accurately write common units and quantum can be found at: http://www.wjgnet.com/1949-8470/g_info_20100313185816.htm.

Abbreviations

Standard abbreviations should be defined in the abstract and on first mention in the text. In general, terms should not be abbreviated unless they are used repeatedly and the abbreviation is helpful to the reader. Permissible abbreviations are listed in Units, Symbols and Abbreviations: A Guide for Biological and Medical Editors and Authors (Ed. Baron DN, 1988) published by The Royal Society of Medicine, London. Certain commonly used abbreviations, such as DNA, RNA, HIV, LD50, PCR, HBV, ECG, WBC, RBC, CT, ESR, CSF, IgG, ELISA, PBS, ATP, EDTA, mAb, can be used directly without further explanation.

Italics

Quantities: *t* time or temperature, *c* concentration, *A* area, *l* length, *m* mass, *V* volume.

Genotypes: *gyrA*, *arg 1*, *c myc*, *c fos*, etc.

Restriction enzymes: *EcoRI*, *HindI*, *BamHI*, *Kbo I*, *Kpn I*, etc.

Biology: *H. pylori*, *E. coli*, etc.

Examples for paper writing

Editorial: http://www.wjgnet.com/1949-8470/g_info_20100313182341.htm

Frontier: http://www.wjgnet.com/1949-8470/g_info_20100313182448.htm

Topic highlight: http://www.wjgnet.com/1949-8470/g_info_20100313182639.htm

Observation: http://www.wjgnet.com/1949-8470/g_info_20100313182834.htm

Guidelines for basic research: http://www.wjgnet.com/1949-8470/g_info_20100313183057.htm

Guidelines for clinical practice: http://www.wjgnet.com/1949-8470/g_info_20100313183238.htm

Review: http://www.wjgnet.com/1949-8470/g_info_20100313183433.htm

Original articles: http://www.wjgnet.com/1949-8470/g_info_20100313183720.htm

Brief articles: http://www.wjgnet.com/1949-8470/g_info_20100313184005.htm

Case report: http://www.wjgnet.com/1949-8470/g_info_20100313184149.htm

Letters to the editor: http://www.wjgnet.com/1949-8470/g_info_20100313184410.htm

Book reviews: http://www.wjgnet.com/1949-8470/g_info_20100313184803.htm

Guidelines: http://www.wjgnet.com/1949-8470/g_info_20100313185047.htm

SUBMISSION OF THE REVISED MANUSCRIPTS AFTER ACCEPTED

Please revise your article according to the revision policies of *WJR*. The revised version including manuscript and high-resolution image figures (if any) should be re-submitted online (<http://www.wjgnet.com/1949-8470office/>). The author should send the copyright transfer letter, responses to the reviewers, English language Grade B certificate (for non-native speakers of English) and final manuscript checklist to [wjgnet.com](mailto:wjr@wjgnet.com).

Language evaluation

The language of a manuscript will be graded before it is sent for revision. (1) Grade A: priority publishing; (2) Grade B: minor language polishing; (3) Grade C: a great deal of language polishing needed; and (4) Grade D: rejected. Revised articles should reach Grade A or B.

Copyright assignment form

Please download a Copyright assignment form from http://www.wjgnet.com/1949-8470/g_info_20100313185522.htm.

Responses to reviewers

Please revise your article according to the comments/suggestions provided by the reviewers. The format for responses to the reviewers' comments can be found at: http://www.wjgnet.com/1949-8470/g_info_20100313185358.htm.

Proof of financial support

For paper supported by a foundation, authors should provide a copy of the document and serial number of the foundation.

Links to documents related to the manuscript

WJR will be initiating a platform to promote dynamic interactions between the editors, peer reviewers, readers and authors. After a manuscript is published online, links to the PDF version of the submitted manuscript, the peer-reviewers' report and the revised manuscript will be put on-line. Readers can make comments on the peer reviewer's report, authors' responses to peer reviewers, and the revised manuscript. We hope that authors will benefit from this feedback and be able to revise the manuscript accordingly in a timely manner.

Science news releases

Authors of accepted manuscripts are suggested to write a science news item to promote their articles. The news will be released rapidly at EurekAlert/AAAS (<http://www.eurekalert.org>). The title for news items should be less than 90 characters; the summary should be less than 75 words; and main body less than 500 words. Science news items should be lawful, ethical, and strictly based on your original content with an attractive title and interesting pictures.

Publication fee

WJR is an international, peer-reviewed, Open-Access, online journal. Articles published by this journal are distributed under the terms of the Creative Commons Attribution Non-commercial License, which permits use, distribution, and reproduction in any medium, provided the original work is properly cited, the use is non commercial and is otherwise in compliance with the license. Authors of accepted articles must pay a publication fee. The related standards are as follows. Publication fee: 1300 USD per article; Reprints fee: 350 USD per 100 reprints, including postage cost. Editorial, topic highlights, book reviews and letters to the editor are published free of charge.